# A Novel Deployable Radiator Architecture for High-Power Spacecraft Missions by Connecting Tapered and Layered Panels with Thin Kinked Tubes

by

**Kyle B. Marquis**

B.A.Sc., University of British Columbia, 2019

A thesis submitted to the

Faculty of the Graduate School of the

University of Colorado in partial fulfillment

of the requirements for the degree of

Master of Science

Ann and H.J. Smead Department of Aerospace Engineering Sciences

2021

Committee Members:

Francisco López Jiménez, Chair

James Nabity

David Marshall

Marquis, Kyle B. (M.S., Aerospace Engineering)

A Novel Deployable Radiator Architecture for High-Power Spacecraft Missions by Connecting

    Tapered and Layered Panels with Thin Kinked Tubes

Thesis directed by Prof. Francisco López Jiménez

A novel deployable radiator system has been designed to reject kilowatt-scale power at a fraction of the mass compared to existing technology. The architecture involves a mechanically pumped fluid loop (MPFL) system, inspired by Mars Rover missions, to scale up for the high heat-rejection capabilities that will be necessary as spacecraft become more powerful. The system consists of layered and tapered radiator panels that undergo a similar deployment to rigid solar panels: stowed in a zigzag configuration before flattening straight out. Thin tubes are proposed as structural connectors between panels, acting as deployable hinges as well as thermal-fluid transport tubes. Experiments have characterized the tubes' bending moment vs angle relationship, and a prototype successfully demonstrated the deployment process using only static pressure from an accumulator which would be sufficient to deploy the tubes in space. A release mechanism for initiating the deployment, using a scrolling sheet released through a burn wire, enables deployment after experiencing launching loads. The single-phase fluid loop system was designed based on existing similar technology, and simplified in order to reduce mass and complexity. The performance of traditional radiator panels is improved by combining advances in materials science with optimal thermal geometry. Instead of aluminum sandwich panels, pyrolytic graphite sheets are used in a tapered configuration to reject 61 W for each 126 g panel when at the layer base temperature of 300 K. Finite element analysis and numerical models are used to determine the effects of layer anisotropy of the design, as well as compute the thermal performance. A single radiator panel was prototyped with the same process and materials as proposed, and the design appears capable of good thermal contact without the need for fasteners. A dynamic analysis was conducted for the 28-panel system for the expected critical modes of vibration resulting in an insufficient natural frequency of 0.02

Hz. Through the addition of lightweight hinges and lengthened panels, the system is expected to perform with a fundamental frequency over 0.4 Hz, which is similar to existing deployed panel arrays. Finally, a thermal resistance network was created and solved numerically to determine the heat rejection from a 28-panel pumped-fluid-loop system for a 50 °C spacecraft. Areal density was found to be 1.9 kg/m$^2$, or 3.9 kg/m$^2$ if considering planform area, both considering the total system mass. Heat flux, or rejection per unit radiating area is 205 W/m$^2$, or 409 W/m$^2$ for the planform area. With a weight of 13.3 kg, the system is projected to reject 1400 W of heat, 106 W/kg, a threefold improvement in specific power over similar existing architectures. By incorporating features, developing, and scaling aspects of this design, the next generation of high-power space missions can be realized.

## Dedication

This work is dedicated to my friends who shared and discovered the love for space exploration with me. As well, to my family - for without their support, I would not be here today. To you, the reader, I encourage you to stay curious and always strive to do better in everything that you do.

# Acknowledgements

Many thanks goes out to my professor, thesis advisor, and mentor Dr. Francisco Lopez Jimenez. The number of hours he has spent to coach me, introduce me into his lab, and challenge my ideas is remarkable. I appreciate the willingness to work with me in not only the domain of deployable structures, but also in thermal analysis. The extent to which he consistently took time out of his week to review my work has exceeded expectations.

I would like to recognize the work of Kayla Ployhar, an undergraduate mechanical engineering student who helped develop and prototype the design. Through calculations, drawings, CAD modeling and more, her contributions made this project a success.

I would like to recognize the assistance of Yasara Dharmadasa who helped me analyze the stiffness of composite hinges.

To the aerospace department staff - machinists, fabrication coordinator, building manager, and purchaser - who enabled me to build and test my designs, thanks for helping me make these designs a reality.

Finally, I would also like to recognize the contributions from the Beverly Sears Graduate Student Grant Fund for providing financial support to purchase components for a prototype.

# Contents

**Chapter**

# Tables

**Table**

# Figures

**Figure**

# Chapter 1

# Introduction

Thermal control systems are used to regulate the temperatures within spacecraft, protecting sensitive components from exceeding operational limits. As larger and more complex spacecraft — satellites, probes, habitats, communications craft, and landers — are developed, the need for lightweight, robust, and high-performance thermal control systems (TCS) is emerging as humanity pushes to explore the solar system. Specifically, there have been recent calls by the US Air Force in SBIR programs asking for solutions to develop high power radiators (1000 W range) for smallsat missions [1], and similar NASA SBIR [2] requests for two-phase mechanically pumped fluid loop radiator designs.

This need for higher performance radiators was one of the initial drivers that motivated this work, along with noticing a significant lack of off-the-shelf thermal radiator solutions. This project set out to design and prototype an over 1000 W radiator solution that could be easily implemented in future space missions specifically as a scalable solution, with the goal to reject the most amount of heat per unit mass compared to existing technology.

In exploring the possibility of a novel radiator design and now having proposed a concept, this work addresses research questions such as: whether radiators composed of highly conductive pyrolytic graphite sheet can perform better than existing alternatives; whether a tapered and layered radiator panel can be made structurally sound; whether thin kinked tubes acting as hinges can reduce mass and can they deploy radiator panels when pressurized; what the deployment process looks like for these kinked tube hinges; and whether simplifications can be made to mechanically

pumped fluid loops to reduce mass while maintaining robustness. Below, this introduction summarizes an approach to achieve better performance and looks at existing technology for perspective. In the following sections, the design is proposed, compared against similar technology, and analyzed - answering these hypotheses along the way.

Partial results from this study were previously reported at the International Conference on Environmental Systems in 2021 [3, 4]. Approval was given to allow shared material between these works.

## 1.1    Thermal Design Philosophy

A difficulty in designing a low-weight deployable radiator system is that of designing a thermal hinge. Standard capillary-based heat pipes are typically solid tubes which cannot bend. Loop heat pipes get around this by locating the condenser apart from the wick evaporator and use a flexible hose carrying fluid, and therefore heat, through the joint as demonstrated by Lécossais [5]. This enables further distances for fluid to travel, but the technology is still limited by capillary action. Additionally, these hinges often achieve deployment by using an actuator to bend a stiff panel [5] in the same manner as an elbow extends an arm. This mechanical system increases the weight and complexity of the structure, which is undesirable in small satellites. Other solutions consider a flexible-wick heat pipe [6], but the proposals for this technology are in the hundreds-of-watts regime and are still limited by capillary action.

In this work, we follow a common approach in deployable space structures in which deployment is achieved through the elastic deformation of structural elements [7]. In particular, we propose a new thermal hinge mechanism using thin, flexible tubes which will serve three purposes: structural elements connecting the panels of a radiator, hinges in the panel deployment, and thermal hinges allowing unrestricted flow in the fluid loop.

In order to further reduce weight, the proposed solution does not rely on traditional radiator architectures based on aluminum sandwich panels filled with tubes carrying heat [8, 5, 9]. Sandwich panels are not an optimal design for a radiator due to the unnecessary structural mass and the

need for the heat to transmit through the core of the panels to the face-sheets. Additionally, these designs do not leverage new materials with conductivity per unit weight significantly higher than those of aluminum.

Regarding the material choice, pyrolytic graphite sheets (PGS) are commonly available and often used thermally in computer electronics. These sheets have an in-plane thermal conductivity five times higher than aluminum with around 70 % of the density, making them a clear choice to design a novel radiator panel [10, 11]. A comparison of PGS against a typical aluminum radiator is also highlighted in a 2017 paper from Maas [12] demonstrating the advantages. Maas' layered design has even been proposed with a tape-spring-hinge deployable radiator in a 2021 Thesis by van Lierop [13], but it is not a high-powered application. As Maas points out and as we have experienced, there are many challenges in utilizing a layered architecture as these sheets are very thin and brittle if not supported with adhesive backing.

Regarding geometry, the proposed design leverages the fact that tapered fins are the optimal shape for a convective fin in terms of heat per unit volume [14]. I apply the same principle to the design of the radiators: mass at the end of a fin is not conducting the same amount of heat as the initial sections, making it less efficient. This solution was explored by NASA researchers looking for an optimal aluminum fin structure for radiation in the 1960s [15].

This paper describes an approach to build, deploy, and control a pumped-fluid-loop system with novel tapered and layered radiator panels. However, the approach to structurally support these layered panels is a challenge and a primary trade-off when considering this novel design. Thermal performance is investigated, and by combining the mass budget data, comparisons are made to existing and proposed technologies. As a highly compact and modular design, a solution like this could become an off-the-shelf solution for mission designers that need to reject kilowatt-scale heat while keeping the stowed volume at a minimum.

### 1.1.1 Heat Transfer in Spacecraft

There are three main methods of transferring heat between media: conduction, convection, and radiation. Physical transport of material can also be used to carry heat from one location to another, storing energy in the temperature and possibly phase of the material. In space, conduction and convection cannot be used to reject heat so radiation, along with transport of material (jettison), are the only realistic ways to remove heat from the boundary that surrounds a spacecraft. However, mass is not typically rejected from craft for thermal purposes, with the exceptions of ablative heat shields (which collide into atmospheric particles and flake off to prevent intrusion of heat), and spacesuit applications (evaporative cooling). This leaves radiation as the primary method to reject heat from most spacecraft.

Controlling the radiative heat transfer is important to ensure that operational temperature limits are being met for spacecraft to survive. This can be accomplished by operating a well-designed passive system in the perfect environment, or by using a host of different technologies to function in a diverse set of thermal environments: ones which could include cycles of planetary albedo, self shading, or solar irradiance. This control of heat flow can be accomplished by the use of technologies such as heat pipes [16], thermal louvers [17], self-shading radiator panels [18], variable emissivity coatings [19], thermal switches [20], bypass or flow control valves [21, 22, 23], or fluid-loop pump speed variation [24]. The details of these various control methods are not a primary focus of this work, but will be considered as part of the fluid loop design.

With radiation as the goal, how do spacecraft get the heat from within their internal computers and instruments to the radiator panels? Passively, heat pipes and thermal straps are used for smaller power spacecraft [25], and for higher power spacecraft, loop heat pipes [5] and mechanically-pumped-fluid-loops [23] connect the radiators to the instruments using dedicated cold plates to transfer the fluid. Choosing between these higher powered options can involve many trade-offs, and the rationale for the proposed design is below.

### 1.1.2 Pumped Fluid Loop vs Heat Pipes

Heat pipes are a common choice for spacecraft because they are passive mechanisms to transport heat. There are many different types of heat pipes, such as constant conductance, variable conductance, diode, and loop heat pipes [16].

An issue with heat pipes is that some cannot be easily tested on Earth, such as 3-dimensional heat pipes since gravity can play a large adverse affect on the operation [16]. As well, performance decreases with length in traditional constant conductance heat pipes, seen from the graphs from Enertron Inc. Other factors limiting performance of heat pipes include their sonic limit, flooding, and boiling which can prevent nominal operation if a heat pipe is not properly designed for its environment [16]. Classic heat pipes do not typically transfer large amounts of heat very far, however, loop heat pipes (LHPs) are able to transport a large amount of heat across larger distances up to tens of meters [26]. These have gained traction and have been used and proposed for many spacecraft [26, 5]. LHPs enable larger heat rejection than typical heat pipe systems by separating the wicking from the evaporation sections. They typically use a stainless steel body with sintered nickel, titanium, or copper powders as the wick.

All heat pipes operate in the two-phase fluid regime, transitioning from liquid to gas. As a result of having gas in a fluid line, pressures can often be much higher as the fluid needs to expand when it changes phase, just like mechanically pumped fluid loops (MPFLs) such as on the ISS [8]. This higher pressure means walls and components need to be thicker and ultimately heavier. While some MPFLs are two phase, other concepts use single-phase fluids [24, 27], unlike LHPs. Single-phase fluid reduces both complexity and places where failures can occur, which is very desirable for complex and expensive missions.

Despite the strong performance, these loop heat pipes have not been demonstrated for very high heat rejection space systems (couple thousand watts) such as the ISS, and this could be because the technology simply does not scale well. Fundamentally, capillary action controls the fluid motion, and while passive mechanisms are often a safe bet, they might not perform the best

compared to other technologies such as a pump which can efficiently transport fluid in a pipe. For higher flow rates, more of the heavy sintered metal wick will be necessary, whereas in a MPFL design, one could possibly just increase the power to the motor to increase the flow. Essentially, at a certain point, it makes sense to simplify the system by just switching the wick with a normal pump to drive the flow for lesser mass.

Another advantage of pumped fluid loops is that the operator/spacecraft has control over the system, and can change the temperature of the spacecraft to be hotter or colder from equilibrium if necessary for certain (albeit unconventional) missions. Furthermore, pumped systems are easily scalable as you can route the tubing to many instruments to collect heat, add more panels for radiation, and swap out a more powerful pump for more heat rejection without needing to add a lot of additional mass.

MPFL technology has flight heritage over many missions. Three rover missions, Mars Pathfinder, Mars Science Laboratory, and Mars 2020 have successfully used this to perform science on the surface of Mars. The Parker Solar Probe uses pumped fluid loops to research the sun, and the ISS keeps the station cool as well. These missions are all over 1000 W because this technology trades well once you get past a certain power requirement threshold.

Overall, the desire to create a high powered scalable solution for future spacecraft lead this work to propose a pumped-fluid-loop design used with the rest of the novel deployable radiator architecture. As well, the proposed design uses thin kinked tubes which require thin walls from reasonable pressures such as those found in single-phase pumped fluid systems.

### 1.1.3  Material Breakthroughs

The novel radiator presented here has been designed to take advantage of advances in material technology. Extremely thermally conductive off-the-shelf pyrolytic graphite sheets (PGS), often used thermally in computer electronics, are configured in a layered architecture for a spacecraft radiator design. These sheets can have in-plane thermal conductivities five times higher than those of aluminum and are even less dense, making them a clear choice to design a novel radiator panel.

Specifically, pyrolytic graphite sheets can have in-plane thermal conductivities ranging between 700-1950 W/m/K [10], with thinner layers performing better than thicker ones. The performance of PGS is only surpassed by diamond at around 2100 W/m/K, and graphene at around 4840 W/m/K [28], although these are all highly affected by the temperature (some elements can get much higher at a few K above absolute zero). Notably, the only materials that outperform these graphite sheets at realistic temperatures are those also made from carbon lattice structures, as diamond and graphene are also structures made from carbon, just like graphite. Graphite sheets are also anisotropic, and have out-of-plane thermal conductivities around 14 W/m/K according to graphene-supermarket.com. However, if adhesive is used to attach layers together as is common, the anisotropic nature is amplified because the adhesive is even more thermally insulating.

It was only recently, some time during the 21st century, that pyrolytic graphite sheets began to be produced on an industrial scale. Following the initial synthetic production of graphite in 1897 [29], thin layers of pure graphite are now available on the market, sold to be used with thermal management systems typically found with computer systems. There are a handful of manufacturers creating this product, and it is easily accessible through online retailers or direct sales.

### 1.1.4 Radiating Fin Heat Transfer

A lack of research exists, however, detailing the use of these layers for the most efficient heat transfer per unit mass in a design. Rectangular profiles, as evidenced by the current technology sandwich panels, do achieve good heat rejection, however, the additional mass at the section furthest from the source of heat only provides limited usefulness, increasing the mass required. As heat travels away from its source, it reduces in temperature through conductive resistance. A small reduction in temperature can lead to significantly less radiative heat transfer leaving that section. So as the radiator material gets further from the source, its ability to reject heat lowers, reducing the efficiency of heat-per-unit-mass of the system. Consequently, the ideal radiator profile would have some optimal max length and some optimal base thickness, taking on some optimal shape to get from the base to the tip of the radiator.

The concept of tapering a heat transfer device has significant history in the field of heat sinks and convective fin design. The transport of heat from a source to an exposed surface for heat rejection is known as fin heat transfer, which confusingly can include both convection and radiation, both of which remove heat from the fin's surface. Convective fin heat transfer has been studied in great detail, and can be found in any general heat transfer textbook. The same conductive principles apply in both cases, however, in the case of spacecraft radiators, radiation happens at the surface in place of convection, and this introduces a fourth-power nonlinear term making solutions more challenging. Heat sink designers often taper their fins, as mass at the tips of the fins are not experiencing the same amount of heat flux through the cross section, and the additional mass is less useful. A tapered radiator can reduce significant mass while performing very similarly to a plain rectangular design. As well, anisotropic effects make a tapered approach ideal because if there are insulating layers such as adhesive between sheets, then the heat from a central layer can reach a radiating surface without having to pass through any insulator. For research into radiator design, few resources were found, but interested readers can look to the textbook on extended surface heat transfer [30] which does go into detail on the mathematics. One tapered radiator design has been considered in the past by NASA researchers in 1964 [15]. However, their work is limited to solid homogeneous radiators, not one which includes layers of highly conductive material with anisotropic properties. Furthermore, in a patent filed by Benthem in 2015 [31], a radiator was conceived of which uses layers of pyrolytic graphite to transfer heat away from a source. This work shows a configuration consisting of conductive and emissive layers, albeit not with an optimal configuration: one which forgoes ineffective mass. This paper will illuminate the performance of a tapered and layered design, combining these two aspects to try and come up with a solution that approaches an optimal yet realistic design.

## 1.2    Examples of and Necessity for Deployment on Spacecraft

Deployable space structures have history in many missions, ranging from deployable solar panels, antennae, booms, and radiators. They are used to extend the capabilities of a craft by

creating surfaces larger than otherwise possible. With limited size launch vehicles, space and volume requirements can be a bottleneck on a design, as we have seen spacecraft such as James Webb Space Telescope can be limited to payload fairing sizes. In fact, SpaceX is planning on extending its fairing to allow for larger modules to be sent for the Lunar Gateway project [32]. Accordingly, it can often make sense to look at not only heat rejection per unit mass, but also stowed volume.

Examples of deployable solar panels include NASA's Insight Lander, the GPS satellites from Lockheed Martin, and the Juno spacecraft, with heritage going back to some of the earliest satellites like the Ranger satellites. Many of the larger spacecraft like the ISS and GPS satellites use a zigzag or z-folded architecture to easily stow and release panels [33].

Examples of deployable antennae concepts can be found dating back to the 60s as well [34], with spacecraft such as the Canadian Alouette 1 demonstrating tape spring antenna deployment, and others like the Mars Express, whose flight heritage history is neatly summarized along with high strain composite booms from Murphey in 2015 [7].

Solar sail concepts have also utilized deployable boom technology to unfurl their sails [35].

However, deployable radiator designs do not have much flight heritage apart from the Space Shuttle and the International Space Station [8], although others have been designed and tested. Roll-out radiator designs were proposed in the early 80's from Cox and Leach [36], and now followed up with prototypes by Yendler in 2020 [37]. Other recent designs include the European Space Agency's alphabus program [38] whose platform has expanded to include research from Lecossais [5] and Verdonck [39]. Other radiators have been conceived of such as Goncharov and Perroto's DPR design from 2000 [40], Ding 2017 [9], Ambrose 2019 [6], and van Lierop's 2021 cubesat deployable radiator concept [13]. The upcoming James Webb Space Telescope will also use deployable radiators [41], along with the rest of the generally deployable structure, to fit into the Ariane 5 rocket fairing.

Many deployable radiator concepts come from higher-temperature nuclear-powered spacecraft or surface missions. These extremely high-power missions have issues fitting radiators within

a launch vehicle [42] and it would follow that deployable solutions are the way forward. The Prometheus project, proposing the Jupiter Icy Moon Orbiter from JPL in 2005 [43] kicked off development in the U.S. to research the designs that would enable nuclear propulsion. Nuclear powered surface missions extended after this from Siamidis and Ellis in 2006 and 2011 developing radiator designs for a lunar mission [44, 45], and from NASA in 2010 with an initial concept definition [46]. More recently, Tomboulian in 2014 reviews this prior work and models performance from a nuclear-electric propulsion radiator using a combined heat-pipe and fluid-loop design, although they do not specify the deployment method for their concept.

# Chapter 2

# Details on Proposed Deployable Radiator Architecture

## 2.1 Overview of the Proposed Deployable Radiator System

The proposed deployable radiator architecture discussed below represents a preliminary feasible design concept that could be used to save mass on certain high-power spacecraft missions. The primary goal was to reduce the amount of mass, while still ending up with a high-power deployable radiator solution that is scalable to reject large amounts of heat from a small region taken up on the external surface of a spacecraft.

This section will briefly outline the major systems involved, talk about the operation of the design, and detail the novel radiator panel and the thermal analysis leading to the selection of the geometry thereof. Then, the deployment system will be explored in detail, followed by a thermal analysis for the overall pumped-fluid-loop system used to determine the performance.
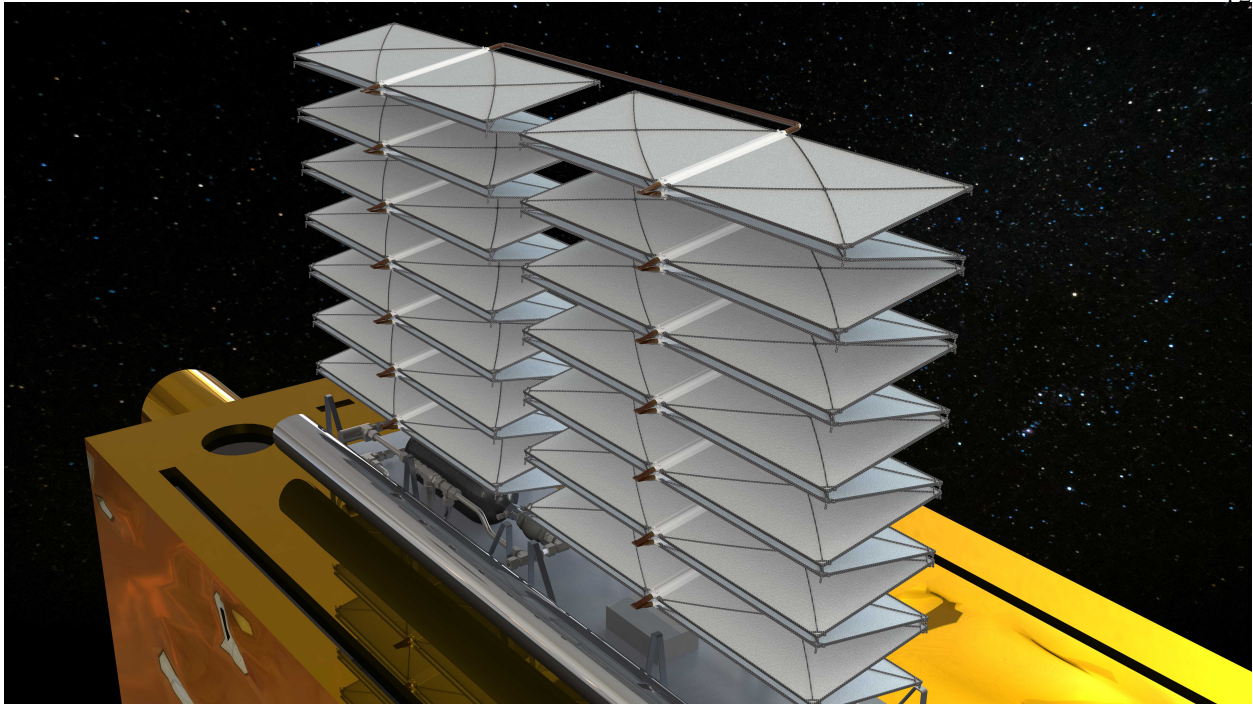
Figure 2.1: Deployment of stacked radiator panels in the stage of partial extension

### 2.1.1  Operation of the System to Reject Heat

The radiator system begins in a packaged configuration with two sets of 14 stacked panels on top of one another. They are connected using thin polyimide (Kapton HN, DuPont) tubes that can fold, or kink, while the panels are stacked. These tubes are set up to be able to deploy the panels in a z-folded pattern, in a similar manner to how many solar arrays are deployed [33]. These tubes allow fluid to flow into the radiator panels and transfer heat to the radiators. In the packaged configuration, a sheet of aluminized BoPET (Mylar, Dupont) restrains the stacked panels, ensuring enough compressive force to prevent motion during a launch. The undeformed configuration of the sheet is rolled into a small diameter tube, and it is kept in place by a Vectran, Kuraray, cord. Thermally cutting the cord with electric heating, the restraining sheet retracts driven by its strain energy, revealing the stacked radiators. In the microgravity environment, these panels will then partially extend, as the elasticity of the thin tubes creates a bending moment at their joints. A render of this process is shown in Figure 2.1 below.
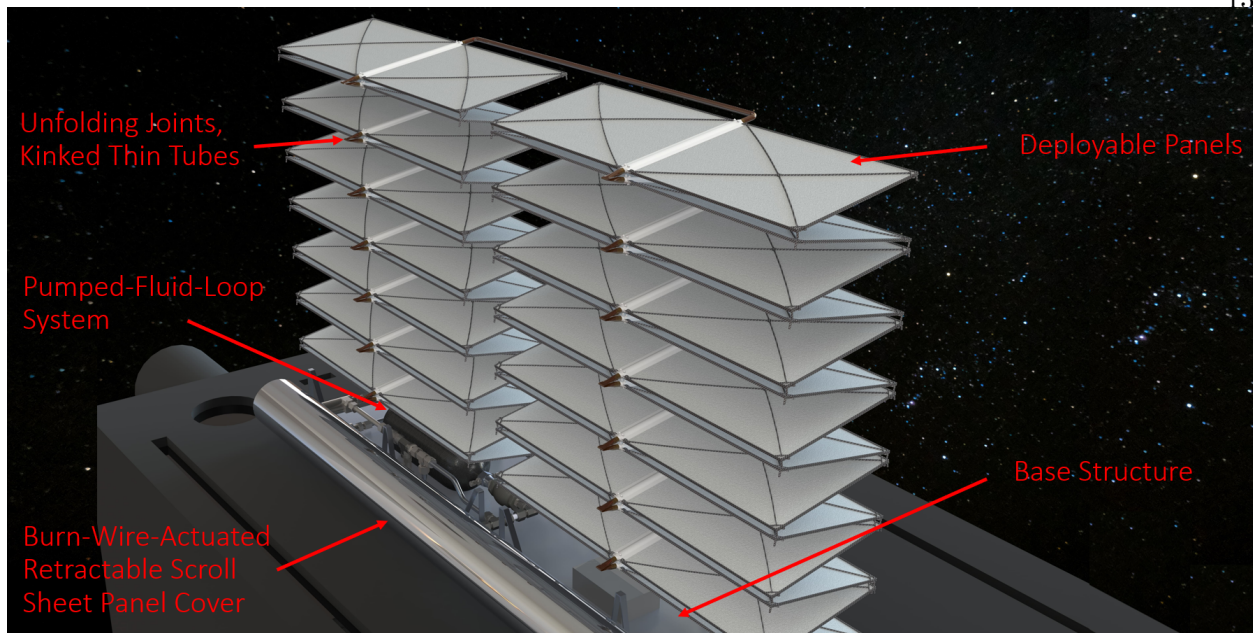
Figure 2.2: Labeled diagram of the deploying radiator panels showing the major subsystems

A valve is then opened, and pressurized fluid pushes through the tubes and radiators, pressurizing the joints between the panels. This increases the bending moment at the joints, which results in the deployment of the panels even without other additional hinges. In the final deployed configuration, the panels are all parallel, maximizing the exposed radiation surfaces. A pump is then turned on and the fluid begins to flow through the system, transporting the heat from inside the spacecraft to the radiators for rejection to the space environment. An image of the fully extended system is shown in Figure 2.3 below.
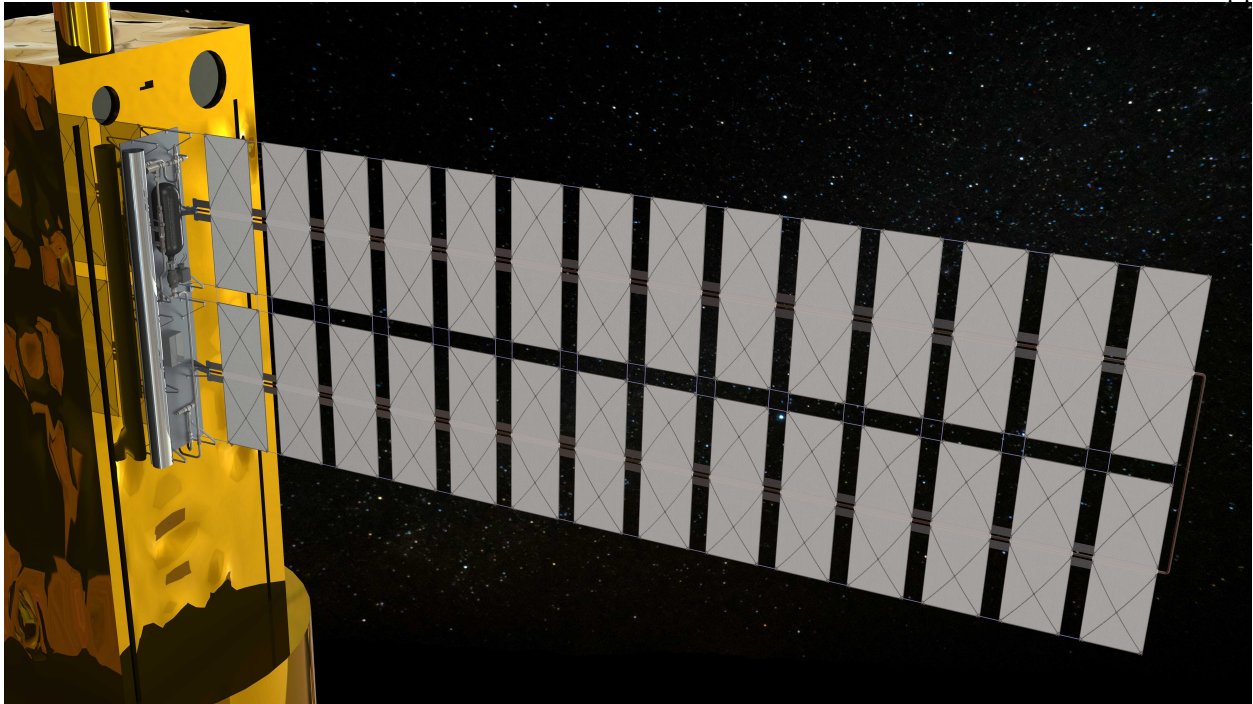
Figure 2.3: Deployment of stacked radiator panels in the stage of full extension. Included here are hinges and rope connecting panels together.

Here, additional ropes are included to constrain the two sets of panels to deploy together. As well, hinges are shown here because additional stiffness was found to be required in order to match the fundamental frequency requirements for typical deployable-panel spacecraft.

### 2.1.2    Layout and Dimensions of the System Design

In the packaged configuration, the boxed volume is 0.108 m$^3$, with length height and width being 1.307 x 0.319 x 0.259 m respectively. After being deployed, the radiator panels extend to 3.82 m.

## 2.2    Proposed Radiator Panel Design

### 2.2.1    Layout and Dimensions of the Final Panel Design

The thermal performance of a section of radiator is proportional to the fourth power of the panel's surface temperature. Consequently, the primary objective is to reduce thermal resistances in

the network which drops the temperature before reaching the radiating surface. However, this target must be balanced with the structural aspects of a design as well, providing a realistic minimization to the thermal resistance in the system. Note that this design is meant to be incorporated separate from the main structure of a spacecraft, and this is important because this technology will only be beneficial in mass reduction if the surface area of the craft is not already enough to match thermal loads at an acceptable temperature.

Here, a schematic of the proposed new radiator panel is shown in Figure 2.4. Pyrolytic graphite sheets are stacked in layers, tapering towards the end of the panel, reaching out from the central heat source. In a configuration as a deployable radiator panel, this design can operate from both sides, top and bottom, symmetrically as depicted. Alternatively, as a static structure, this could also be used in a single-sided configuration. If this is the case, then the structure should change to match the mating location. As it has been designed, a central clamping tube bracket transfers the heat while also maintaining the structural rigidity of the layers through a cross-braced carbon fiber frame fastened to the central bracket.
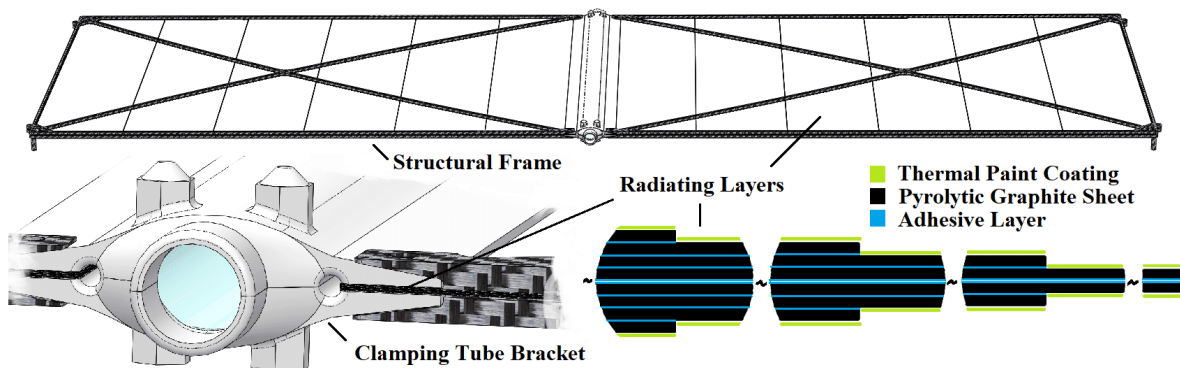


Figure 2.4: Radiator panel design. Top: panel assembly. Bottom Left: close-up of the structure clamping the radiator layers. Bottom Right: a diagram of the PGS layer stack with adhesive layers and thermal paint

This model can also be viewed in detail as a 3D-PDF object in Appendix A. The central tube structure depicted was designed to be used in a single-phase pumped-fluid-loop system, but could be generalized for any design. Strategically, this design clamps the stacked layers providing

good thermal contact using the elastic nature of the aluminum clamping bracket with a bending arm geometry. The internal tube section of this bracket conducts heat from a source, whether that is a fluid, a heat pipe, or some other source. Any design which utilizes these highly conductive and thin pyrolytic graphite sheets is going to face challenges assembling the structure while reducing the thermal resistance pathway since a constant force is desired at the surface to ensure thermal contact over the lifetime of the part. Many iterations were involved to create a structure that can flex, maintain thermal contact, and be manufactured while keeping mass at a minimum. A two-piece clam-shell manufacturing method is proposed with milled aluminum by slicing the design in half and epoxying together the pieces while clamping the structure in a weighted jig for curing. With this method, contact force can be controlled for repeatable results. Alternative designs using many spaced fasteners to provide the contact were considered, however, the contact force would be inconsistent between the fasteners, and weight and complexity increases.

### 2.2.1.1    Panel Dimensions

The length, width, and height of the two-wing assembly seen in Figure 2.4 is 624 x 11.0 x 214 mm.

The internal tube section is an ellipse of major diameter 12.0 mm and minor diameter 6.0 mm, with a minimum wall thickness of 1.0 mm all around. This section then tapers to meet the stacked radiating layers, with the top section having a cutout for the passive clamping of the layers. The front and back of this part have cylinders for attaching thin tubes for a pumped-fluid-loop system using epoxy. These cylinders are 5 mm deep before tapering to match the elliptical shape, with an outer diameter and thickness of 7.6 mm and 1.6 mm respectively.

There are six layers of 25 $\mu$m thick PGS with a maximum length of 300 mm spaced 50 mm apart, and each layer having a 10 $\mu$m thick adhesive backing. This adhesive was found to be necessary because the graphite alone is very thin, easily damaged, and tears readily, as discovered from handling samples from suppliers. Together, the two symmetric halves of the layers total 0.42 mm. Indium foils 50 $\mu$m thick are to be placed in the contact regions between the clamping bracket

and the layers since this thermal interface material is conductive and ductile even at cryogenic temperatures. This brings the total thickness to be clamped at 0.52 mm in a 0.47 mm space to allow the load to be applied through the layers as the two halves of the tube cure in place. This design purposefully leaves a gap at the fluid section for the epoxy to seal up in order to achieve the desired clamping force at the layers.

The 4x structural frames are 1.6 mm thick and cover the layers in a cross shape to prevent bending during launch accelerations and G-loads. From a top-down view, the width of the frame cross and edges are 1.4 mm, with additional bracing in the corners.

In summary, this design features unique tapered and layered aspects which the structure needs to accommodate. Depending on the application and thermal environment, this design will have a different optimal geometry than what is given above, and the process of optimization is explored below.

### 2.2.2    Justification for the Structural Design Decisions

The design of the clamping tube bracket (CTB) involved numerous iterations to come up with a concept that would ensure good thermal contact, eliminate the need for heavy fasteners, and be capable of fabrication. Initial one-piece designs involved machining arms that would clamp the PGS layers together using only the elasticity of the aluminum metal. One benefit of this design is that it would ensure a sealed CTB made from a single block of material. However, the gap between arms would be a thin slit, and tolerances of 0.1 mm for wire EDM fabrication meant that the PGS layers would either be too small or too large, ruining the thermal contact. Further, opening that gap to slide the layers in would require additional mass, since the arms would likely be too small to grab onto easily.

The new two-piece clam-shell design solves these problems as long as it can be properly sealed. By curing the two pieces in place while under load, it ensures the arms compress against each other and consequently the layers. The clam-shell sections can be machined using milling and turning, and even allow for hand lapping of the mating surfaces to enable precise fits. Although,

with the addition of indium foil strips, this step will not need to be as precise. In section 2.4.1 below, these two clam-shell halves can be seen aligned with the press jig structure.

The clamping tube bracket has four holes in the arm's corners. These serve three purposes, first, they aid in the alignment of the assembly for the press jig structure with the use of pins, and second, they allow alignment to the composite frames. Lastly, they can be filled with epoxy to ensure solid mounting points from the frames to the bracket, to the layers.

Other pin structures can be seen in Figure 2.4, at four corners of the frames, and along the top and bottom ends of the CTB. These pins are tapered on the ends, and allow the packaged radiator assembly to stack neatly, preventing motion during vibratory launch conditions. The tapered pins fit into corresponding conical regions to achieve this locating effect.

The frames utilize a simple cross structure to brace loading in the planar direction of the layers. Adding these helps to ensure in-plane loads do not transfer to the thermal PGS layers, avoiding potential damage. As well, this additional material increases the stiffness against bending, and section 4.3 shows that altogether, this structure is sufficient to withstand expected worst-case handling loads, as well as vibration.

Finally, this design assumes that epoxy rated for outgassing is used for the composite carbon fiber frame and the clamping tube bracket clam-shell connection.

## 2.3    Modelling the Thermal Performance of the Radiator Panel

Initial optimization work was done using Finite Element Modelling with Solidworks Simulation thermal analysis package. Here, the desired performance metric was defined to be watts per kg, however, a penalty mass model needed to be created to realistically compare different cases. Later, triangular mathematical models were used to characterize the performance of the selected geometry, and to understand the effect of insulative adhesive used between PGS layers.

### 2.3.1    Penalty Mass Model

To find the optimal shape of the radiator, it is important to characterize the negative impacts of scaling a design. For example, as a radiator grows in length, it has to account for the increased mass of the extended layers. Similarly, if the radiator layers grow in height, then additional structure must surround the layers, and this must be included too. Finally, the mass of the panel's structure and fluid must also be accounted for in every unit length deep (width) the radiator grows. Otherwise if this penalty mass were to not be included, the optimal radiator would be no length at all, and it would be able to radiate from the source of heat's surface with no mass - which is unrealistic. Consequently, an equation for penalty mass was used and held constant across different trials using early estimates of the bracket geometry. A depiction of the sections included in the penalty mass is shown in Figure 2.5.
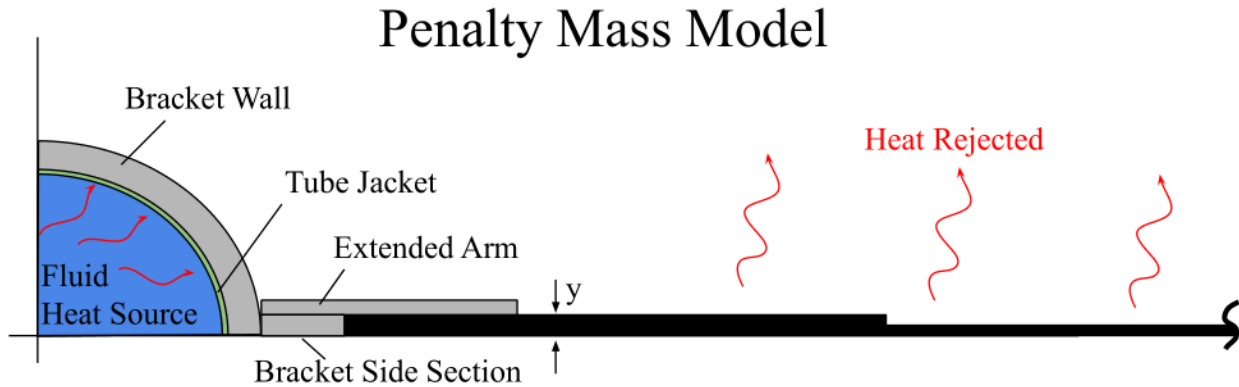


Figure 2.5: Diagram of the components used for penalty mass calculations when scaling the geometry of the layers

Early on, it was found that a clamping tube bracket (with similar geometry to the one shown) had a very small thermal drop from transferring heat from the internal fluid-wall surface to the extended arms, reducing the temperature by 0.1 K while rejecting over 1000 W of heat. This suggested that while the structure's penalty mass would be critical to the optimization, the bracket's effect on thermal resistance is essentially negligible, at least when it came to optimizing the layered geometry.

With the finalized clamping tube bracket, however, an average temperature drop of 1.2 K happens across the arms of the radiator panels from hand calculations assuming 50 W per panel. This is one area that could be optimized in future work, looking at whether it could be worthwhile increasing the thickness of the CTB for small thermal gains.

### 2.3.2    Early Justification

Two different geometries were used in the early simulations with estimated dimensions for PGS layers and aluminum radiators in Table 2.1 below. First, layers of constant thickness were constructed and stacked next to each other with a small gap in between. These were either all the same length or the first layer was cut in half representing a simple taper. Second, solid triangular geometries were used for aluminum, as this material does not have to be comprised of layers like PGS. For the selected aluminum geometries, versions were tested with shorter lengths or thicker bases.

Through finite element analysis with Solidworks, it was found that early, non-optimized, tapered aluminum geometries initially tested were underperforming PGS designs of similar proportions, see Table 2.1, cautiously validating the hypothesis that PGS would perform better. The parameters used for these designs are listed in this table as well, such that the simulations could be recreated. Note that these results only include the mass of the layers and the penalty mass, not the system to carry the heat to this location (such as pumps, deploying structure, etc), which would be much larger. The option of including internal radiation between layers was added as well, which as expected, improved performance marginally by adding a parallel pathway for some heat to flow.

In these models, 0.1 mm was used as the width of the mesh, chosen for computational efficiency because of the assumption that the results are constant along the width of the radiator (ignoring edge effects). These parameters and computed values are scaled up for a 200 mm wide panel to make comparisons easier. The thermal conductivity was chosen as 1300 W/m/K to correspond to the layer thickness, as a thicker PGS can dramatically reduce the value for thermal

conductivity [10].

Note that these simulations represent a single quadrant of a radiator panel, symmetric on two axes.

Table 2.1:   Initial Thermal Simulations PGS vs Aluminum

| Simulation Code | PGS1 | PGS2 | PGS3 | ALUM1 | ALUM2 | ALUM3 |
|---|---|---|---|---|---|---|
| Material | Pyrolytic Graphite Sheet | Pyrolytic Graphite Sheet | Pyrolytic Graphite Sheet | Aluminum | Aluminum | Aluminum |
| Geometry | Single rect. layer | 2 layers (top cut in half) tapered | 3 layers (top cut in half) | 5 layers (top cut in half) | Solid tapered triangle, thin | Solid tapered triangle, Long |
| Internal Radiation | none | none | cut surface +1 layer | cut surface +3 layers | N/A | N/A |
| Num of effective layers | 1 | 2 | 3 | 5 | N/A | N/A |
| Max length [mm] | 200 | 200 | 200 | 200 | 200 | 161.5 |
| Gap Between Layers [mm] | 0.001 | 0.001 | 0.001 | 0.001 | N/A | N/A |
| Max height [mm] | 0.3 | 0.3 | 0.3 | 0.3 | 0.242 | 0.3 |
| Width [mm] | 200 | 200 | 200 | 200 | 200 | 200 |
| Base temp [K] | 300 | 300 | 300 | 300 | 300 | 300 |
| Layer thickness [mm] | 0.0255 | 0.0255 | 0.0255 | 0.0255 | N/A | N/A |
| Thermal Conductivity (in plane) | 1300 | 1300 | 1300 | 230 | 230 | 230 |
| Thermal Conductivity (vertical) | 14 | 14 | 14 | 230 | 230 | 230 |
| Density of Layers [kg/m$^3$] | 1700 | 1700 | 1700 | 2700 | 2700 | 2700 |
| Slope L/h if triangle | N/A | N/A | N/A | N/A | 826 | 538 |
| Radiating Area [m$^2$] | 0.0400 | 0.0400 | 0.0400 | 0.0400 | 0.0400 | 0.0323 |
| Layer/Sheet Mass [kg] | 0.00173 | 0.00260 | 0.00434 | 0.01239 | 0.01307 | 0.01308 |
| Penalty Mass [kg] | 0.0166 | 0.0167 | 0.0167 | 0.0168 | 0.0169 | 0.0169 |
| Total Mass [kg] | 0.0184 | 0.0193 | 0.0210 | 0.0291 | 0.0299 | 0.0300 |
| Heat Rejected [W] | 7.77 | 9.60 | 11.34 | 7.20 | 9.48 | 9.44 |
| **Heat per Mass - panel [W/kg]** | **423** | **498** | **539** | **247** | **317** | **314** |

The results of the first two columns show that tapering (removing top layer mass and adding a second layer beneath) was indeed optimal in increasing performance. In fact, this change even increased total heat rejected compared to a single layer design since a single layer obscures layers below from the external environment. These initial results justified the design choice of using PGS and further optimization was conducted to find the best geometry.

### 2.3.3    Evaluating Two Mathematical Models and the Effects of Anisotropy

Two mathematical models were derived from the first law of thermodynamics to analytically solve the temperature for a triangular geometry and show that the finite element analyses are accurate. Two models were formed because of the need to understand the contributions from the anisotropic nature of a layered structure. The first equation, a nonlinear differential equation, was derived from the assumption of vertically isothermal layers (thin enough to remain at the same temperature). The second was modeled off the assumption of infinite insulated layers, representing the case of a perfect insulator between extremely thin sheets. With a design that requires insulating

adhesive between layers of PGS, the question was posed: which model is correct, how different are the results, and under what circumstances should the models be used? It was expected that the isothermal case would be accurate since the layers are only 25 $\mu$m thick and the finite element simulations seemed to be a constant temperature, but it was also known that the early finite element simulations did not have many nodes vertically, especially with the large aspect ratio of the design.

The diagrams for each model are included in Figure 2.6 with their respective equations below. The steps to derive the insulated layer model include equating the heat flow from conduction to the heat flow due to radiation and rearranging. This assumes thin rectangular layers that become a triangle when enough thin layers are stacked together. For the vertically isothermal model, a small element is drawn with radiation leaving, and heat flow at x and x+dx at the left and right boundaries respectively. Using taylor series expansion, removing higher order terms, replacing the heat flow with fourier's law of conduction for an arbitrary area, and equating to radiative heat transfer the insulated layer model can be found.
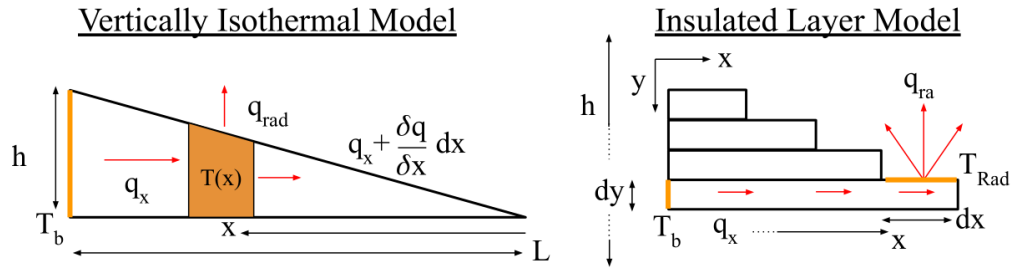


Figure 2.6: Diagrams of the vertically isothermal and insulated layer models for a triangular radiating fin

Vertically Isothermal Model:

$$\frac{kh}{L\sigma\epsilon} \cdot \frac{\partial}{\partial x}\left(x \cdot \frac{\partial T(x)}{\partial x}\right) - T(x)^4 = 0 \tag{2.1}$$

Insulated Layer Model:

$$\frac{T_b}{T_{rad}} = 1 + \frac{x\varepsilon\sigma}{k}\frac{dx}{dy}T_{rad}^3 \tag{2.2}$$

Here, k is the in-plane thermal conductivity, x is a distance as shown for each (defined in

opposite directions for equation simplicity), $\sigma$ is the Stefan–Boltzmann constant, and $\varepsilon$ is the emissivity. $q_x$ is the heat flowing through the material and $q_{rad}$ is the heat radiating to space. For the insulated model, $T_{rad}$ is the temperature at the end of a layer, but it could also be thought of as the top triangular surface. For the isothermal model, dx is the infinitesimal thickness of the section of the radiator, and for the insulated model, $dx$ is the exposed infinitesimal distance for that layer and $dy$ is the layer height. Both these triangular models have base temperature $T_b$ , base height h, and maximum length $L$. The assumption was made that these radiators are purely exposed to space at 0 K.

Solving the isothermal model required a shooting algorithm combined with a boundary-value-problem numerical solver using the command bvp4c in Matlab, as well as the assumption of a thin radiator. Here, mixed boundary conditions were used: heat flow at the tip of the triangle was zero, and temperature was held constant at the base.

The layered model was much easier since it did not need to solve a continuous problem; each layer is independent of the rest. It took a simple iterative solver to find $T_{rad}$ at every point along the surface.

These models were solved and compared against identical triangular geometries solved with Solidworks simulations. These simulations were repeated using different values of anisotropic thermal conductivities. Anisotropy is typical of these pyrolytic graphite sheets, with an out-of-plane conductivity of around 14 W/m/K according to graphene-supermarket.com, compared to the in-plane 1500 W/m/K used for this design [11]. Furthermore, the introduction of interstitial adhesive layers changes the out-of-plane thermal conductivity between layers, and the significance of this was investigated through the use of these finite element models. See Figure 2.7 below for the results. Here, a base temperature of 300 K was held constant, an emissivity of 1, and the maximum length 200 mm, except for the final plot which matches the current design with an emissivity of 0.89 and length 300 mm.
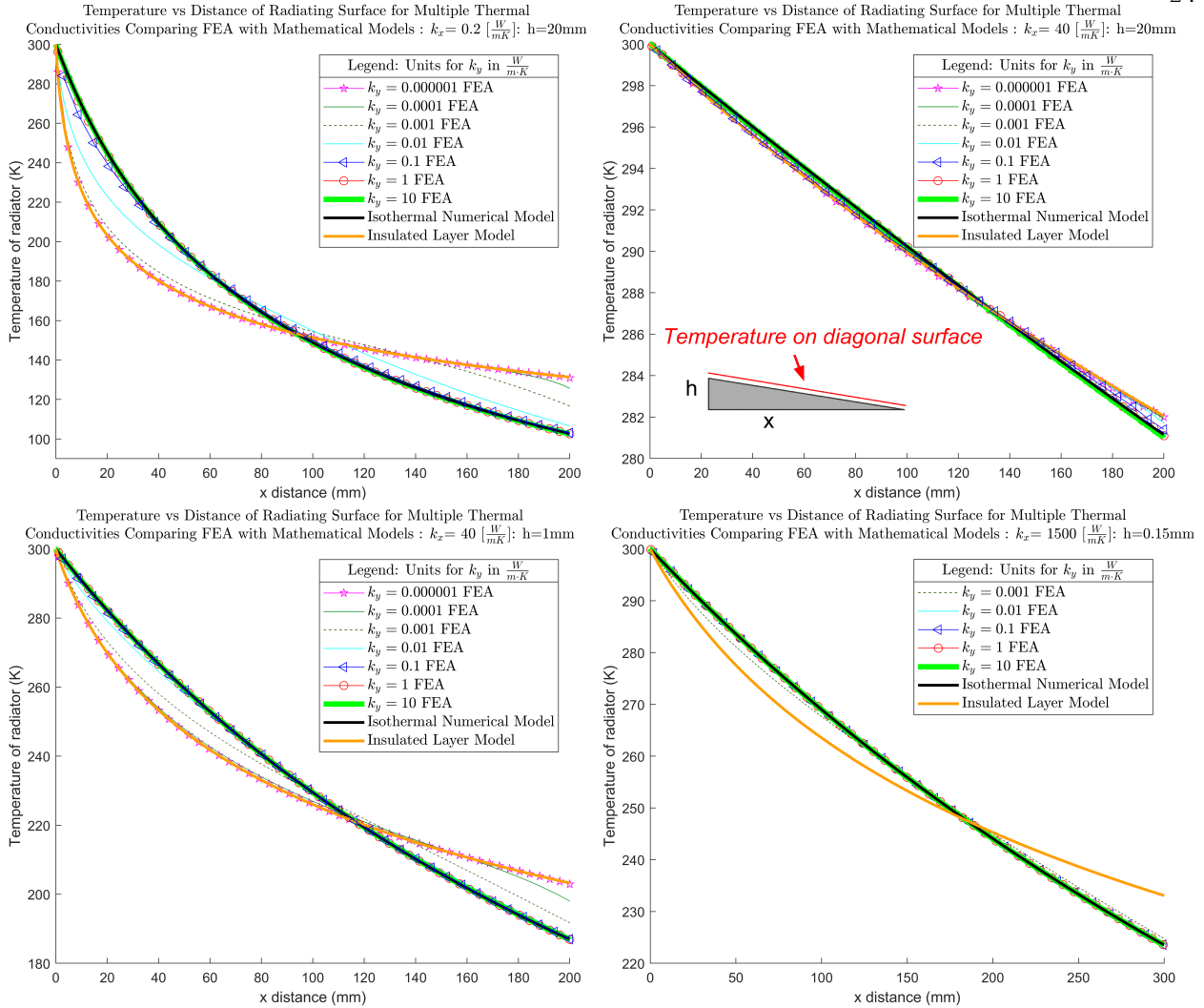
Figure 2.7: Temperature over distance graphs for a triangular panel radiating heat from the top surface. Anisotropic thermal conductivities in finite element analyses are compared against two mathematical models, bounding the solution space

Note that the bottom right subplot does not include all of the finite element analyses; the extremely small thermal conductivities were too computationally expensive to be solved with the thin and high-aspect-ratio geometry.

We can conclude from these results of the graphs:

(1) As in-plane thermal conductivity increases, the two different models collapse onto each other. This is presumed to be a result of the temperature drop becoming negligible as heat is easily transported.

(2) As height decreases, the two mathematical solutions separate, again presumed to be a result of the temperature drop becoming non-negligible as heat is less easily transported.

(3) With opposing factors at play, we find that the models do very closely match each other for the real case with 1500 W/m/K

(4) At anything but negligible out-of-plane thermal conductivity (0.001 W/m/K and below), we see that the finite element results match the isothermal solution almost exactly. And when the thickness decreases and conductivity increases, it can handle even lower out-of-plane thermal conductivities before diverging from the isothermal model. These results show that it is a good assumption that a triangular radiator follows the isothermal model when the dimensions are long and slender, with extremely high thermal conductivity in x, and practically any thermal conductivity in y. This result is expected to be a good proxy for stepped layers like the current design, which adds additional highly conductive mass compared to the triangular analyses above which can only increase heat rejection. Furthermore, the adhesive between layers has an out-of-plane thermal conductivity of up to 0.60 W/m/K such as 3M 8805, which is high enough to match the isothermal model.

The isothermal model of the current radiator design radiator (such as the lower right plot) produced 14.4 W, whereas the insulated layer model produced 13.6 W, from one side - a difference of 5.5 %. For the panel's 4 quadrants, multiply these numbers by 4 to get 57.6 W and 54.5 W respectively. For these heat rejection results only, emissivity was changed to be 0.89 matching AZ-400-LSW white thermal paint from AZ Technology. The max length of the radiator in this graph is 300 mm, base height totaling the 6 x 25 $\mu$m sheets, and width 200 mm - all parameters matching the aforementioned design with the hindsight of having the geometry finalized.

It should be noted that while heat is proportional to the slope of the temperature along a direction, these charts are misleading in the sense that they show only the temperature at the top surface, not the temperature profile of the base, or the internal material. Since radiation is a fourth power relation to temperature, it is much more important that the surface temperature remains

high for a longer distance, as evidenced by the isothermal model outperforming the insulated model in heat rejection, despite the two models' curves intersecting partway through.

While analyses and equations such as this isothermal model are not new [30], this work does help to illuminate the effect of anisotropy on the result, enabling designers to understand exactly when it can be assumed negligible and giving further confidence to future designs. This work provides the bounds to which heat transfer must lie between - at least for a triangular design. Regardless of the exact anisotropy of this design, the two mathematical models only differ in heat rejection by 6 %.

The code used to solve these equations can be found in Appendix B.

While it would be straightforward to program an iterative scheme to find the optimal geometry through the isothermal model above, finite element simulations had already been computed by the time the model was finalized. Realistically, the isothermal model approach should be used to find the optimum design faster and more accurately than trying many finite element simulations. However, this model is limited to the assumption of perfectly triangular designs instead of the realistic staggered layer approach and more work needs to be done to characterize the validity of this assumption. With thin and numerous layers, it should be a good and slightly conservative assumption for heat rejection. The staggered design's mass can still be used in the heat per mass performance metric.

### 2.3.4    Iterating Finite Element Models to Finalize Geometry

With the confidence in the Solidworks finite element simulations, this software was used to compute the thermal performance of many different PGS geometries.

Length and height were independently varied, and a design was approaching an optimal solution. See Table 2.2 below for the parameters used in the simulations, as well as their results. The first three columns look at the effect of changing length, the middle three look at height, and then the final three change length again, but now with a realistic staggered layered geometry instead of the triangular one. Again, these simulations represent a single quadrant of a radiator

panel.

Table 2.2:   Analyses for Optimizing Layered PGS

| Simulation Code | PGS4-tri-L | PGS5-tri-L | PGS6-tri-L | PGS7-tri-h | PGS8-tri-h | PGS9-tri-h | PGS10-L | PGS11-L | PGS12-L |
|---|---|---|---|---|---|---|---|---|---|
| Material | PGS | PGS | PGS | PGS | PGS | PGS | PGS | PGS | PGS |
| Geometry | Triangle | Triangle | Triangle | Triangle | Triangle | Triangle | Stag. Layers | Stag. Layers | Stag. Layers |
| Internal Radiation | N/A | N/A | N/A | N/A | N/A | N/A | none | none | none |
| Number of layers | N/A | N/A | N/A | N/A | N/A | N/A | 10 | 10 | 10 |
| Max length [mm] | 412 | 500 | 300 | 412 | 412 | 412 | 280 | 300 | 320 |
| Gap Between Layers [mm] | N/A | N/A | N/A | N/A | N/A | N/A | 0.005 | 0.005 | 0.005 |
| Max height [mm] (w/o gaps) | 0.094 | 0.094 | 0.094 | 0.080 | 0.100 | 0.130 | 0.100 | 0.100 | 0.100 |
| Width [mm] | 200 | 200 | 200 | 200 | 200 | 200 | 200 | 200 | 200 |
| Base temp [K] | 300 | 300 | 300 | 300 | 300 | 300 | 300 | 300 | 300 |
| Layer thickness [mm] | N/A | N/A | N/A | N/A | N/A | N/A | 0.010 | 0.010 | 0.010 |
| Thermal Conductivity (in plane) [W/m/K] | 1950 | 1950 | 1950 | 1950 | 1950 | 1950 | 1950 | 1950 | 1950 |
| Thermal Conductivity (vertical) | 14.0 | 14.0 | 14.0 | 14.0 | 14.0 | 14.0 | 14.0 | 14.0 | 14.0 |
| Density of Layers [kg/m$^3$] | 2130 | 2130 | 2130 | 2130 | 2130 | 2130 | 2130 | 2130 | 2130 |
| Slope L/h if triangle (w/o gaps) | 4389 | 5331 | 3199 | 5146 | 4116 | 3166 | 2800 | 3000 | 3200 |
| Radiating Area [m$^2$] | 0.0823 | 0.1000 | 0.0600 | 0.0823 | 0.0823 | 0.0823 | 0.0560 | 0.0600 | 0.0640 |
| Layer/Sheet Mass [kg] | 0.00822 | 0.00998 | 0.00600 | 0.00702 | 0.00876 | 0.01140 | 0.00656 | 0.00703 | 0.00750 |
| Penalty Mass [kg] | 0.0167 | 0.0167 | 0.0167 | 0.0167 | 0.0167 | 0.0168 | 0.0167 | 0.0167 | 0.0167 |
| Total Mass [kg] | 0.0249 | 0.0267 | 0.0227 | 0.0237 | 0.0255 | 0.0282 | 0.0233 | 0.0238 | 0.0242 |
| Heat Rejected [W] | 16.09 | 16.79 | 14.67 | 15.13 | 16.48 | 18.13 | 14.54 | 14.86 | 15.14 |
| **Heat per Mass, panel [W/kg]** | **645** | **629** | **646** | **638** | **647** | **644** | **624** | **626** | **625** |

Notably, the thermal conductivity here is higher than in Table 2.1 because thinner layers are included. This is not as important a factor to the result for efficiency (W/kg) as compared to the changes optimizing the geometry.

In the end, the final design's length was chosen to be 300 mm since it had superior performance. However, the PGS thickness was increased to 6x 25 $\mu$m layers totaling 0.15 mm. This change was made because an adhesive layer was empirically found to be required since plain PGS was too brittle to handle. Having 10 additional $\mu$m of adhesive per layer (which suppliers insisted was the minimum thickness possible) would certainly increase the weight of the system. It was also known that by changing the penalty mass to be higher, this shifted the optimal design to become thicker, and with the additional mass of adhesive and likely future structural mass creep as well, the decision was made to use a total of 0.15 mm of PGS from ProGraphite [11].

Now with the geometry finalized, the results are provided. The design weighs 125.9 g (24.9 g for the frames, 52.1 g for the layers with adhesive, 36.2 g for the bracket, and 12.7 g for the fluid), and the expected heat rejection for the panel (assuming 300 K base temperature, 0.89 emissivity) was found to be 60.5 W (57.6 W as mentioned from the previous isothermal model, with an additional 2.9 W from the clamping bracket radiating heat at 300 K). This corresponds with a heat-per-unit-

mass ratio of 481 W/kg for an individual panel - not far off the final numbers for the second last column of Table 2.2. The difference between the design-predicted and the estimated Table 2.2 efficiencies results from: first, the guess of the penalty mass geometry as an approximate model that was used before the final design was settled upon; second, the 11% reduction of emissivity from the black-body radiation case; finally, a reduction of thermal conductivity after selecting the specific PGS material. Concerning the previous penalty mass model, the current design has a mass-per-unit-width of 0.37 kg/m without considering the mass of the layers, while the penalty mass model itself had a value of 0.33 kg/m, a 12% decrease in part because it lacked structural frames.

To note, the predicted panel heat rejection should be moderately conservative because the value was determined using a triangular radiator model with less material than the realistic rectangular-stepped-layer approach: more material would reduce the thermal resistance and consequently increase heat rejection.

## 2.4    Realistic Radiator Panel Prototype

A realistic single-panel prototype was created to demonstrate the feasibility of manufacturing such a design and having it be structurally sound. While thermal vacuum tests would be ideal using this realistic prototype, (and necessary for further integration on an actual mission), this testing was not conducted due to a lack of time. Similarly, vibration testing on a panel would be good to conduct on this prototype, but it was outside the scope of this thesis.

Of primary concern, one of the primary drivers in this technology is the extremely thin pyrolytic graphite sheets. Structurally, thermally integrating these thin sheets can be challenging, and a realistic prototype demonstrates that a layered and tapered radiator panel can be built, and holds up (at least under its own weight). This prototype does not address how these panels will fare under the launch vibrations with many stacked on top, but this is left for future work to confirm that they will survive.

Shown in Figures 2.8 and 2.9 below are two images of this full-scale panel design.

Figure 2.8: Top view of the radiator panel prototype



Figure 2.9: Close up of the radiator panel prototype

Note that the prototype has additional structure along the clamping tube bracket which was added for CNC milling manufacturability. These would realisticlly be removed before use. Furthermore, the alignment pegs on either end would be extruded and indented in a conical mating fashion for stacking the panels during launch.

In the beginning, initial samples of PGS were acquired without adhesive from Panasonic's catalog [10]. It was informally determined that these layers of thin graphite sheets were too fragile to handle without the adhesive backing that most sources provided with it. An image is included below showing what happened when a adhesive-less sheet accidentally caught a piece of tape and ripped immediately while being removed from packaging. This result, along with even the flexibility of the adhesive-backed sheets, confirm Maas' comments in 2017 [12] that pyrolytic graphite sheets require structural support.

Figure 2.10: PGS without adhesive backing that ripped immediately after pulling it out of its package

### 2.4.1    Assembly Process for Realistic Panel Prototype

Assembly of the radiator panel involves a step-by-step process to have the layers properly clamped in place. Good mechanical contact is required for optimal thermal performance. Below is an image of the major sections of the press jig used to clamp and cure the design in place.
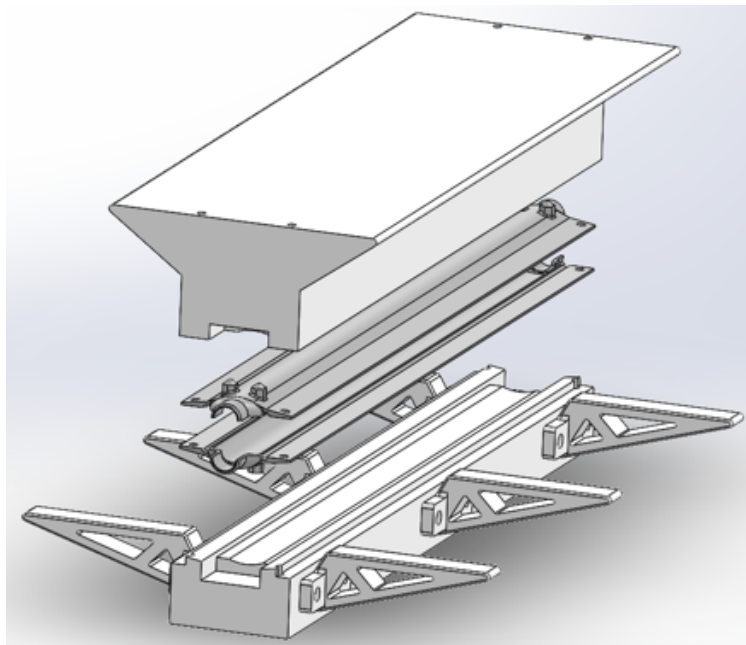


Figure 2.11: Exploded view of clamping tube bracket press jig

A list of the steps taken to create the realistic radiator panel are below:

(1) Manufacture or acquire all parts: two halves of the machined clamping tube bracket, the waterjet cut carbon fiber frames, the sheets of PGS with adhesive cut to length, indium foil strips cut to size, the two main parts of the press jig, blocks to hold the layers at the correct height, pins for alignment, a heavy weight or press, and epoxy

(2) Stack the tapered PGS layers on top of each other for both sides, ensuring the profiles line up and are not at an angle. Try to minimize wrinkles

(3) Set up bottom portion of the press jig

(4) Lay bottom half of clamping tube bracket onto press jig

(5) Insert alignment pins

(6) Lay PGS Layers on height blocks, and set close beside the bottom half of the bracket on either side

(7) Place lower strips of indium foil on the extended arms of the bracket

(8) Mix epoxy and spread a bead along the two edges and depressions of both bracket halves, ensuring no gaps that could allow fluid to escape. Avoid getting the alignment pins stuck because disassembly is important

(9) Rest the PGS layer assemblies on top of the indium foil, only going as far as the flat surface allows (further would go into the epoxy)

(10) Place the top strips of indium foil on top of the PGS layer assemblies

(11) Place the top clamping tube bracket half on top of the lower half, sandwiching the layers, using the four alignment rods.

(12) Apply force to the top of the press jig using a weight or press, and keep this pressure applied until the epoxy is cured

(13) Use fasteners to temporarily attach frames to the now-in-one-piece bracket

(14) Epoxy the edges of the frames together, and allow to cure

(15) Remove fasteners, and add epoxy into alignment holes, allowing it to cure one final time

Pictures of the assembly process are included below.



Figure 2.12: Image of a 16 kg weight on top of the press jig used to attach layers to the bracket

Figure 2.13: Image of the press jig clamping two shells of the clamping tube bracket around PGS layers

## 2.5    Deployment System Design

The deployment system is comprised of multiple sections, performing different functions. The release mechanism allows the stack of panels to be freed from the structure using a burn wire. The kinked tubes are the hinges which the panels use to deploy, and the fluid system pressurizes these tubes for the extension to occur. These sections are detailed individually below, talking about the design and or design process. An image of the packaged configuration is included here as well, which is the start of the deployment



Figure 2.14: Packaged view of the proposed deployable radiator system held down via scroll sheet

This radiator system can also be viewed as a 3D-PDF object in Appendix A below.

### 2.5.1    Stacked Panel Z-Folded Extension

The panels utilize the aforementioned thin-walled tubes as a means to connect to each other. Here, a z-folded pattern with two sets was decided on. Other patterns were initially considered;

radial fanning, unfolding flat pattern to a cube, and origami-inspired flat patterns. A simple zigzag folded architecture was selected for just that: repeatability, and a compact predictable folded pattern with flight heritage on satellite designs [33]. An architecture like this can be scaled easily, and more panels can be added to each stack. The rationale for having two sets of panels comes from the need for a returning fluid line. With a pumped loop system, the fluid that goes through the radiators has to return to the spacecraft somehow, and that means directly back from a linear structure of the first stack.

The number of panels was chosen by iterating them in the thermal resistance network analysis code, ensuring heat rejection above but around 1000 W, and low enough numbers such that a design could fit within tank sizes around a liter. As a first-order design, this could certainly be changed to optimize based on the parasitic mass of the rest of the system — valves, sensors, brackets, tubes, cold plate, etc — which does not change when scaling up the design. Certain limitations will be hit, such as selecting a pump that is powerful enough to overcome the additional pipe friction by adding more radiators, yet light, small, efficient, and reliable enough for the task. Furthermore, adding radiators in series can drop the temperature lower, and this will limit the low-power use case, affecting the operating range of a design.

### 2.5.2    Release Mechanism

The release mechanism was designed in collaboration with Kayla Ployhar, a mechanical engineering undergraduate working on the project. The release mechanism performs two functions. The first is the motion to release the stacked panels, allowing them to be free of any forces or objects preventing deployment. The second function is to actuate a component on command from the spacecraft, enabling the release mechanism to perform its task. Different combinations of these two functions were sketched out and composed, with stabilizing arms, panel holders, ropes, membrane, actuated by any means such as electric motor, explosive bolts, wire cutters, and burn wires. Various components from industry were considered, and a weighted decision matrix was used to evaluate the best concepts. They were scored based on mass, deployment load, and static

survival load, with power requirements not included because high-powered spacecraft would likely have enough ability to run a single-use actuator. The matrix is included below.

| Candidate Design Decision Matrix Rating: 1(worst) - 5(best) | | | | | | | | | | | | | |
|---|---|---|---|---|---|---|---|---|---|---|---|---|
| Critera | Notes | Formula | TINI: Frangibolt | | TINI: Pin Pullers | | TINI: Micro Latch | | Arquimea: Pin pullers | | Nichrome Burn Wire | |
| | | | value | score | value | score | value | score | value | score | value | score |
| Static Launch Loads (N) | needed F = 200 N | [val/400]*5; if > 400, 5 | 3,781 | 5.00 | 448 | 5.00 | 445 | 5.00 | 25 | 0.31 | 338 | 4.22 |
| Max. Deployment Load (N) | needed F = 200 N | [val/400]*5; if > 400, 5 | 3,781 | 5.00 | 45 | 0.56 | 224 | 2.80 | 25 | 0.31 | 338 | 4.22 |
| Lightweight (g) | - | [lowest value/value]*5 | 25 | 0.57 | 30 | 0.48 | 15 | 0.95 | 45 | 0.32 | 2.85 | 5.00 |
| Peak Power | | | | | | | | | | | | |
| FINAL SCORE: | | | 10.57 | | 6.03 | | 8.75 | | 0.94 | | 13.44 | |

Figure 2.15: Decision Matrix used for scoring deployment actuator concepts. Here, mass and load bearing capability were used to compare designs

As well, the original concepts are sketched and shown in Appendix C. Here, the selected design's sketch is included here for reference, but not all aspects are current, such as the existence of a latch mechanism.
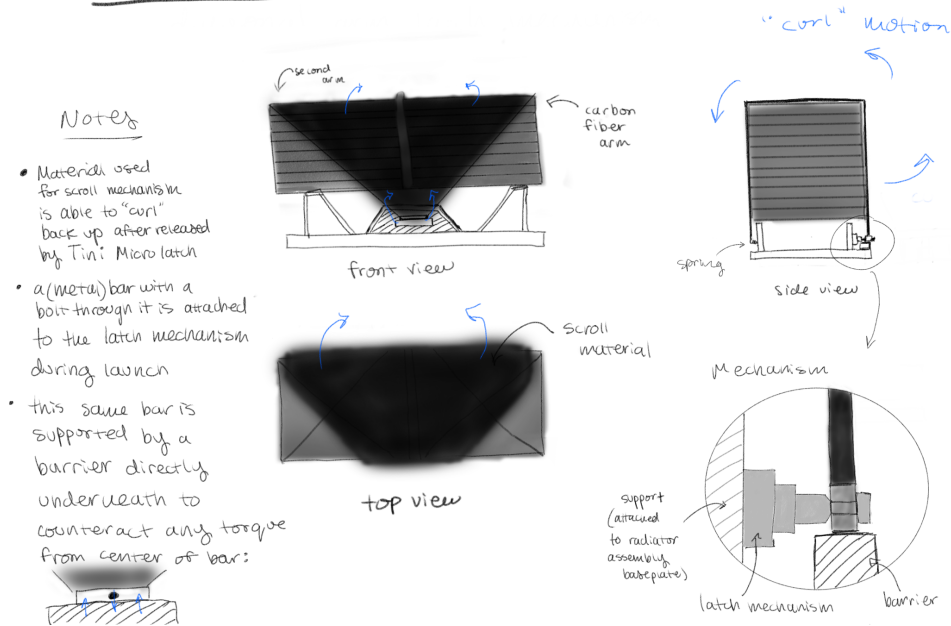
Figure 2.16: Initial image of scroll release mechanism

At first, the double-compression-arms design was the winner, but after further thought, the scroll sheet concept was formed, and was clearly better in every respect, and thus added into the comparison. This new design provides direct compression based on spring tension across the entire top panel, is lighter weight, does not require a complex pin-pulling spring retracting mechanism. It also clears the panels entirely and leaves almost no chance of interference in the deployment as the sheet tucks away safely, and can even be pushed out of the way by the panels if necessary. The design scored better and was chosen as the design to move forward with.

The design chosen is deemed as the "scroll sheet" mechanism in this work. This mechanism consists of an aluminized Mylar sheet held in tension over the stack of radiator panels. The sheet has been permanently deformed so that its stress-free configuration is a roll of a very small radius of curvature. It is interfaced with a thin aluminum attachment containing a singular through-hole for a cord to pass through. The sheet is also attached on the other side to two springs that are fixed to a bracket on the base of the radiator system. Tension is applied to the sheet during assembly, with

the load calculated based on the force required to keep the radiator panel supports within their angled sockets during launch. The expected launch loads of a Falcon 9 rocket were used in this analysis, considering acceleration and vibration g-loads in the lateral and longitudinal directions acting on a spacecraft, and these are in Appendix D. Below, Figure 2.17 shows the launch position, rolling action, and fully-rolled-up configuration of the scroll sheet. In a later section, 4.4.5, there are videos linked to a deployment prototype showing this exact process.
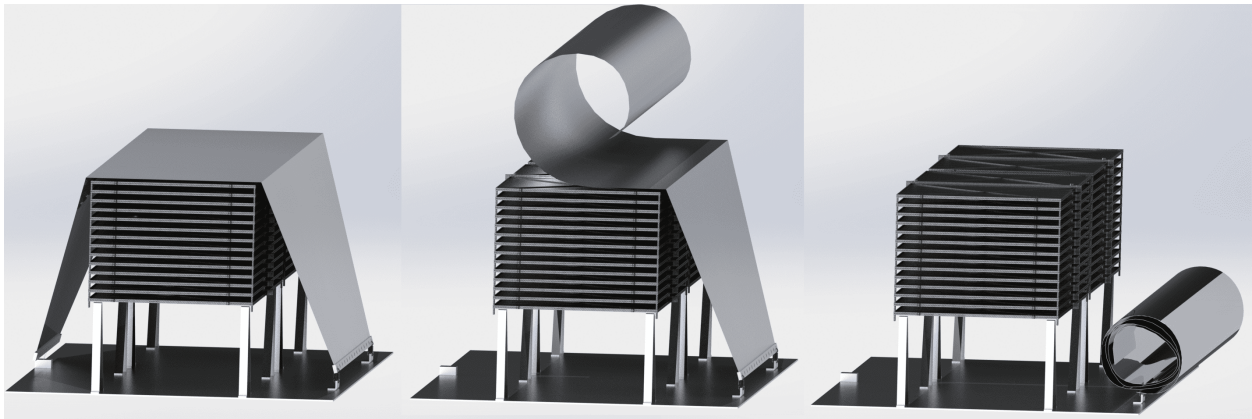


Figure 2.17: Stages of the release mechanism

Given the curvature of this scroll, pulling the sheet straight will result in elastic deformation, and once released, it will spring back into its curled position: a 40 mm diameter cylindrical curl. At the end of the actuation, this roll will be stowed out of the way beside the panels.

This release mechanism matches well with the burn-wire technology explained in the next section.

### 2.5.3    Burn Wire Design

A Vectran burn wire was selected for its simplicity and light mass as a means to release this scroll design. The burn wire concept was brought forward after a search found commercial actuators used on other spacecraft designs. It was quickly implemented because it was superior with lower mass and complexity compared to larger off-the-shelf actuators. Interestingly, this technology was created recently by Adam Thurn in 2012, with his conference paper and patent

on this technology [48]. He makes use of a spring to slowly push the burn wire through a rope in a controlled manner, ensuring enough tension within the rope for proper usage. However, many derivative works exists that uses or builds upon this, such as Roccor's [49], JPL's design [50], and Oh's work in 2014 [51].

Below is a diagram of my radiator design's burn wire system. It is modeled closely after JPL's "mini rope furnace", which uses wrapped coils of nichrome wire and, what appears to be, an insulative material to heat up the rope it surrounds.
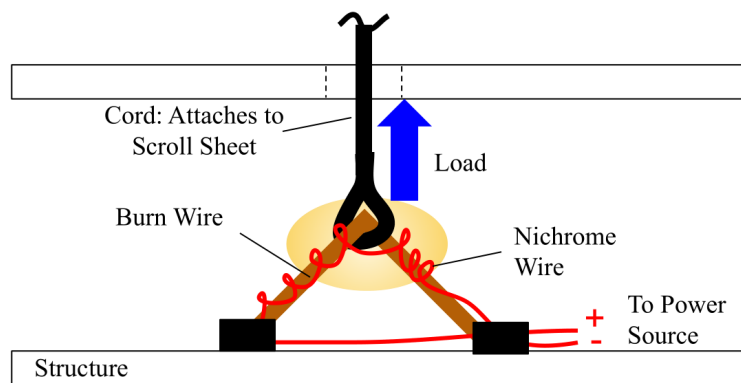


Figure 2.18: Burn wire diagram incorporating spiral-wound nichrome wire along a Vectran cord

Either copying JPL's design directly or using this other design would work to cut the rope for negligible mass.

### 2.5.4    Kinked Tube Hinge Mechanism

One of the unique pillars of this design are the kinked tubes that connect the radiator panels. These connectors serve three purposes, and this synergy is key to reducing the mass of the design. First, these polyimide tubes carry fluid for heat transfer to the radiators. Second, they act as hinges to deploy the panels, utilizing elastic deformation instead of complex mechanical elements. Finally, they become structural members once they fully deploy into pressurized cylinders.

Above, these tubes were visualized opening up the radiator panels in Figure 2.1. However, instead of a single kink, the design should instead utilize a double kink approach visualized below.

Figure 2.19: Close up view of thin kinked polyimide tubes connecting panels together in a prototype
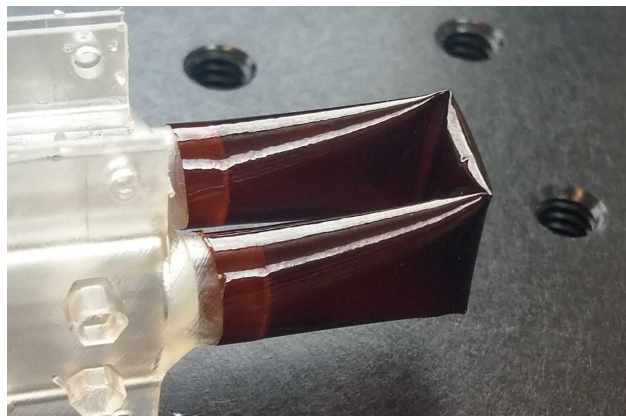


Figure 2.20: Double 90 degree bend of a polyimide tube that is proposed to connect radiator panels

In the proposed design, these tubes are 7.70 mm outer diameter, and 0.069 thickness. This was based on the tubes that were tested in section 4.1.4 below. The experiments conducted showed that these tubes were able to be bent repeatably at least 9 times (the number of pressure runs in the experiment per sample) without leaks. With an increased thickness and same diameter, these samples were unable to complete the experiment's nine pressures without leaking slightly.

Ultimately the size of these tubes was not fully optimized, and this is one area where further improvements could be made. The initial selection of tube size was roughly based on pump tubing

size from the MSL mission, roughly 10 mm outer diameter tubing [22], and then the closest available size was sourced. For optimization purposes, changing the diameter of these tubes will affect the pump's pressure drop, heat transfer, fluid mass, and possibly the radiator stack dimensions.

### 2.5.5    Fluid System

The pumped-fluid-loop system was designed to reject over 1 kW of heat from the spacecraft while minimizing the number of components necessary beyond necessary redundancy. By studying the designs of previous missions such as MSL [22] and Parker Solar Probe [21], a process and instrumentation diagram was formulated and iterated upon, seen in Figure 2.21 below.
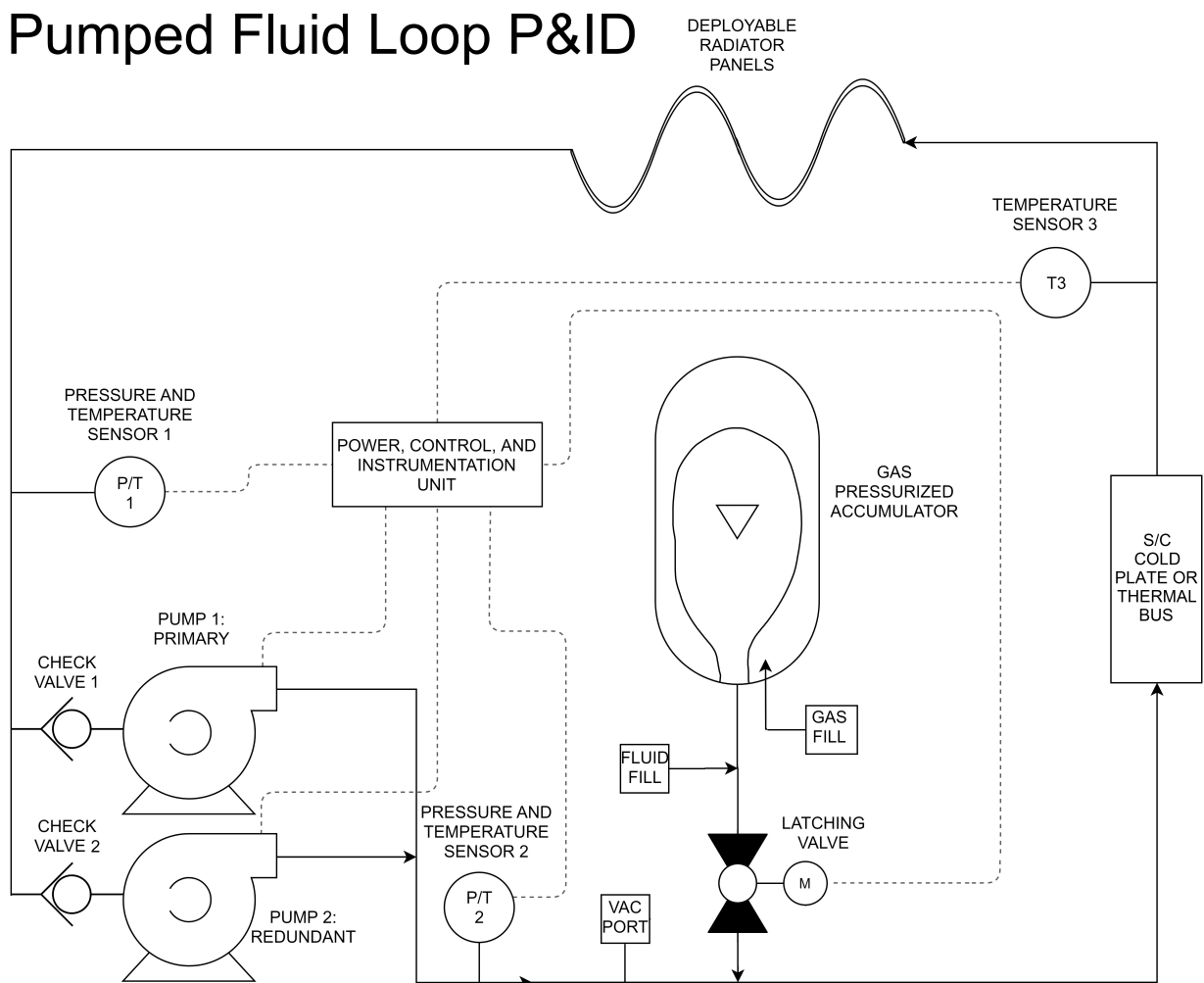


Figure 2.21: Mechnically pumped fluid loop process and instrumentation diagram

### 2.5.5.1    Design Decisions

The pumps [52] and tube diameters were selected to match the performance of those used on MSL at 0.75 L/min. A dual-pump configuration was chosen to match the MSL and Parker Solar Probe missions. A dual pump system is a common choice to ensure that if one fails, the other can continue operations. The rest of the design, however, is a single point of failure. Given the lightweight nature of this solution, additional separate radiator assemblies could be added for redundancy at the cost of several additional kilograms. For the control of the fluid flow, the motors within the pumps are projected to be electrically controlled, such as by varying the input voltage to the motor. This decision diverges from other designs which use additional valves to redirect flow elsewhere, with our goal to increase performance and reliability by removing unnecessary valves that could be a potential source of failure. Such a system will need to be thoroughly tested to ensure this will work over the expected lifetime of the spacecraft.

The latching valve needs to be positioned just inside the primary loop for a few reasons. First, a short distance from the accumulator results in better insulation from the cold external environment before startup. Second, this position does not incur pressure losses since it is not in the path of the loop. Third, a failure partway through the mission would not stop the flow of the fluid. Lastly, allowing the accumulator to be connected with the fluid system during operation could enable the device to dampen any pressure fluctuations in the system.

The position of the vacuum port was selected to be able to pull fluid from the system for testing and pre-launch setup. In the position shown, it can withdraw fluid from the accumulator, from the pumps, and consequently both sides of the radiator panel assembly. The locations for the pressure sensors were chosen to be able to measure the drop across the pumps, and therefore the rest of the fluid system. These locations both include temperature sensors because knowing the temperature of the fluid flowing into the spacecraft is useful to predict and control the heat rejection and provides single redundancy for a sensor failure. An additional temperature sensor was placed right before the radiator panels because the temperature of the fluid after receiving

heat from the spacecraft is important to be able to predict and control the heat transfer of the system as well. However, even if the temperature sensors in this design were to fail, other on-board spacecraft sensors could also be used as means to control the flow of heat.

### 2.5.5.2 CAD Model of the Fluid System

A model has been designed based on the above diagram which is similar to a prototype of the fluid-deployment system that is in development. The piping system, tank, and connections to the radiator panels are shown in Figure 2.22.
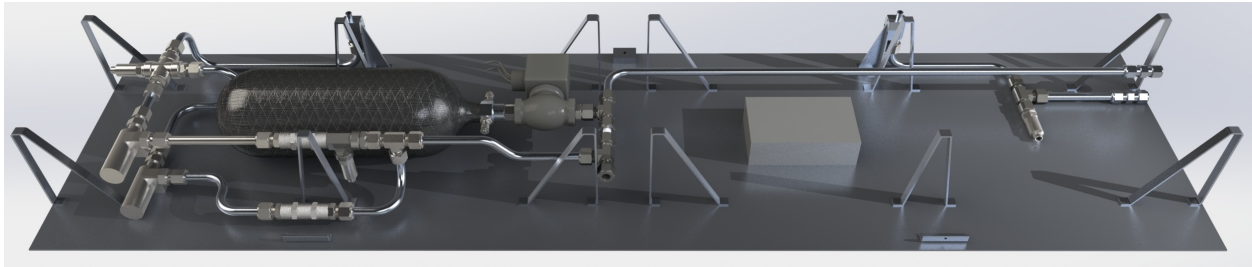


Figure 2.22: Fluid system 3D model shown with panels removed

### 2.5.5.3 Accumulator Design

In the proposed design, a non-traditional approach was taken in order to reduce as much mass as possible. Accumulator designs typically weigh many kilograms and often, bellows designs for spacecraft are used [24, 21] which incorporate ribbed metal to extend and compress. Our approach was to use composite materials to increase the strength to weight performance to save mass, such as the trend in composite overwrapped pressure vessels (COPVs), commonly used in paintball tanks, or here developed into actual accumulators like Steelhead Composites Accumulator, seen in Figure 2.23 below. Further, we were able to prototype this accumulator design, seen in section 4.4.3 below, and were able to demonstrate the functionality with this similar bladder approach in component testing.
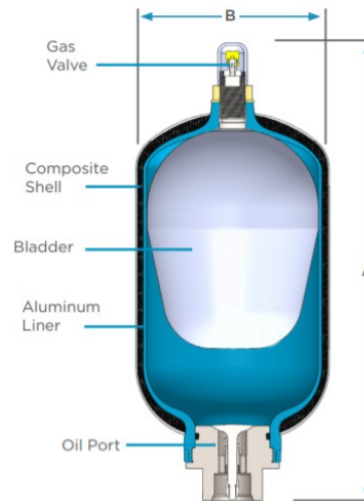
Figure 2.23: Steelhead composite overwrapped pressure vessel accumulator design

In the mass budget in section 3.2.3 below, we use the mass from our design scaled up from a 77 CI tank to the 90 CI tank used for fluid volume sizing calculations. While the prototype system only had one port, and this Steelhead example one has two — one for either end — an optimal design would use aluminum for lightweight fittings, and the pressure vessel would not need to be sized for such as large an operating pressure, reducing the mass further. These fluid volume calculations can be found in Appendix E, and they show that the air pressure for filling the system would only need 20 bar of air pressure instead of the over 200 bar operating pressure this vessel was designed for. Further, the Steelhead design weighs 5 kg for a 4 L of volume, and the proposed design is around 1.5 L in tank volume. Accordingly, it makes sense that it would be possible to scale down this example for a lightweight tank. Overall, through size reduction and smart material choice, we are confident that a design similar to Steelhead can be made to match the proposed design of around 1 kg.

### 2.5.5.4 Heat Rejection Through Motor Control

As mentioned, the design diverges from traditional MPFLs because it lacks what is typically used: a bypass valve that allows fluid to divert away from radiator designs. As mentioned by Benthem in 2009 [24] in a similar MFPL technology, three-way bypass valves keep hydraulic

characteristics constant, and reduce pump speed variation and on/off cycles. This may be one way to control the fluid flow, and it may reduce electrical circuitry, however, the addition of an entire valve increases mass, complexity, and circuitry all on its own. It appears from researching their work that a significant part of getting MFPLs accepted in the market is the long-duration qualification of the components, as they write in their recommendations. Flight qualification needs to happen in any case, and here, this work seeks to propose the best solution regardless of what is described as a "hesitant" market. Concerns of mechanical wear do not appear credible to these authors of this work, as they have demonstrated that using commercial off-the-shelf motor electronics with their BBM pump showed operation for already 5 years without problems or mechanical degradation [24]. Additionally, recall that there are two pumps in single redundancy, so even if one were to break, there should be another backup ready to go.

With the mechanical issues resolved, the remaining difference between the designs is single speed vs variable speed DC motors. Here, brushless sensorless DC motors are said to be used for their MPFL. With this type of sensorless BLDC motor, a dedicated microcontroller is required with this type of motor anyways [53], so it does not seem like a significant stretch to allow the controller to vary the voltage and speed of the pump. With any BLDC motor, it is possible to get torque ripples and current spikes which can damage the controller or motor windings [54], and they need to be designed for the expected operating conditions. However, this is an active research area with work describing ways to reduce these issues. Furthermore, this technology is commonly used in electric tools, bikes, and quadcopters, so there is no shortage of expertise in similar variably-controlled designs. To summarize, Benthem is able to have a controlled BLDC motor that performs without failure over many years, and adding additional control capability does not appear to be a significant issue. By eliminating the need for a bypass valve, less circuity, mass, and risk is inherited in the design. With an already single-fault-tolerant system, it makes sense to reduce the additional failure mode that a bypass valve induces by replacing the fluid control mechanism by pump speed variation.

## 2.6 Thermal Analysis of the Multi-Panel Pumped-Fluid-Loop Radiator System

A thermal analysis using Matlab was performed to solve the system performance of a spacecraft operating with a single-phase pumped-fluid-loop system, using these novel radiator panels as they were intended. Details of the pumped-fluid-loop system, including 3D models and the process diagram, are included in the sections above. A simplified thermal diagram of the system is shown in Figure 2.24 below for reference.
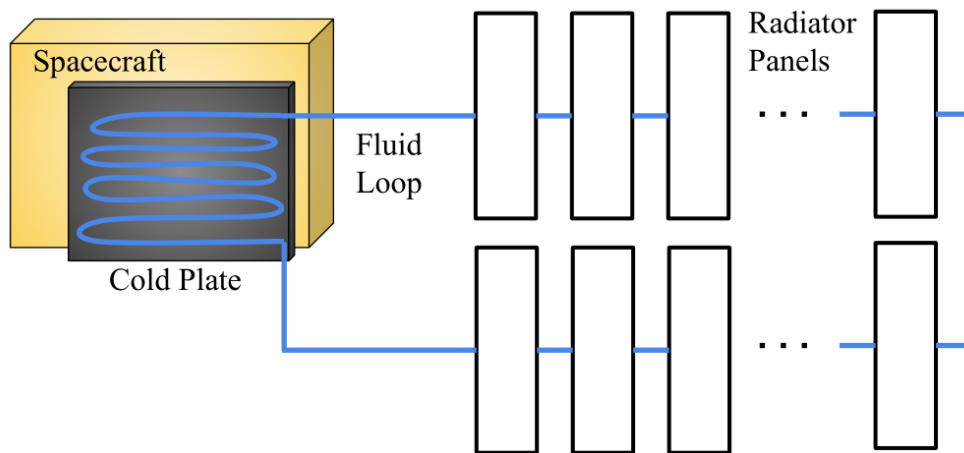


Figure 2.24: High-level thermal diagram for the pumped-fluid-loop system

Using the first law of thermodynamics in conjunction with fluid transport, a network of temperature nodes were placed and then solved to find the maximal heat load produced by a spacecraft that remained within temperature limits.

This network of thermal resistances, in the same way as electrical resistance, shows the path of flow of a conserved quantity, in this case, heat instead of charge. By laying out the nodes of the network such that it matches the physical system, putting numbers to the thermal resistances and solving for the system temperature allows a designer to understand where the most critical regions are for heat rejection early on in the design process.

When the design was in the early stages, it was not well understood how long the cold plate should be to prevent a significant drop in temperature that would reduce the performance. By

running multiple scenarios with different geometry, a realistic baseline design was found. The same was able to happen with iterating the number of panels and finding area required to reject over 1000 W. The geometry of the clamping tube bracket was able to be iterated such that there would not be an extreme temperature drop, and this informed the rough dimensions of the design before the concept was finalized. Critically, this work was also able to get realistic base temperatures of the radiator panels, which was used in further analysis to optimize the panel geometry. Fundamentally, this type of analysis can be used both as a preliminary tool to size components, as well as a rigorous analysis that determines the expected performance of the finalized design.

### 2.6.1    Assumptions and Parameters

(1) Steady state operation

(2) Max operating temperature for a spacecraft is 50 °C matching Verdonck [39]

(3) Heat from the external environment is negligible, no irradiation or albedo, solely facing deep space

(4) Dual-sided radiator panels

(5) Same flow rate and pumps as Mars Science Laboratory rover at 0.75 L/min [22], with similar diameter tubing

(6) Laminar partially developed flow through the panels

(7) Viscosity, heat capacity, and other fluid parameters are considered constant and averaged around the expected temperature of the fluid - 52 % by volume ethylene glycol in water

(8) Radiator layers do not touch or interact after the clamping region - this is conservative, and would otherwise slightly increase heat transfer.

(9) Temperature of the fluid within each clamping tube bracket is all at the same temperature, and only drops after passing through each panel in its entirety.

An exhaustive list of parameters from the analysis takes up a significant amount of space since it is a large thermal network. A table with some of the key influencing parameters are included in Appendix F, and the code (with all the values) for the entire analysis is linked in the data archive Appendix B.

The fundamentals of heat transfer can be found in any undergraduate level heat transfer textbook, but the equations I am using are summarized below.

**Conduction: Rectilinear**

$$\dot{q}_{cond-x} = kA\frac{\Delta T}{L} \tag{2.3}$$

**Conduction: Cylindrical**

$$\dot{q}_{cond-r} = 2\pi Lk\frac{\Delta T}{ln(r_2/r_1)} \tag{2.4}$$

**Conduction: Elliptical, Balcerzak 1961 [55]**

$$\dot{q}_{cond-el} = \frac{2\pi Lk\Delta T}{ln((c+d)/(a+b))} \tag{2.5}$$

**Convection**

$$\dot{q}_{conv} = hA\Delta T \tag{2.6}$$

**Convective Heat Transfer Coefficient**

$$h = \frac{Nu \cdot k}{D} \tag{2.7}$$

**Radiation**

$$\dot{q}_{rad} = \varepsilon\sigma AT_{surf}^4 \tag{2.8}$$

**Fluid Flow**

$$\dot{q}_{flow} = \rho\dot{V}C_p\Delta T \tag{2.9}$$

**Reynolds Number**

$$Re = \frac{uD}{\nu} \tag{2.10}$$

**Prandtls Number**

$$Pr = \frac{Cp \cdot \mu}{k} \tag{2.11}$$

**Graetz Number**

$$Gz = \frac{D}{L} Re \cdot Pr \tag{2.12}$$

**Nusselt Number: Laminar Partially Developed Flow, Bergman 2011 [14]**

$$Nu = \frac{\frac{3.66}{\tanh\left[2.264Gz^{-1/3}+1.7Gz^{-2/3}\right]} + 0.0499Gz\tanh\left(Gz^{-1}\right)}{\tanh\left(2.432Pr^{1/6}Gz^{-1/6}\right)} \tag{2.13}$$

**Hydraulic Diameter: Replaces diameter where required**

$$D_h = 4A_{cs}/Perim \tag{2.14}$$

Here, k is thermal conductivity, L is the tube length or distance in the case of rectilinear conduction, A is area, either cross-sectional, radiating surface, or wall contact area for the fluid. T is the temperature, $\dot{q}$ is the heat flow, $\dot{V}$ is the volumetric flow rate, $\nu$ is the kinematic viscosity, $\mu$ is the dynamic viscosity, Cp is the specific heat of the fluid, h is the heat transfer coefficient, D is hydraulic diameter, $\sigma$ is the Stefan–Boltzmann constant, $\varepsilon$ is the emissivity, Re is the Reynolds number, Gz is the Graetz number, and Nu is the Nusselt number which relies on correlations for the regime of fluid flow, here being laminar and partially developed. a,b,c, and d are dimensions for an elliptical cross section from Balcerzak's work [55].

### 2.6.2 Cold Plate Thermal Resistance Network Detailed

After building a thermal circuit, these equations were used along with the first law of thermodynamics to ensure energy was conserved, and a list of equations was able to be written from the conservation of energy at every temperature node. For simplicity, the equations were reduced using equivalent resistances, R, in the form $\dot{q} = \Delta T/R$ for all except the radiative term, which was given its own constant. A representative diagram of the initial heating section is included in Figure 2.25 below.
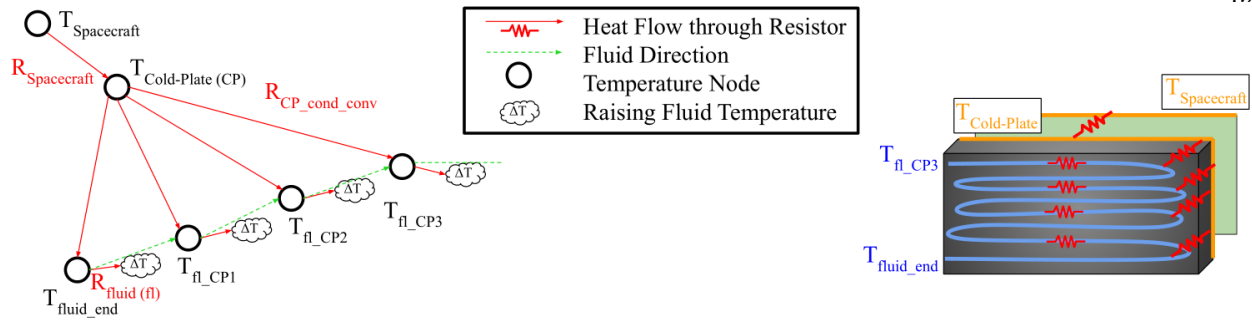
Figure 2.25: Thermal resistance network from a spacecraft to its fluid loop via a cold plate. Left: network tree graph. Right: representation of the network on a realistic model

These equivalent resistances made it easy to understand where the most significant bottlenecks in the system were located. Essentially, where the equivalent resistance or temperature drop was the highest, this was the section that is the "weakest link" preventing additional radiative heat transfer from occurring. As the system was solved, these resistances were analyzed and parameters were modified until they were as negligible as reasonably possible. This was one of the first steps taken in the design to understand basic dimensions of the system; this analysis helped to set realistic limits for the design early on.

A similar resistance network was created for the heat flowing through the radiator panels with temperature nodes within the fluid, bracket, the clamping region of the layers, and at the exposed-surface midpoints of the layers. The heat conduction pathways through the bracket and stack of layers assumed the expected average distance and included the necessary travel of the heat through the insulating adhesive layers. Here, the indium foil contact resistance was assumed negligible compared to the insulation between the PGS layers. Each radiator panel is assumed to use the temperature of the fluid entering the clamping tube bracket. The heat flow through these fluid nodes depends solely on the temperature of the previous fluid node, and any heat that enters or leaves the prior node. A temperature-node tree graph shows the heat pathways for the rest of the network in the next section.

### 2.6.3 Results

The code iteratively solves for the temperatures across the system for an arbitrary number of nodes (and therefore equations), ensuring that every equation is met - conserving heat flow. From there, the heat through every section can be backed out and computed. As a final check, We have verified that the sum of all the radiative heat adds to the specified input heat.

A depiction of the results is seen in Figure 2.26 below as a tree graph showing the spacecraft, fluid path, radiator layers, and all the other temperature nodes in between through which heat travels.
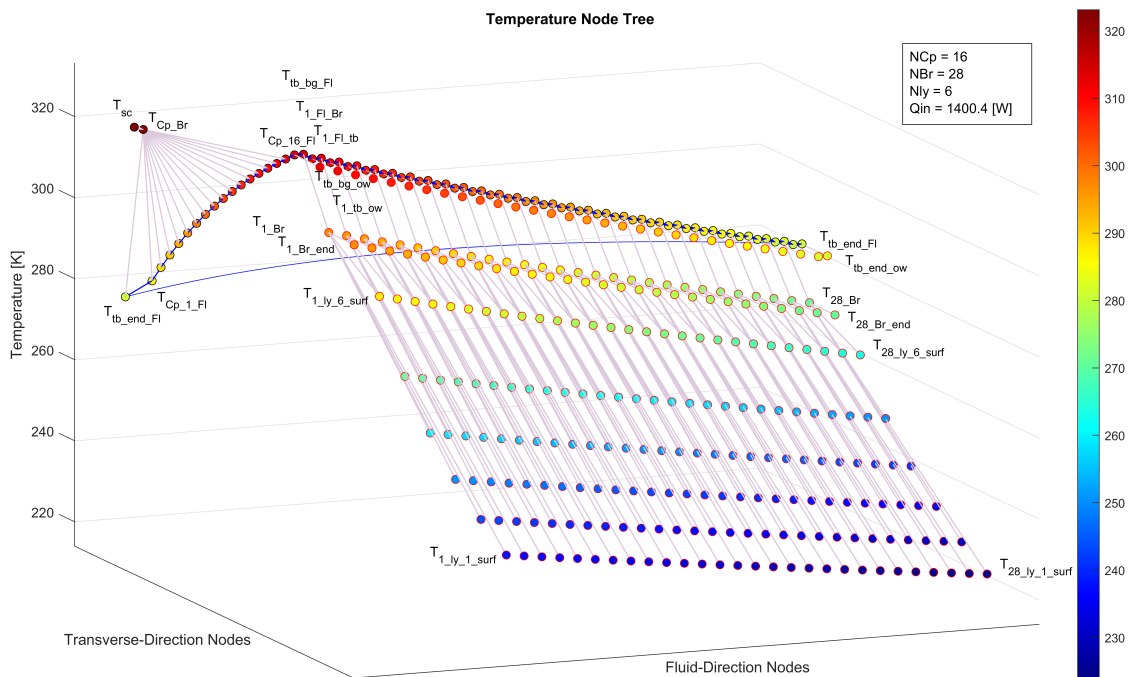


Figure 2.26: Temperature-node tree graph of pumped-fluid-loop radiator system, showing the solution to its thermal resistance network

At the upper limit of the selected 50 °C for the spacecraft, the system rejects 1400.4 W of heat. At the lower limit of freezing the fluid (-40 °C), the system must reject a minimum 791.7 W of heat with the flow rate slowed by 33 %. With this cold case, the spacecraft temperature becomes -7.0 °C; alternatively, 847.1 W is the minimum heat to keep the spacecraft above 0 °C. These numbers are provided as guidance for typical temperature limits, but in reality, each spacecraft

could have unique requirements depending on the mission.

Here, the radiating surface area for these 28 panels is 6.90 m$^2$ which includes both sides of the panels and brackets without considering the structural supports.

This analysis uses a simplistic resistance model to calculate heat transfer on the radiator panels. For further improvement, a lookup table would be ideal using the previously derived isothermal model, otherwise, implementation of a numerical solver within a nonlinear solver (loop within a loop) would slow down the solution.

For panels at almost the same 300 K temperature, the system shows very similar performance to the triangular mathematical model derived in section 2.3.3 above: an averaged 50.0 W per panel, compared to the 60.5 W calculated above. This lower result makes sense because the panels increment away from the spacecraft, they drop in temperature as the fluid transfers heat away before reaching them. This drop in temperature then reduces the radiation that gets rejected from these further panels.

### 2.6.4    Parameter Sensitivity Analysis

A preliminary sensitivity analysis was conducted to investigate the effect of changing some of the key parameters in the thermal resistance network. Heat rejection was found by iterating the code until the spacecraft temperature limit of 50 °C was met.

Fluid flow rate, fluid specific heat, tube radius, layer thickness, layer thermal conductivity, layer length, and the number of panels were all independently varied from their base parameters, seen in Appendix F. Note that in the code, the number of panels needed to be rounded to the nearest whole number. See Figure 2.27 below.
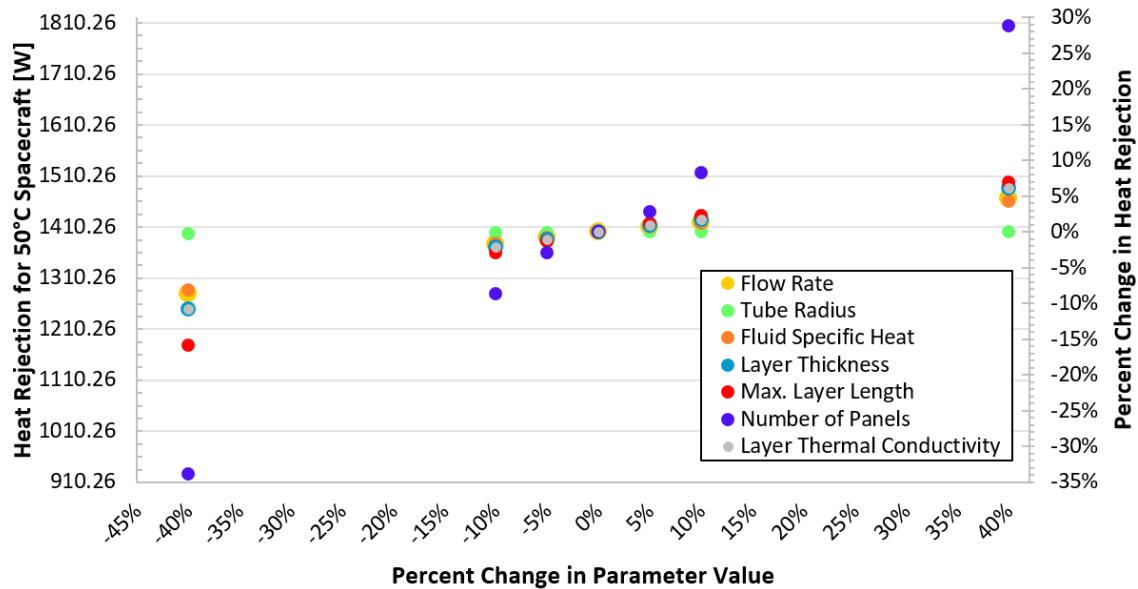
Figure 2.27: Sensitivity Analysis exploring the change in heat rejection for the thermal resistance network by modifying independent parameters. Heat rejection is solved to meet the maximum spacecraft temperature limit of 50 °C

The number of radiator panels was found to be the most critical parameter of the ones explored. Layer length is the next most sensitive, and this parameter has a notable asymmetry about the positive and negative sides of the x-axis. Layer thermal conductivity and layer thickness show an almost identical change in heat rejection. Many of these other parameters only increase heat rejection by a small fraction of the initial change, however, stacking these optimizations could enable larger gains.

Overall, this analysis further demonstrates that more work can be done to optimize the design. Changes to these parameters should also be accompanied by modifications to the mass estimate of the system since this is the cost of scaling.

# Chapter 3

# Performance and Comparisons to Similar Technology

## 3.1 Mass, Power, and Volume

### 3.1.1 Mass Budget

A mass budget has been created which breaks down the mass for the exact parts proposed for the design. A 15 % mass growth allowance has been included to allow for increased mass with future changes in accordance with AIAA standards [56]. Here, it is assumed that the technology being presented is between E2 "layout" and C3 "Preliminary Design" maturity categories.

Table 3.1:  Estimated Mass Budget

| Part | Qty/Length | Combined Mass [kg] | Source |
|---|---|---|---|
| Carbon Fiber Frames | 28 | 0.696 | Design |
| PGS Layers with Adhesive | 28 | 1.458 | Design w/ ProGraphite sheets |
| Clamping tube brackets | 28 | 1.015 | Design |
| Polyimide Tube | 2.4 m | 0.006 | Design |
| Aluminized Mylar® scroll | 1 | 0.132 | Design |
| Scroll Spring | 1 | 0.002 | Design |
| Scroll Attachments | 1 | 0.131 | Design |
| Vectran® Cord and Burn Wire | 30 cm | 0.002 | Sampson Rope |
| Tank | 1 | 0.988 | Design |
| Tank Fitting | 1 | 0.036 | Design |
| Tank Bladder | 1 | 0.075 | Estimated |
| Water-Glycol Fluid | 1.33 L | 1.439 | Estimated |
| Latching Valve | 1 | 0.725 | Vacco |
| Pumps | 2 | 0.500 | Pacific Design Tech. (MSL) |
| Temperature and Pressure Sensors | 3 | 0.426 | GP50 Transducers |
| Driver Boards + Enclosure | 2 | 0.100 | Estimated |
| Check Valves | 2 | 0.390 | Circo Aerospace |
| Fill/Drain Ports | 3 | 0.825 | Vacco Low P. Fill Drain Valves |
| Tees, unions, elbows | 10 | 0.998 | Dynatube |
| Tubing 9.53 mm OD, SS | 3 m | 0.577 | Estimated |
| Cold Plate - Not incl., applic. specific | | | |
| Supporting Brackets - Aluminum | 12 | 0.175 | Design |
| Structural Attachment Baseplate | 1 | 0.650 | Estimated |
| Fasteners 50x M4-16 mm | 50 | 0.113 | Estimated |
| Copper Wiring AWG 18 | 8 m | 0.083 | Estimated |
| Subtotal | | 11.4 | |
| 15 percent Margin | | 1.7 | AIAA standard S-120A-2015 |
| **Total Mass with Margin** | | **13.3** | |

### 3.1.2    Power Budget

The burn wire, latch valve, pumps, and pressure and temperature sensors are the only powered components for this design. All but the burn wire and latch valve will need to be operating at the same time.

The burn wire actuation could likely require about 20 volts DC and 1 amp of current, so 20 W of power if it is similar to JPL's micro burn wire release mechanism [50].

The Vacco latch valve V1E10453-01 lists 20 V, but not the exact power draw. For a similar vacco valve, the power draw is 90 W [57].

The pumps proposed here follow from the specifications of the one used on the MSL rover, despite being meant for CFC-11 instead of water, and the assumption is that a similar size and flow pump can be procured . For this pump, it draws a maximum of 10 W each, according to Birur, 2015 [52]. Note that only one of the two pumps would operate at the same time.

The pressure and temperature sensor model 7220 [58] from GP50 does not list maximum power draw, however, a similar pressure and temperature transducer from TE, model AST20PT [59] can have a maximum of 0.28 W. Assuming 3 sensors, that would total 0.84 W.

Table 3.2:   Estimated Power Budget

| Part | Max Power Draw [W] | Notes |
|---|---|---|
| Burn Wire | 20 | one time use |
| Latch Valve | 90 | one time use |
| Pumps | 10 | continuous |
| Pressure and Temp. Sensors 3x total | 1 | continuous |
| **Max Operating Power Total** | **11** | |

### 3.1.3    Volume Budget

In the packaged form, the design takes up 0.108 m$^3$, with length width and height being 1.307 x 0.319 x 0.259 m respectively. After being extended, the maximum length becomes 3.822 m instead of the previous 0.259 m. To note, additional space (on the order of several cm) will be required for the rolled-up scroll sheet.

## 3.2      Comparable Radiator Technology

Deployable and pumped-fluid-loop radiator technology need to be compared against the current novel deployable radiator architecture to understand the performance gains. In this section, the spacecraft that come closest to the current design are explored in the subsection below, and their specifications are listed in a table.

One of the most critical metrics for this system is the rejected heat per unit mass, also known as specific power. Radiator heat flux can also be used to compare designs. However, as we will see, radiator source temperature can impact these heat rejection performance metrics significantly, which makes comparisons difficult. Areal densities (kilograms per square meter) are useful to compare against these varied-temperature designs, and have been used as a NASA goal to compare high-temperature nuclear-electric rockets [60]. This metric is included with the other performance metrics in the second table. Additionally, the areal density and heat flux metrics have a second set of values for comparing single-sided versus double-sided designs. Planform radiator area here refers to the area of the panels used for radiation that is projected down onto a plane.

For these comparisons, only spacecraft above 1000 W here are included. This was done because less powerful spacecraft do not need large heat transport solutions, and would unfairly win in the W/kg metric. As well, papers from technology operating before year 2000 are not included. Some designs that fit this category include Goncharov, 2000 [40] and Lashley, 1998 [61]. As well, the space shuttle design is not considered here due to it being an older technology than the ISS, however, it is another example of a deployable radiator with flight heritage [62].

### 3.2.1      Candidates for Comparison

The ISS is the only operational current example of a pumped-fluid-loop system with a deployable radiator design to which I am aware, however, this is an older technology.

The MSL spacecraft, along with its predecessor Mars Pathfinder and successor Mars 2020, uses a static radiator attached to the cruise module. MSL and Mars 2020 contain an radioactive

thermal generator (MMRTG) that produces a couple thousand watts of heat, and this heat is pumped through two fluid loops to reject the heat from the cruise module. Unfortunately, public data does not exist on the mass breakdown of this pumped-fluid-loop system.

The Parker Solar Probe mission has a pumped-fluid-loop system as well, but it is higher temperature and non-deployable. The published mass numbers for the system are hard to compare because they include the solar arrays with the rest of the radiator cooling system; 86 kg for the Solar Array Cooling System [63]. If one uses the mass number of only the radiator panels, it becomes only 20 kg for just the radiators (4x 5kg radiators) [21]. Somewhere in between these two values is the estimate that excludes the mass of the solar arrays while keeping the rest of the fluid loop system.

The most recent and closest comparable deployable radiator design comes from Lécossais' DPR design [5] in 2017, and was updated by Verdonck [39] in 2018, but the information gathered here stems from the 2017 paper due to abundant specifications. They use a loop heat pipe technology with a rigid panel deployed with a single hinge.

Ding, 2017 has a similar loop heat pipe radiator design as Lécossais, with a solid sandwich panel design with a hinge [9].

Siamidis presents a concept for a high-power nuclear fission radiator for the lunar surface in 2006 [44]. Note that the data used for the comparison comes from one of their test cases for a 100 kilowatt-electric fission-power design. This work is followed up with manufacturing validation from their subsequent work with Ellis in 2011 [45], however, the results here do not include mass estimates, so the original work's design is used for comparison instead.

Tomboulian in 2014 presents another nuclear power concept, for a nuclear-electric spacecraft design [47]. Their work references the research of similar high-power nuclear radiator designs such as the fission-surface-power designs seen from Siamidis, Ellis, and Mason, as well as the Jupiter Icy Moon Orbiter design [44, 45, 46, 43]. Tomboulian here provides analysis data for different scenarios, and the one compared was the one selected for reducing mass in their design. However, it should be noted that they use heuristics to calculate pump mass and structure, this was not a bottoms-up

approach like other more detailed designs.

### 3.2.2 Fourth Power Normalization for Equating Different Temperature Spacecraft

There is a significant hurdle comparing "apples to apples" when it comes to different temperature spacecraft.

We know from the fundamentals of radiative heat transfer that heat is proportional to the temperature to a fourth power, as below.

$$\dot{q}_{rad} = \epsilon \sigma A_{surf}(T_{surf}^4 - T_{surround}^4) \tag{3.1}$$

With rejecting to space, here we assume the $T_{surround}^4$ is negligible as the background temperature of space is 2.7 K [64], compared to a room temperature at 293 K. So

$$\dot{q}_{rad} = \epsilon \sigma A_{surf} T_{surf}^4 \tag{3.2}$$

Consequently one could expect that to normalize radiator temperatures, you can normalize by taking the normalization temperature to the power of four, and dividing it by the system's radiator base temperature to the fourth power for a ratio to either inflate or deflate the number.

$$\dot{q}_{norm} = \dot{q}_{surf} \frac{T_{norm}^4}{T_{surf}^4} \tag{3.3}$$

This would be true if the radiator was at a constant temperature, but as we saw in section 2.3.3 the temperature changes with distance from the base or heat source of the radiator.

Below is a graph that uses the triangular layered radiator mathematical model for the proposed radiator geometry, and compares it to this normalization technique.
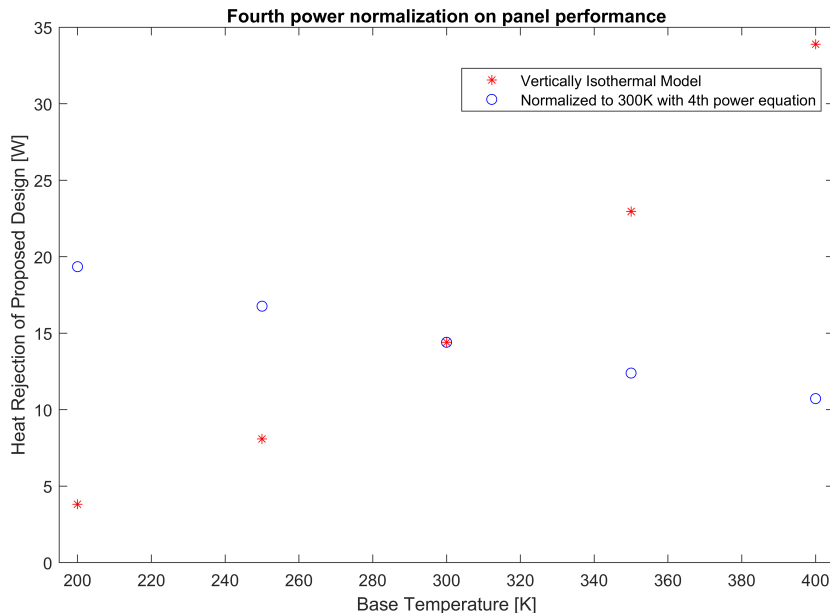
Figure 3.1: Attempt at normalizing radiator base temperatures to compare performance.

If this technique was perfect, one would expect the blue curve to be horizontal and flat. However, we see that this is not the case. In fact, the slope is opposite to the slope of the isothermal model.

While the normalization method we've shown is rooted in heat transfer fundamentals, it is not viable to compare different systems against one another, and the reason it has been included is to provide some idea of how system temperature affects heat rejection. Without comparing many different radiator examples, its difficult to know how to modify this to be accurate across many different radiator profiles. More work should be done in this area to understand the best way to compare radiators to each other.

These results in the upcoming table are normalized to the same reference temperature of 300 K using this fourth power method. This is done because all missions are different operating conditions, and its easier to radiate at higher temperatures, due to the fourth power relationship for radiative heat loss with respect to temperature. For the comparison, the base temperature was chosen to be at the spacecraft, or other hot source such as a base plate. 300 K was used as

this standard comparison temperature, selected for its roughly room temperature conditions most components operate in, and for its even number.

### 3.2.3 Performance Comparisons

Table 3.3 has been compiled below which includes as much data as seemingly publicly available, comparing the spacecraft listed above to one another. Table 3.4 follows up by comparing just the relevant performance metrics.

Table 3.3: Data Comparison of High-Power Radiator Technology

| Spacecraft / System Name | Dual Sided | Deployable | S/C Temp [K] | System Mass [kg] | Radiating Area (both sides) [m²] | Heat Rejected [W] | Heat Rejected Normalized to 300 K [W] | Source Ref. | Notes |
|---|---|---|---|---|---|---|---|---|---|
| International Space Station | yes | yes | 285.6 | 6492 | 951 | 70000 | 85281 | Oren, 1995 | Only includes mass of the radiator ORU units, no additional structure. Max temp. of fluid 12.4 C |
| Mars Science Laboratory | no | no | 273.2 | No data | 5.48 | 2110 | 3070 | Birur, 2013 | Estimated Area of panels, MMRTG heat + electric output for power, cold plate temp. used |
| LHP Radiator - Ding | partially | yes | 305.6 | 30 | no data | 1000 | 929 | Ding, 2017 | Partial panel self occlusion |
| DPR - Lecossais | yes | yes | 368.2 | 50 | 9.24 | 2800 | 1235 | Lecossais, 2017 | Hottest 95 deg C case |
| | ~ | ~ | 338.2 | ~ | ~ | 1700 | 1053 | | Colder 65 deg C case |
| Parker Solar Probe | no | no | 398.2 | 20 | 4 | 5900 | 1902 | Ercol, 2018 | Only incl. mass of radiators and worst-case temp. at the solar panels |
| | ~ | ~ | ~ | 86 | ~ | ~ | ~ | ~ | Includes mass of pump, instruments, and solar arrays |
| Brayton HRS | yes | yes | 512 | 829.1 | 306 | 297000 | 35008 | Siamidis, 2006 | From the 100 kWe sample case |
| Tomboulian HRS Model | yes | N/A | 900 | 224.5 | 79.7 | 700000 | 8642 | Tomboulian, 2014 | Pump and Structure mass was estimated, detailed components not considered |
| PGS Radiator, this work | yes | yes | 323.2 | 13.3 | 6.84 | 1400.4 | 1040 | Marquis, 2021 | |

Table 3.4:   Performance Metrics Comparing High-Power Radiator Technology

| Spacecraft / System Name | S/C Temp. [K] | Heat Rej. per Mass [W/kg] | Heat Flux [W/m$^2$] | Areal Density [kg/m$^2$] | Heat Flux (Planform Area) [W/m$^2$] | Planform Areal Density [kg/m$^2$] | Source Ref. |
|---|---|---|---|---|---|---|---|
| International Space Station | 286 | 11 | 74 | 6.8 | 147 | 13.7 | Oren, 1995 |
| Mars Science Laboratory | 273 | no data | 385 | no data | no data | no data | Birur, 2013 |
| LHP Radiator - Ding | 306 | 33 | no data | no data | no data | no data | Ding, 2017 |
| DPR - Lecossais | 368 | 56 | 303 | 5.4 | 606 | 10.8 | Lecossais, 2017 |
|  | 338 | 34 | 184 | ~ | 368 | ~ | ~ |
| Parker Solar Probe | 398 | 295 | 1475 | 5.0 | 1475 | 5.0 | Ercol, 2018 |
|  | ~ | 69 | ~ | 21.5 | ~ | 21.5 | ~ |
| Brayton HRS | 512 | 358 | 971 | 2.7 | 1941 | 5.4 | Siamidis, 2006 |
| Tomboulian HRS Model | 900 | 3118 | 8787 | 2.8 | 17575 | 5.6 | Tomboulian, 2014 |
| PGS Radiator, this work | 323 | 106 | 205 | 1.9 | 409 | 3.9 | Marquis, 2021 |

The results from these tables is clear when excluding the high-temperature systems: this novel deployable radiator design outperforms all competition in the basis of heat rejected per unit mass. The proposed system achieves **three times the heat rejected per unit mass** compared to Léccosais' DPR and Ding's LHP designs.

Reasons our design is able to achieve higher performance per unit mass:

(1) Mass savings by way of

    (a) simplifying the fluid loop system, reducing parasitic mass from additional fittings and components

    (b) using a lightweight release mechanism with a burn wire and scroll sheet

    (c) utilizing the kinked tubes for structural, dynamic, and thermal functions

    (d) ignoring conventional sandwich panel design, instead using a carbon composite structure to hold the panels rigid.

(2) Heat rejection improvements through

    (a) individual panels optimally shaped

    (b) choosing to use highly conductive PGS on the panels to transfer the heat to the ends of each panel.

Together, these changes inch closer to the theoretically optimal design, reducing mass while increasing heat-rejection performance.

Further, our design is also highly scalable for two reasons. First, it can be stored in a small volume and does not require a large area of the spacecraft external surface, unlike a large rigid panel that needs space to rotate as seen with Lécossais and Verdonck. Secondly, we can always add more panels, stacks, fluid volume, and increase pump size for higher performance with relatively little additional mass. The drawbacks, however, come from the less rigid nature of a z-deployed panel architecture connected with pressurized tubes. These shortcomings, however, are addressed in section 4.2.

Our proposed design outperforms the existing lower-temperature technology in terms of areal density as well as heat flux. The design also beats the high-temperature solutions from Siamidis and Tomboulian in areal density, which is the best metric to compare since drastic temperature differences should not directly affect this result; only the size and layout of the panels affects this. Our design could even improve if it were scaled to reject hundreds of thousands of watts such as these. We already saw that the majority of the mass of the proposed design is not the radiator panels or fluid, but the associated structure and fluid loop fittings, tank, pumps, etc. As has already been discussed, this design should be able to achieve higher performance by scaling the architecture for higher heat loads. A better comparison would be against the panels of each design individually. Data from Siamidis' Brayton HRS sample case shows a single-sided radiator panel areal density of 3.8 kg/m$^2$ [44]. For our design, including the mass of the fluid and panel assembly with 15% margin, it weighs 6.92 kg with a planform radiating area of 3.42 m$^2$, giving a result of 2.0 kg/m$^2$. This result, as well as the heat per mass comparison against similar temperature radiators, suggests that our design methodology can indeed reduce mass compared to other approaches.

# Chapter 4

# Deployment Experiments and Simulations

## 4.1 Thin Tube Bending / Post-Buckling Experiments

As previously discussed in section 2.5.4, the thin tubes used in this radiator design perform many functions in order to save mass. Structurally, they are used to hold the panels together; thermally, they allow fluid to flow to the radiators; and dynamically, they act as a hinge for the deployment to occur. Consequently, it seemed important to characterize how these critical components would perform during the deployment process. Research and experiments were conducted to determine if these tubes would be able to deploy by themselves when pressurized, and survive extreme bending.

### 4.1.1 Results from Literature on Thin Tube Kinking

An early literature review was performed to investigate the current research for the purpose of eventually modeling the behaviour of thin tubes in the kinked state, folded before deploying. This post-buckling review is included in the appendix G below, and was completed as part of a independent study course for credit. The results of this work showed that much of this area has not been widely covered, as research tends to focus on the point of buckling, not afterwards. Stresses and strains have largely been ignored at strong curvature regions sharp corners. Large deflection has mostly been ignored, with no research exploring close to a kinked in half scenario. Ovalization of inflated tubes, however, has been described in detail.

Additional later research found similar work from the domain of inflatable spacesuits, with

arm joints designed to accommodate mobility. Work from Schmidt in 2001 [65] and Guo in 2020 [66] show that there has in fact been work to characterize bending moments in inflatable structures. An image from Schmidt shows their membrane model being considered.
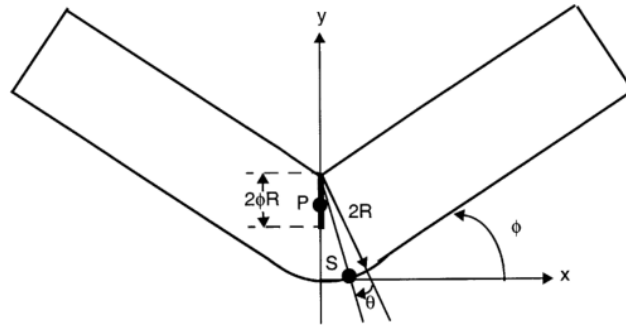


Figure 4.1: Inflated beam kinking schematic for a membrane model [65]

Schmidt details a beam and a membrane model, used in spacesuit design applications, each with their own assumptions. The membrane model assumes inextensability and that all the work goes into compressing the gas inside the tube, shown in Figure 4.1 above. The beam model assumes elasticity, but no compression of the gas. As well the beam model is not valid for large deflections since wrinkles dominate. They postulate that "it is reasonable to expect that the actual behavior of a space suit falls between these two extremes" and that elasticity and volume changes impact the bending moment and therefore mobility.

This work was not used to inform the design due to finding the research after the project was well underway, however, the bending moment experiments performed on the proposed design's polyimide tubes were still instrumental in determining if this material would perform well for the architecture's application. Below, these experiments are explained.

### 4.1.2    Bending Moment vs Angle Experiment for Proposed Polyimide Tubing

In order to characterize the mechanical response of the radiator design's polyimide tubes during deployment, we have performed bending moment experiments under various static pressures in a force-displacement bending rig, see Figure 4.2.
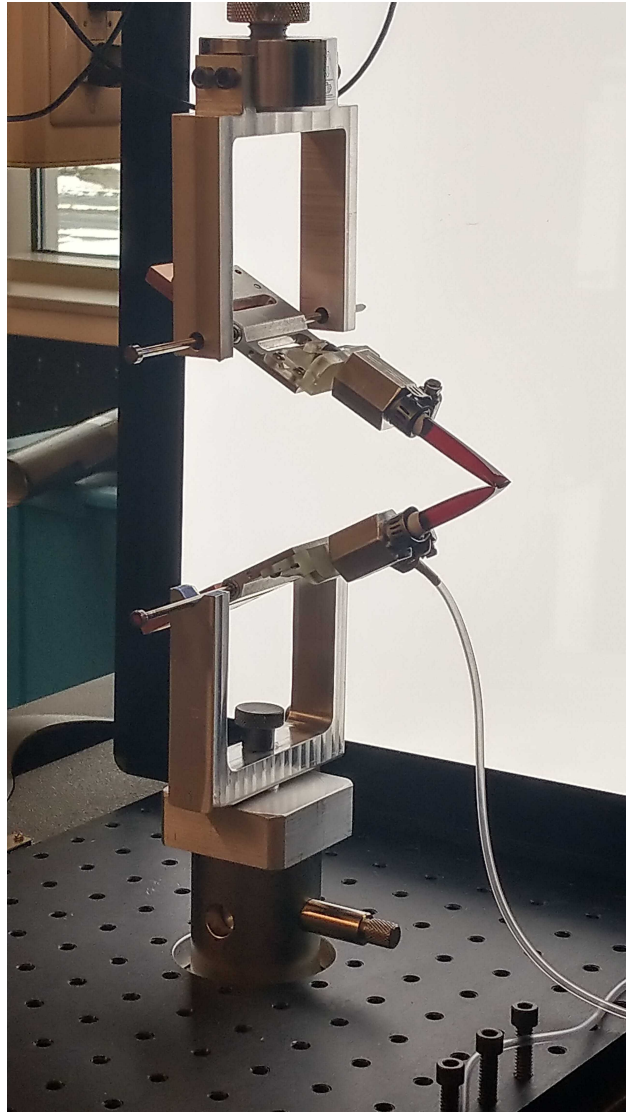
Figure 4.2: Image of Instron setup for pressurized bending moment experiments

The experiment is similar to the Column Bending Test used to characterize the bending failure of high strain composites [67]. It uses grips with ball bearings, that are actuated in an universal testing machine (Instron 5969 with a 100 N load cell), so that vertical displacement of the cross-head results in rotation of the grips. A video of the test is recorded, and a Matlab in-house code is used to calculate the angle in which the two halves of the tube meet at the kink, as well as the distance to the bearings, so that the bending moment can be calculated from the vertical force. Effects of gravity are minimized using offset weights to balance mass. The test starts with

the sample folded, and then it slowly applies displacement to open the hinge at a rate of 1 mm/s while measuring the force. Constant pressure is applied to the inside of the tube throughout the test by the use of a small tube connected to a pressure regulator. This tube is placed on the bottom grip such that the weight of this tube will not be measured by the load cell, which is connected to the top grip assembly.
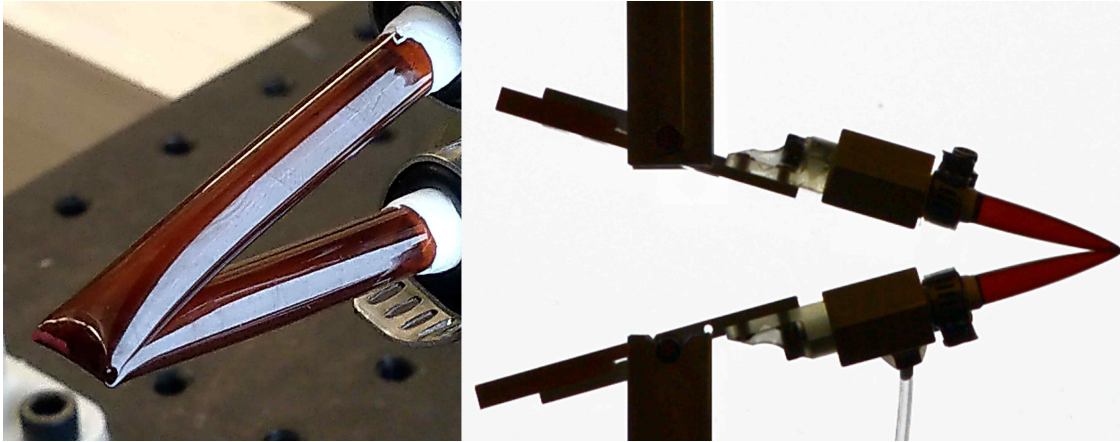


Figure 4.3: Left and center: images of the proposed thin polyimide tubes in a bending test rig. Right: double right-angle bent tube attached to radiator panel brackets in a realistic configuration

The moment-angle relationships provided by the experiment are shown seen in Figure 4.4, with three identical samples ($p_1$ to $p_3$) subjected to increasing levels of internal pressure (from 0 to 200 kPa). An angle of 0 ° corresponds to the tube fully folded, and 180 ° to a fully deployed tube; positive moment results in opening of the hinge. The dimensions of the samples were inner diameter 7.70 mm, thickness 0.069 mm, and length including grips is 100 mm.

The data shows an initial region with high bending moment at small angles (here limited to 20 ° by physical apparatus constraints), due to the contact that can be seen where the two halves meet. Partway through, we see a region of a relatively flat relationship in the zero-pressure moment-angle curve. Adding pressure increases moment and in the central region, the increase in moment is roughly linearly with pressure, with a minimum value around 20 Nmm for 200 kPa of static pressure in the tube. For a hinge on an actual design, the expected regime would be within 90-180 ° with a double right-angle bend, chosen because a single fold with this material cannot

easily conform to two parallel cylinders.

Experiments also showed that the tested polyimide tube shown would be able to withstand a minimum of nine cycles of repeated opening and closing cycles with no failure or leaking of air. Thicker samples (above 0.086 mm) of similar diameter were not able to survive the nine repeated cycles. More work should be done to determine the ideal thickness, as the tested sizes were limited by commercially available tubes. Additional cycling of the fold has been demonstrated to cause failure in thicker samples that were tested beyond the nine cycles used in this study. This work has not characterized the survivability of these kinked tubes over a long period of time, or looked at the effect of radiation, so future work will need to follow up to verify that these joints can stay sealed and operable over an expected mission's duration.
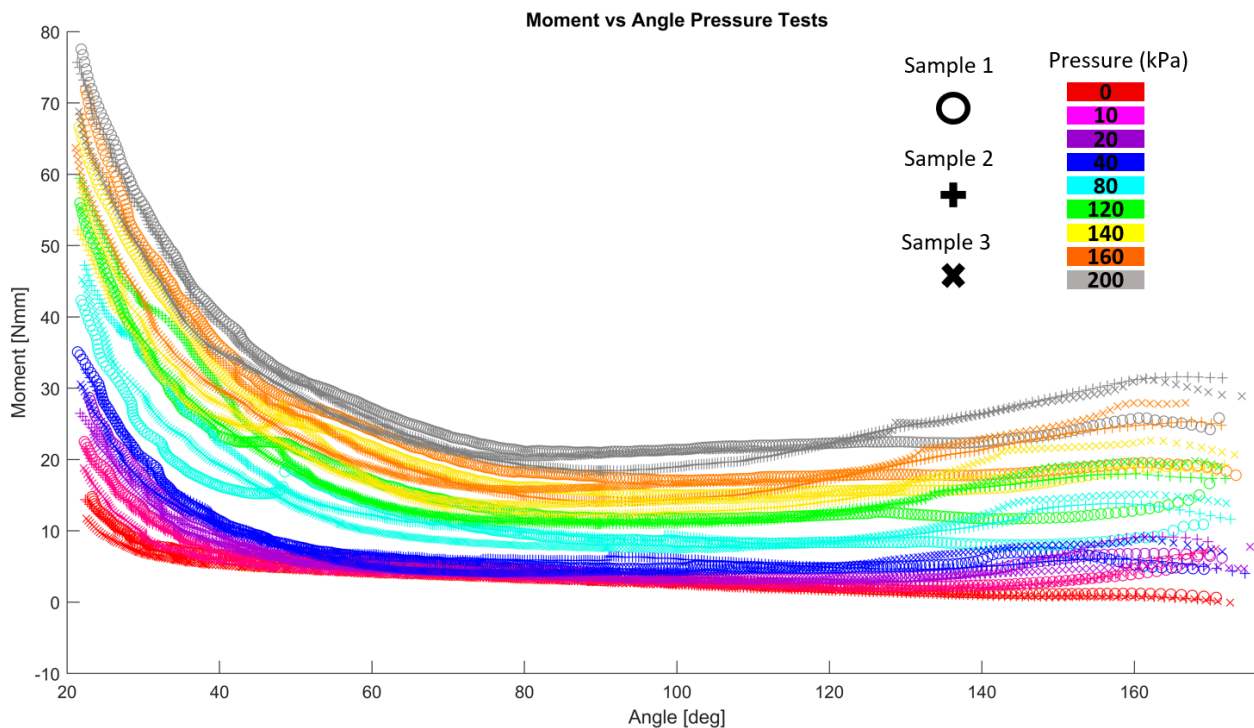


Figure 4.4: Moment vs angle curves for a thin polyimide tube 7.7 mm inner diameter, 69 micrometers thick under varying static gauge pressures. Here, and angle of 0 ° refers to a folded-in-half state and 180 ° refers to the unfolded configuration

What can been seen is that for each of these tests, there is a direct pattern that as pressure is increased, the moment is increased. In fact, this relationship appears to be linear, as shown in

Figure 4.5 below.
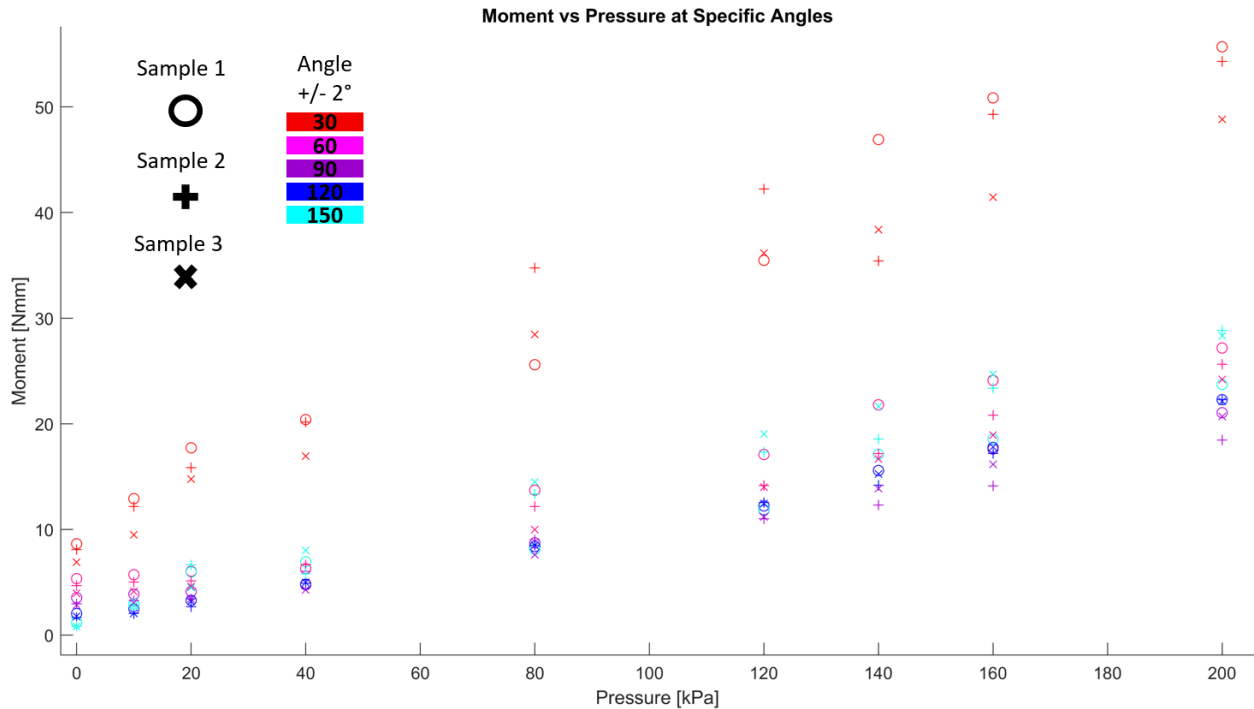


Figure 4.5: Plot of moment vs pressure at specific angles during unfolding for a 7.7 mm inner diameter, 69 micrometers thick polyimide tube

For the purposes of the radiator design, these experiments provide an estimate of the expected moment on each hinge during deployment. More importantly, the moments are always positive, and easily tuned by applying internal pressure. These results can therefore be used to simulate the dynamics of deployment and find an optimum internal pressure resulting in a robust and repeatable opening of the panels.

### 4.1.3    Experimental Set-up and processing

The experiment uses an Instron Testing Machine along with modified bending grips to open up kinked tubes from a closed to a fully opened position. A light and small tube carries pressure to the tubes by way of a custom machined tube holding bracket with a port on the bottom. The experimental setup and procedure is listed in the appendix H below.

For processing, first, the Instron is set to collect the displacement, time, and force during the

experiment, and a camera with telephoto lens is used to capture how the angle changes over time from the base of the tubes. A custom Matlab script using image processing turns these videos into angle over time data, and also distance of the joint from the center over time, to help determine the bending moment. This code is included in Appendix B below with the rest of the data. From there, the bending moment is calculated based on the force acting on the half of the grip assembly, taking the observed distance of the kink to the center of the machine's bending grips, and getting force times distance.

As the videos and Instron data are not perfectly synced, the code asks the user to manually select what appears to be the start of the motion by looking at the angle over time plots. Then, the moment-angle plots can be generated.

Here, an example of the plots used to create these moment angle plots are included.
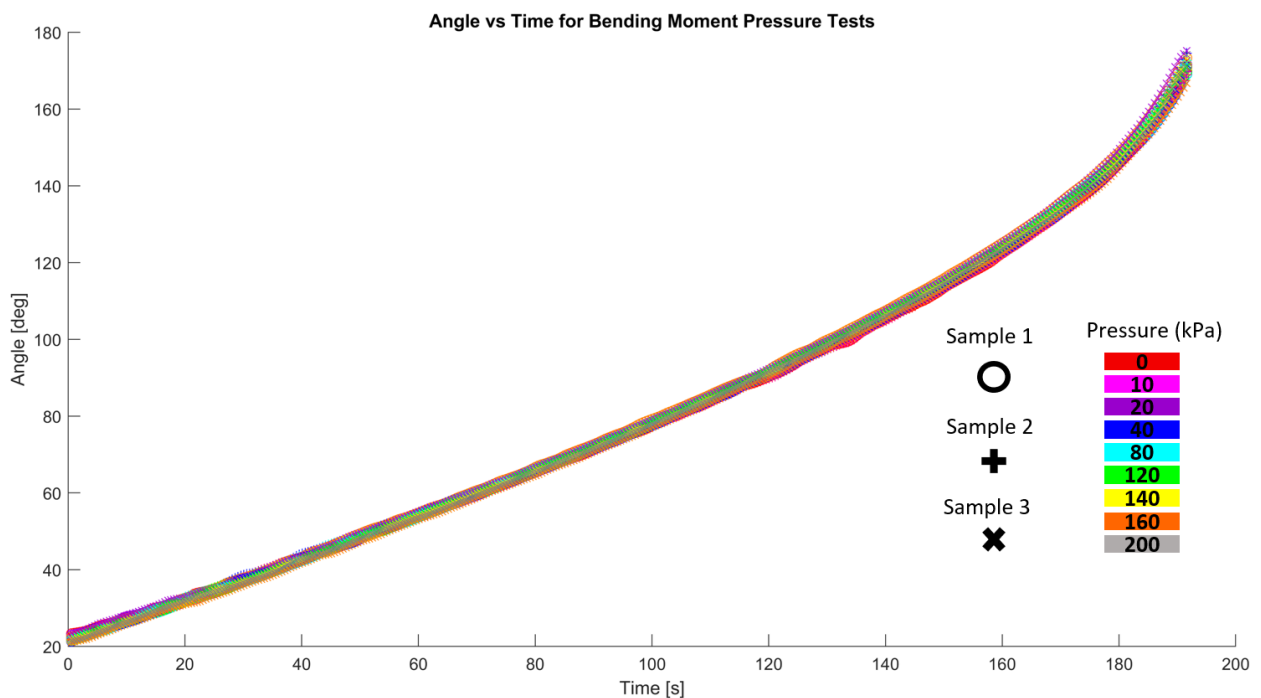


Figure 4.6: Plot of angle vs time, found using the difference from the top and bottom grips
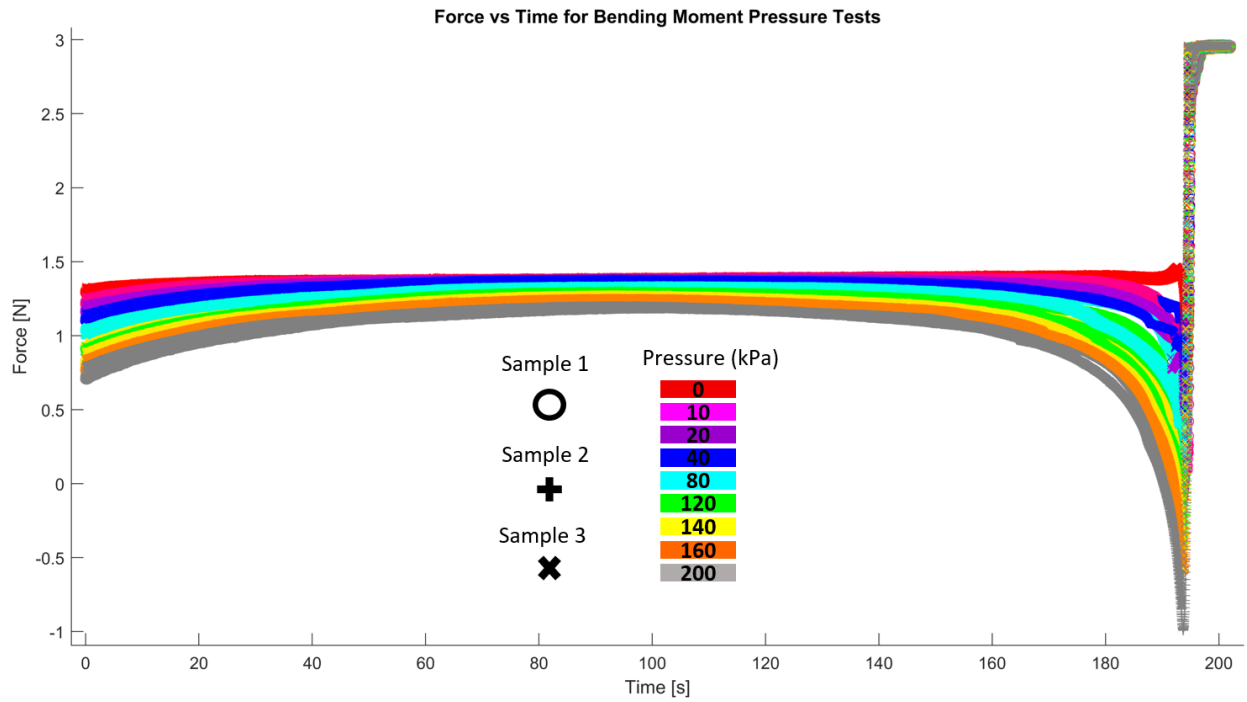
Figure 4.7: Plot of force on Instron vs time
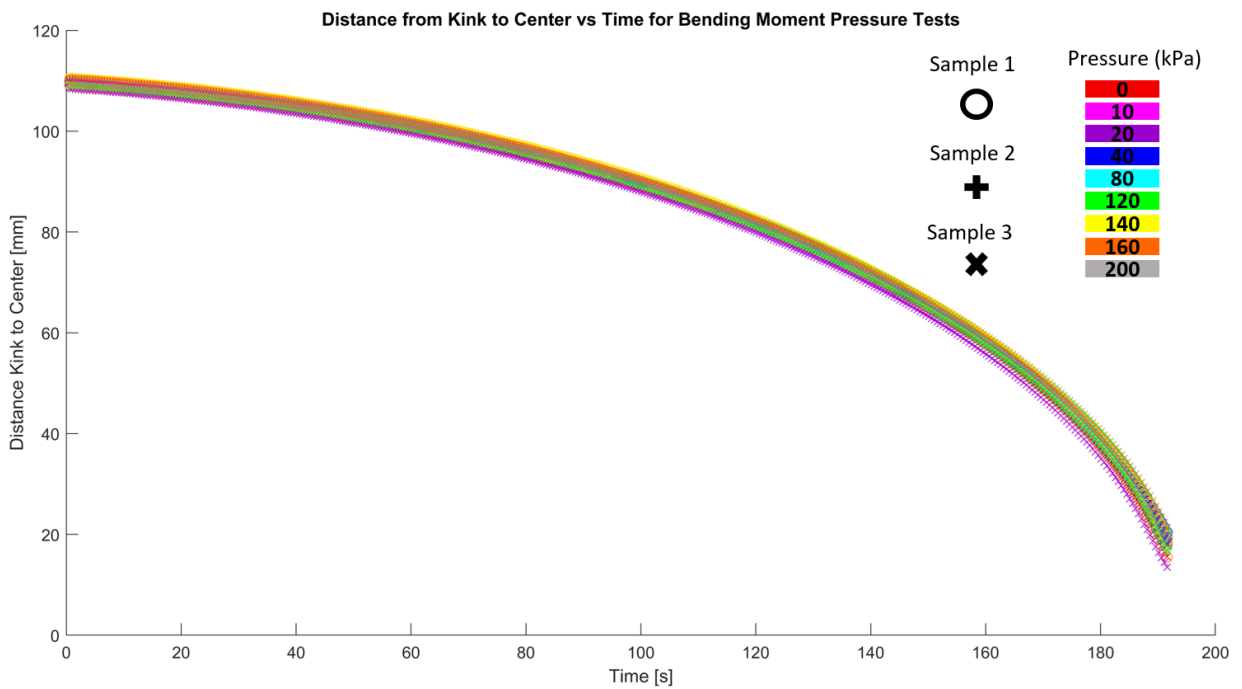


Figure 4.8: Plot of distance from the kink to the center of the Instron vs time

### 4.1.4        Moment-Angle Experiment for Multiple Tube Materials and Geometries

This test was repeated for many different materials and geometries, with always three samples for each to ensure repeatability and the parameters can be found in Appendix I. While the data for these bending moment vs angle tests is included in data archive Appendix B below, this work is not used to draw conclusions in the current radiator project except to show that other materials were tested as potential candidates instead of polyimide tubing. Polyimide was selected over the other candidates because it has a high modulus of elasticity, bent repeatably without failure at certain thicknesses, has great cryogenic performance, and history in spacecraft applications. The data for the other examples is included for the sake of future reference by researchers.

## 4.2        Modeling the Dynamics of Linked Rigid Panels

### 4.2.1        Lumped Element Rigid Panel Model

A dynamic analysis was performed to understand the fundamental natural frequency, and determine if the structure would be stiff enough for certain applications. A lumped element model was created by assuming the panels are rigid bodies, and the thin kinked polyimide tubes act as torsional springs. Newton's second and third laws were used to derive the equations of motion of the system for any number of panels. The system was analyzed and solved in Matlab. The derivation of this model can be found in Appendix J below. Notably, the spring stiffness of the polyimide tubes was found by comparing a small tube element with an equivalent spring-panel element to find that k=EI/L. The assumption can be made that thin pressurized tubes act as elastic beams when they are not wrinkling or buckling [68].

This analysis assumes to worst case mode of vibration to occur in the plane with cross section through the fluid tubes, where two sets of 14 panels swing up and down. Other modes may couple the double sets of panels in torsion, however, this is not expected to be as low a natural frequency as the swinging motion. As well, it becomes more difficult to analyze with the ropes that couple the panels together. In this case, the two sets swing together, and symmetry can be used to make it

a 14 panel system, whose vibration will be the same even if doubled. Future work should consider developing a higher-fidelity dynamic model with these additional modes.

The first several mode shapes are shown below in Figure 4.9.
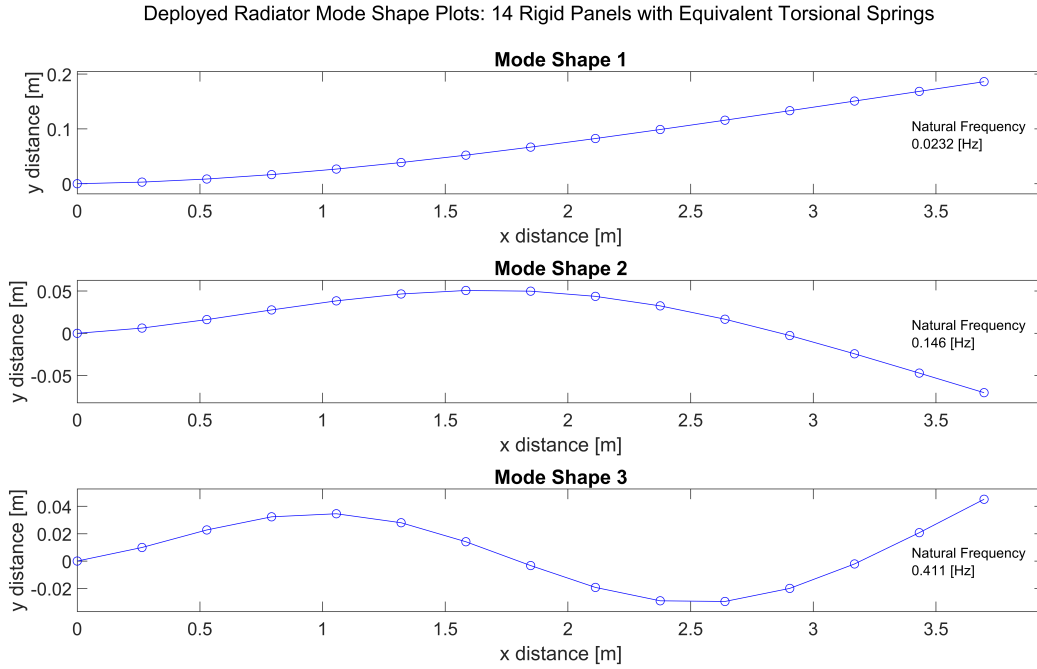


Figure 4.9: Deployed radiator mode shape plots: 14 rigid panels with equivalent torsional springs

### 4.2.2    Equivalent Stiffness Free Vibrating Beam Verification Model

The model's fundamental frequency was confirmed to represent the same result as a beam with equivalent bending stiffness.

From fundamentals of finite elements, where K is the torsional spring stiffness matrix, $\theta$ is a vector of angles of the panels relative to the equilibrium position, M is the bending moment load vector at the joints:

$$K\theta = M \tag{4.1}$$

$$\theta = K^{-1}M \tag{4.2}$$

For unit moment applied at the final hinge

$$M = [0, 0, 0, ...0, 1] \tag{4.3}$$

The stiffness matrix was derived from the lumped element model solved by applying Newtons first law. See appendix J below for the exact derivation

$$K = \begin{bmatrix} (k_{0,1} + k_{1,2}) & -k_{1,2} & 0 & 0 & & & & 0 \\ -k_{1,2} & (k_{1,2} + k_{2,3}) & -k_{2,3} & 0 & & & & \\ 0 & -k_{2,3} & (k_{0,1} + k_{0,1}) & -k_{3,4} & & & & \\ & & & & \ddots & & 0 & \\ & & & & -k_{n-1,n} & (k_{n-1,n} + k_{n,n+1}) & -k_{n,n+1} & \\ & & & & 0 & & \ddots & \\ 0 & & & & & & -k_{N-1,N} & k_{N-1,N} \end{bmatrix} \tag{4.4}$$

Now theta can be found from equation 3.2 and 3.3. From here on, the values for the proposed system are used in the analysis: parameters are shown below. $I_{panel}$ is the mass moment of inertia about the axis that is along the length of the PGS layers, found using Solidworks. $L_{panel}$ is the distance between panels. $m_{panel}$ is the mass of each panel along with the fluid. $E_{tube}$ and $t_{tube}$ are the elastic modulus and thickness of the tube respectfully.

$$I_{panel} = 0.0004822[kg \cdot m^2], \quad L_{panel} = 0.264[m], \quad m_{panel} = 0.1259[kg], \quad E_{tube} = 2760E6[Pa]$$

$$t_{tube} = 0.069E - 3[m], \quad R_{tube} = 0.00385[m]$$

These are used to find the values of theta

$$\theta = [0.0015, 0.0030, 0.0045, 0.0060, 0.0075, 0.0090,$$
$$0.0105, 0.0120, 0.0135, 0.0150, 0.0165, 0.0181, 0.0196, 0.0211] \tag{4.5}$$

from Euler-Bernoulli Beam Theory

$$M = EI\kappa \tag{4.6}$$

$$\kappa = \frac{\theta}{L} \tag{4.7}$$

For structure with a moment load applied to the end, we can find the stiffness by applying a unit moment load at the end, and knowing the angle $\theta$ at the length to this joint

$$EI_{struc} = \frac{ML}{\theta}_{end} \tag{4.8}$$

$$EI_{struc} = 0.1706 \ [Nm^2] \tag{4.9}$$

From theory on free vibrating beams, Harris' shock and vibration handbook [69], we know that the natural frequency for a beam should be

$$\omega_{nf} = \alpha_n^2 \sqrt{\frac{EI}{\rho AL^4}} \tag{4.10}$$

$$\alpha_1 = 1.875, \ \alpha_2 = 4.694, \ \alpha_3 = 7.855 \tag{4.11}$$

Plugging in the numbers, substituting $\rho A$ with $m_{struc}/L_{end}$ the mass and end length of the structure, an equivalent form of linear density, we get natural frequencies very close to the lumped model with modes shown above. Table 4.1 compares these results below.

Table 4.1:   Verifying Rigid Panel Dynamics Model against a Free Vibrating Beam Model

| Model Natural Frequencies [Hz] | 1st mode | 2nd mode | 3rd mode |
|---|---|---|---|
| Lumped Element Panel Model | 0.0232 | 0.1460 | 0.4112 |
| Equivalent Stiffness Beam Model | 0.0256 | 0.1604 | 0.4490 |

Considering how close the 1st mode frequencies are, it appears the lumped element model can be used with confidence.

### 4.2.3    Required Fundamental Frequency for Spacecraft

Structural design guidelines often provide the first mode, or fundamental, natural frequency requirement for spacecraft. This can often be the case to survive launch loads and deployment from a launch vehicle. For example, from AMES' in house NASA Standard, 8070.1 [70], spacecraft are supposed to have over 35 Hz and 50 Hz fundamental frequency for the primary and secondary structure accordingly. Other design guides such as Spaceflight say spacecraft 400 kg and higher

should have a minimum first mode frequency of 30 Hz [71]. However, the applicability is for AMES managed spacecraft.

More importantly, spacecraft that utilize deployable structures often have much lower natural frequency. An example is the ROSA rollable solar arrays on the ISS, whose first mode is around 0.4 Hz [72]. Others such as a 1989 Space Station Freedom Design Requirement lists a minimum of 0.1 Hz [73]. According to Hedgepeth in 1980, "present large arrays are designed for fairly low frequencies", around 0.1 Hz, and "in cases in which very tight pointing accuracy is required or in which vibrational disturbance must be minimized, frequencies of 1 Hz or more are required" [74].

Consequently, it appears that different spacecraft have different sets of requirements depending on their operation. This also makes sense if you consider that certain missions will have certain pointing requirements, and a structure in motion may hinder the ability for a camera to point on a specific target. Regardless, it appears that the current fundamental frequency of 0.023 Hz is not close to meeting the typical values seen on space stations.

### 4.2.4    Increasing Deployed Radiator System Stiffness and Natural Frequency

How can the fundamental frequency be improved for this design? Perhaps the simplest method would be to reduce the number of hinges by increasing the width of each of the radiator panels, however, this appears to have limited effect if the same total length of radiators is desired by scaling the panel width.

Reducing the deployed structure's length would help drastically. In fact, a plot was created to show the logarithmic relationship by simulating the effect of changing the number of panels from the lumped element model seen above.
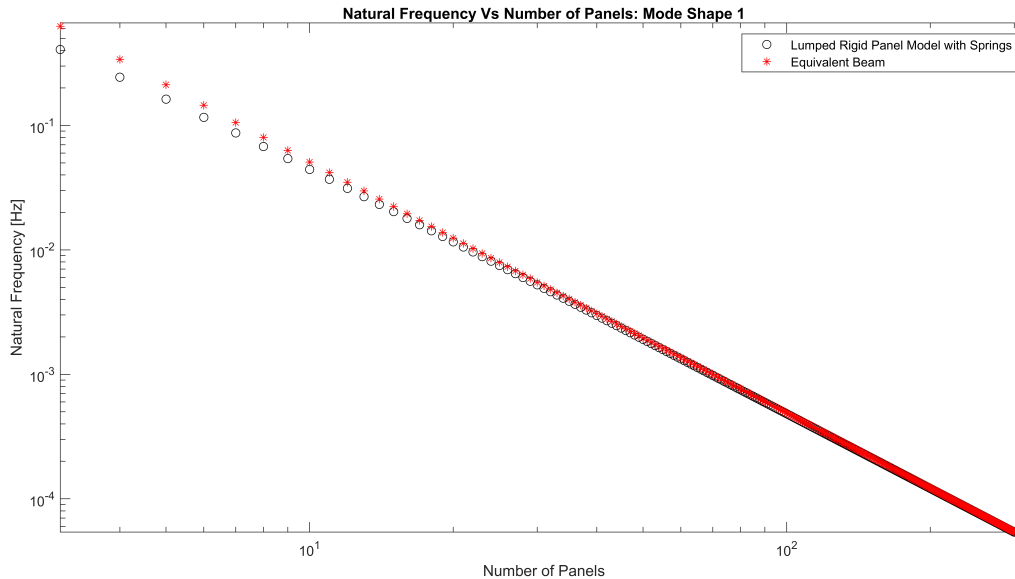
Figure 4.10: Natural frequency vs number of panels plot for the first bending mode shape, comparing the discrete lumped rigid panel model to an equivalent-stiffness continuous beam

As an aside, this chart offers further confidence in the model since the lumped element model should match a beam with the mass and spring elements. The best fit slope is -1.974, approximately -2, meaning the frequency is proportional to the inverse square of the number of panels.

$$f \propto 1/N^2 \tag{4.12}$$

Which is what can be seen from equation 4.10 above. Further, the comparison to the equivalent stiffness beam structure shows a trend that as the number of panels increased, the discrete panel model converges to the equivalent beam.

If we do not want to reduce the number of panels which would reduce the thermal performance, and mass is already as low as possible, what else can be done? Additional spring elements could be added to assist the kinked tubes in keeping the structure deployed. This idea could be accomplished by adding mechanical latching hinges between panels, or using flexible composite hinges. A designer should note that adding more elements will increase the mass, and reduce the natural frequency.

The concept for using composite elements for rigidity and deployable technology traces back

to spacecraft from the 80's, as Murphey summarizes well [7] in 2015. Flat or tape spring hinges are a possibility using these high strain composites. Below is an image of a double flat hinge design concept from prepublished material by Yasara Dharmadasa used with permission [75].
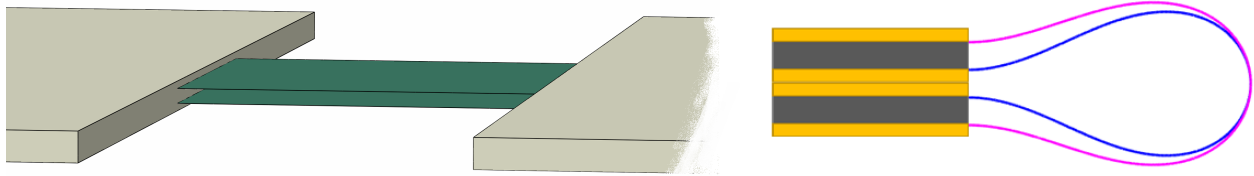


Figure 4.11: Example of a double flexible high strain composite hinge [75]

This could be modified to a tape spring hinge like that shown below, from Jeong, 2014 [76].
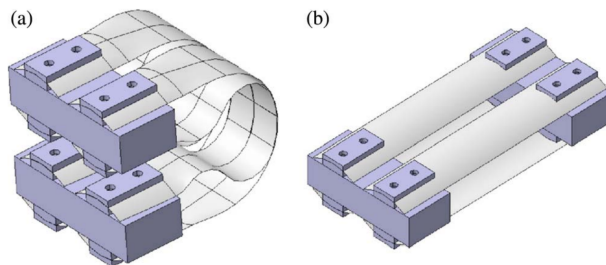


Figure 4.12: Example tape spring hinge [76]

Other more drastic ways to stiffen the structure would be to add additional mechanisms, such as a pantograph radiator. The ISS has this structure on their radiator panels. See Figure 4.13 below.

Figure 4.13: International Space Station radiator panel pantograph mechanism [77]

A structure such as this would add a lot of mass, and could partially make obsolete the weight savings from using a kinked tube design.

Finally, a latching hinge mechanism could be used to rigidly connect panels once they are fully extended [78].
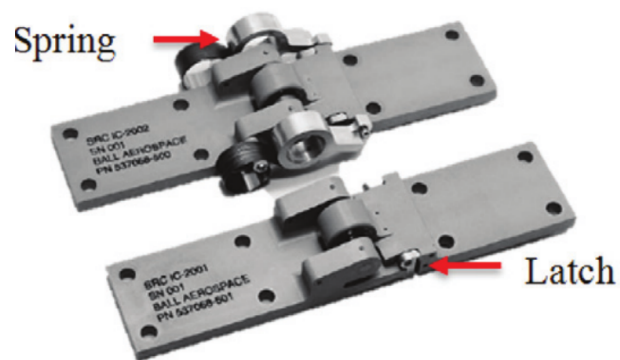


Figure 4.14: Example mechanical hinge [78]

In summary, there are a number of viable options to add to this design to increase the fundamental natural frequency to something more acceptable.

**4.2.4.1     Increasing Natural Frequency with a Double-Flexure HSC Hinge Mechanism**

Initial calculations were performed to understand if a double-flexure hinge would be able to add sufficient stiffness to increase the natural frequency to 0.1 Hz and above. Here, the image in 4.11 shows how this type of flexure would bend in a stacked panel configuration. This hinge for the proposed design has a geometry seen in the following Figure 4.15 and was analyzed with the assumption of classical beam theory (ignoring shearing deformation between upper and lower segments).
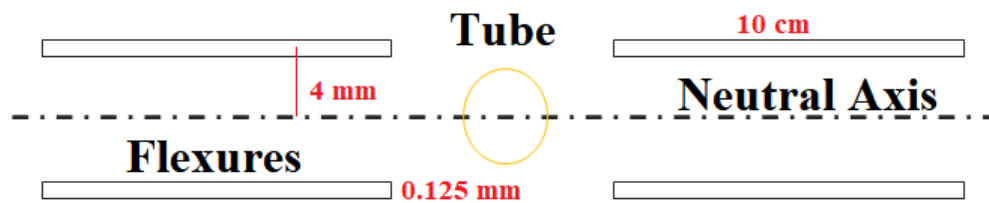


Figure 4.15: Symmetric double-flexure geometry which could increase structural stiffness to improve fundamental frequency, not to scale

The maximum length from panel to panel (including the thickness of the carbon fiber panel frame) is 65 mm, which was the assumed length of the hinges here. The inner flexure deforms to the geometry as shown in Figure 4.16 with curvature seen in Figure 4.17. This work comes from Yasara Dharmadasa as private communication using his code with permission, through the technique of solving the elastica of a thin structure, as published in 2020 by Dharmadasa [79].
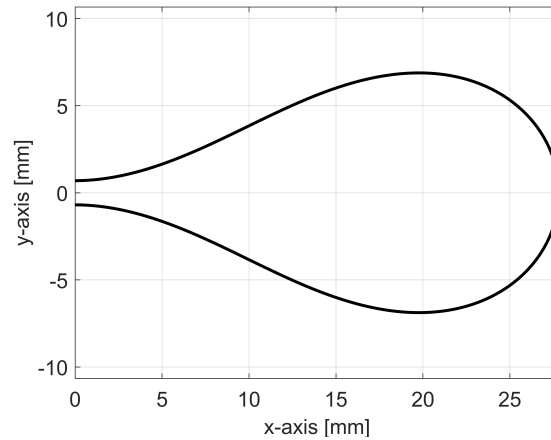
Figure 4.16: Natural equilibrium geometry of the inner flexure for the symmetric, double-flexure hinge
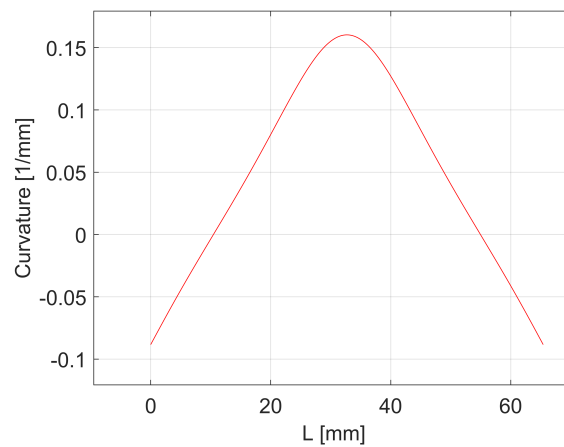


Figure 4.17: Curvature vs arc length for the inner flexure for the symmetric, double-flexure hinge

Using a carbon fiber high-strain composite (HSC) with the assumption of 1 % strain limit (which is conservative given failure strains above this [80]) and a 150 GPa modulus (from an assumption of 250 GPa fiber [7] with a 60 % volume fraction) gives the resulting 14-panel deployed system a natural frequency of 1.2 Hz in the assumed first mode shape seen in 4.9. This symmetric double-flexure hinge together weighs only 3 grams per panel connection, meaning almost negligible mass compared to the rest of the panel. If this analysis were correct, then it would mean the proposed radiator architecture could easily surpass fundamental frequency requirements for even precise-targeting spacecraft applications.

However, this analysis assumes that each double-flexure is a solid beam bending with the 2nd moment of area of the combined upper and lower flexures. In reality, there is another degree of freedom, such as translational motion, seen in Figure 4.18 below.
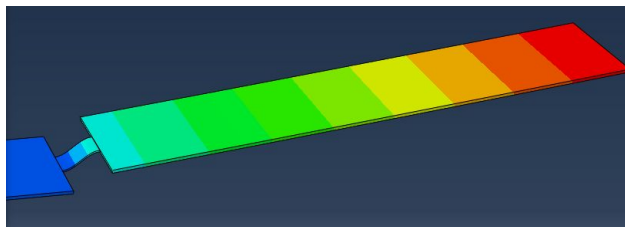


Figure 4.18: Example depiction of a double-flexure shear mode [75]

This mode shape is dominant (and sufficiently higher than 1 Hz) for a single panel configuration, but it is currently unknown how this mode changes with many panels connected together. Future work needs to be conducted to evaluate this more realistic mode. Realistically, a combination of bending and translation will be likely, and could decrease the natural frequency below the potential upper limit of 1.2 Hz from the solid beam assumption above.

Even if the existing geometry becomes insufficient, one can easily extend these HSCs wider, potentially to the maximum of about 60 cm instead of the shown 20 cm total length composite hinge. In summary, it appears possible to design a lightweight HSC hinge capable of sufficient stiffness to meet fundamental frequency requirements.

### 4.2.5 Maximum Static Bending Moment

Additional calculations were made that estimates the maximum static bending moment the structure can handle before failure. Equations from Mathon in 2005 provide a conservative estimate of the bending moment necessary to collapse a pressurized thin cylinder.

$$M_{\text{coll}} = \pi R^2 t \left( \frac{PR}{t} + \frac{1}{2} \sigma_{\text{CL}} \right) \tag{4.13}$$

$$\sigma_{\text{CL}} = Et / \left[ R\sqrt{3\left(1 - \nu^2\right)} \right] \tag{4.14}$$

Applying 2 bar of pressure to the 7.7 mm diameter polyimide tubing with thickness 0.069 mm gives a collapse moment of 85 N·mm. This value is larger than the experimental bending moment seen in section 4.1.2 which makes sense, given that buckling causes a drop in moment as curvature is increased seen from Corona in 2006 [81]: the reverse process would not be expected to immediately jump up in stiffness when unfolding.

## 4.3    Structural Analysis of a Radiator Frame

We now focus on the vibration modes of each radiator panel.

The natural frequency of the wings, first mode, is 54 Hz, as computed using Solidworks Simulation. As seen in the section above, spacecraft typically require a frequency of greater than 35 Hz during launch, and this surpasses the limit. Consequently, the wings on the radiator panel are not of concern for designing a spacecraft. Keep in mind that this is only applicable post-launch, since this is when the panels' wings are free at their tips. During launch, these panels are stowed and compressed under the membrane sheet, keeping them in place, with a different mode of vibration and frequency.
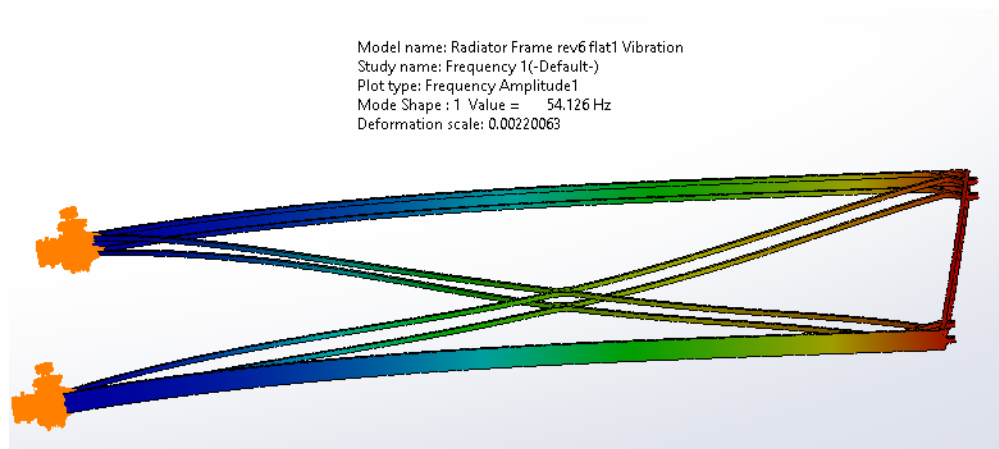


Figure 4.19: Dynamic analysis showing first mode bending of the panels composite frame

For this simulation model, we assume the clamping tube bracket is rigid: connections are fixed, due to epoxy connection. As well, the frame is assumed to have the sides connected. Here,

it is a thin strip of the same carbon fiber composite, but in reality, it would be another epoxy connection.

These assumptions also apply to a static simulation performed as well. A force of 1.24 N was applied at the edge where the CTB would be, the same force that is the weight of the panel. Fixed geometry was placed at the end of the panel frame. This represents the worst case handling conditions on Earth, where someone holds the system from a single edge. This loading scenario was used because is assumed that 1g of acceleration in space is not likely once the system is deployed. Assuming worst-case compressive failure strength along 45∘ bending direction for a 0-90 weave panel from Rockwest Composites [82], the failure strength is around 124 MPa (albeit for a thicker test specimed), so the frame is strong enough to withstand this maximum stress concentration of 71 MPa. Realistically, the weave of the carbon fiber would be aligned with this bending direction, and the strength is then much higher, around 352 MPa when under compression, and even higher under tension. The maximum displacement from this analysis shows only 2.4 mm which would occur at the clamping tube bracket, although more is expected for the opposite-wing frame. This analysis also assumes that the PGS does not contribute to the structural integrity. To summarize, these tests demonstrate that the extremely thin carbon fiber frame (1.5 mm wall thickness) is still enough for careful handling on Earth. See the images of the FEA results below.
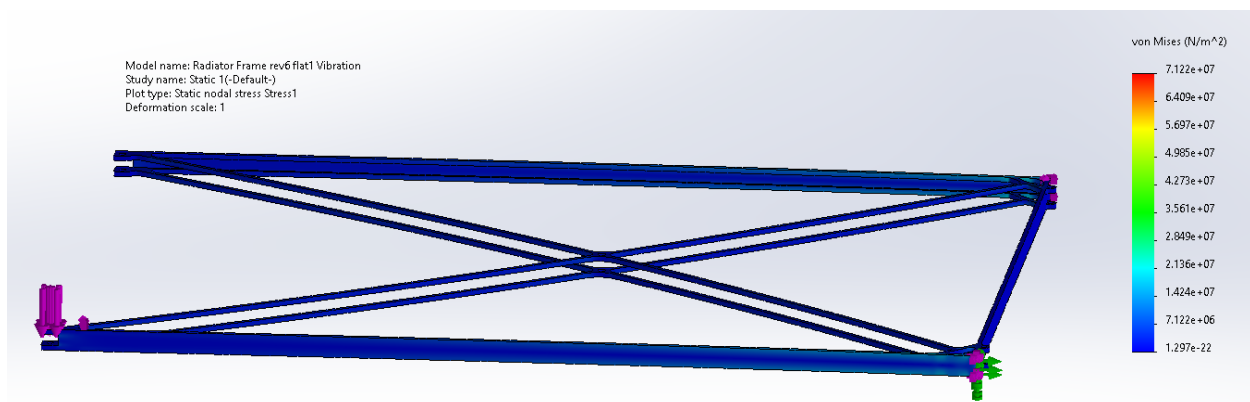


Figure 4.20: Stress plot of single radiator frame
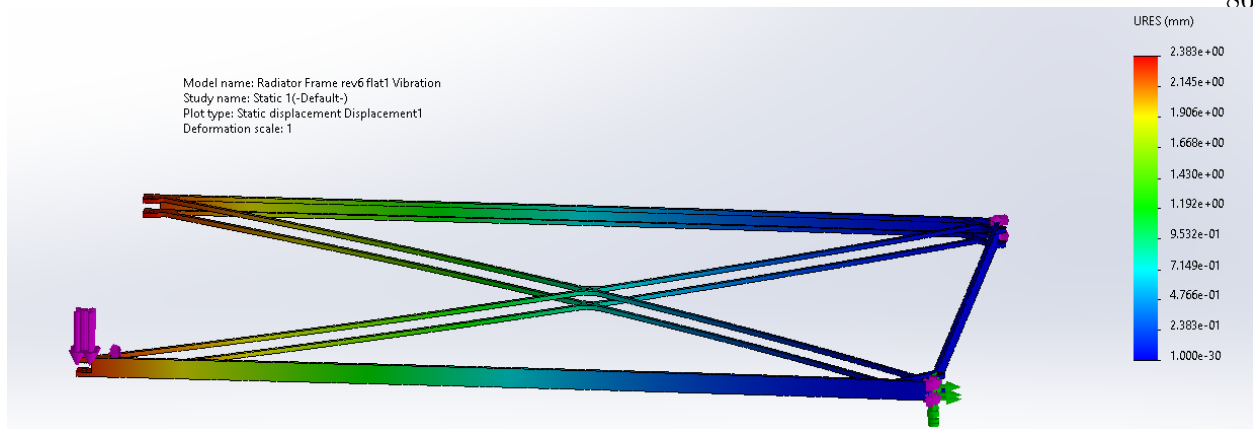
Figure 4.21: Displacement plot of single radiator frame

In space the only loads would be gentle accelerations. During launch, these frames would be tucked together with an out-of-plane load going through the corner locating pins as well as the brackets, but no significant bending loads like those experienced when handling on Earth.

## 4.4    Deployment Validation and Fluid System Prototype

### 4.4.1    Purpose of Experiment

A fluid deployment prototype was created to validate the fluid system, and show that the deployment by the thin kinked tubes was possible as this has not been demonstrated before.

Using the fluid deployment system prototype, a reduced number of panels from the space-version, 6 in total, were deployed using the kinked polyimide tubes connecting them. 6 panels were used instead of the 14 suggested in the proposed design to make manufacturing easier, and cost reduced. In section 4.1.2 above, it was showed that the polyimide tubes exert around 20 Nmm of torque at the joints from 2 bar of static pressure alone, depending on the angle of the joint. One of the main purposes for this prototype was to qualitatively examine whether these panels deploy one-at-a-time or together, and look at how these angles of the joints progress.

### 4.4.2    Two-Axis Gravity Compensation Rail System

A two-axis gravity compensation rail system was necessary to allow the panels to deploy naturally as if they were in space. One of the challenges in designing this system was that the panels needed to stack 11 mm apart from each other; commercial linear bearing systems were too wide, and would not allow to be panels so close together. Consequently, a novel staggered approach was taken where small bearings were used directly on the aluminum t slot rail structure. Carbon fiber rods and traditional linear bearings that slid along them were used for the transverse direction's motion.

The second large challenge was to keep the system lightweight, and as frictionless as possible while on a budget of a couple thousand dollars. Carbon fiber was used for the rods that connected the two sides of the rails for this purpose. 3D Printed frames were made to house the bearings, and aluminum rods were fabricated to connect them together.

The result is shown below, with a rail system that allows for 1 meter of travel transversely, and enough length for 6 panels to open. The mass of the moving parts above the panels was 156 g, which includes the 3D printed bearing assembly and carbon fiber rods. The weight of the linear bearing that slides with each panel is 22 g, and the panels themselves weigh 126 g without fluid.
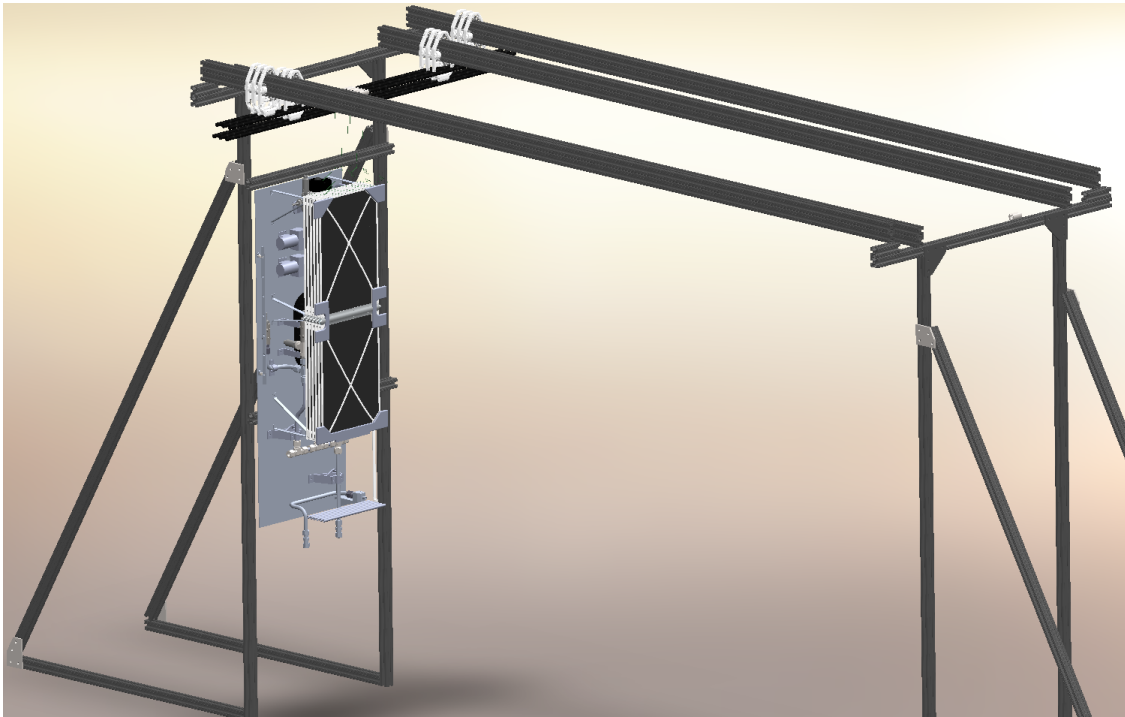
Figure 4.22: Two-axis gravity compensation rail system 3D model

Figure 4.23: Left: two-axis gravity compensation rail system built and operational. Right: video demonstration of two-axis motion for a single panel being pulled along. Link

### 4.4.3    Prototype Fluid System

Modifications to the fluid deployment prototype from the proposed spacecraft fluid system design included a flowmeter to measure flow rate, and removed temperature sensors which wouldn't yield useful data with the environmental conditions being so different.

An image of the fluid system is below.



Figure 4.24: Image of the prototype fluid loop system without the radiator panels attached. Pictured here is an accumulator, pressure sensors, a solenoid valve, a flow sensor, check valves, pumps, the tubing, and the electronics for control and measurement

Figure 4.25: Image of the lower tubes representing what would be a second set of panels in the proposed design. They are hung using strings attached to the panels above
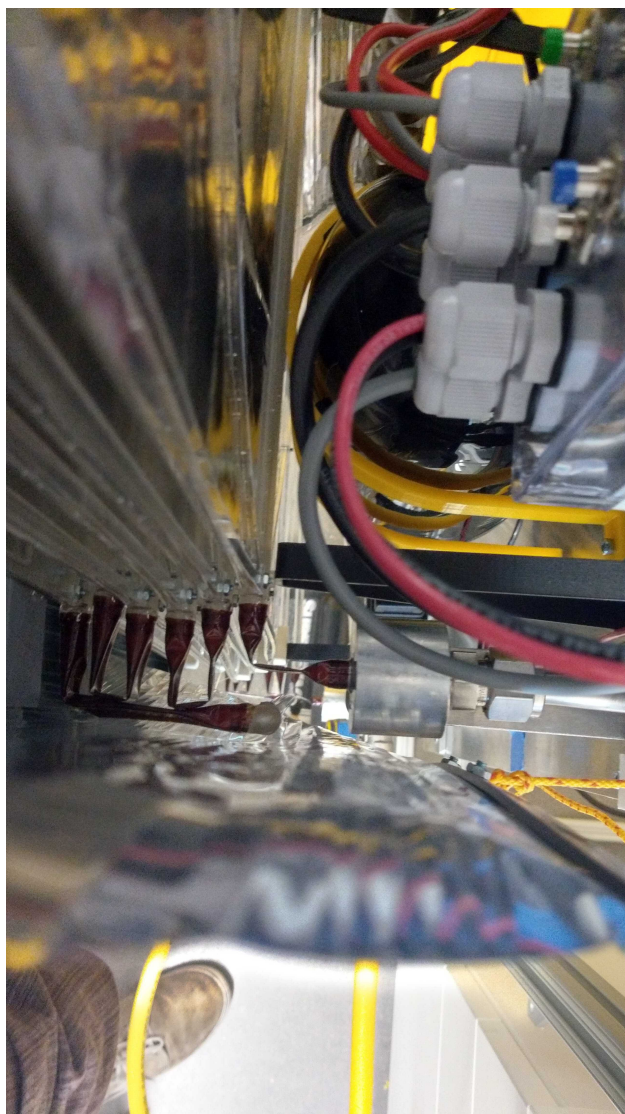
Figure 4.26: Picture of the internal tubes connecting panels after pulling partial vacuum

The fluid system was created to be able to run both static air pressure into the system, and also water stored in the accumulator as shown. An electrical system to measure pressure and flow was added, and also open the solenoid valve for both fill/drain purposes, and also to start the deployment. Unfortunately, a number of issues plagued this first pass of the Earth prototype fluid system, and ultimately, only the static pressure tests were able to show the deployment.

The accumulator was shown to be effective on a part-scale test, with water shooting out when pressurized air was applied around the bag of water in the tank. However, despite using a vacuum pump to evacuate the working fluid bag, not the right amount of water was able to fill the tank, and either there was not the right volume of air to expand and push the water, or there was just too little water in the tank to fill the (previously vacuumed) system with water and pressurize. Secondly the solenoid valve, which in testing worked fine, started leaking the pressurized air and water despite operating conditions meeting manufacturer specs. As well, once the system was vacuumed, released,and the tubes filled with water, it was extremely difficult to purge the trapped water-air mixture out of the polyimide tubes. Kinked tubes were able to be vacuumed when dry, seen in 4.26 above, but not vacuumed with liquid inside. Even blowing air through was only partially effective initially (visualized with the air bubbles slowly moving through the zigzagged tubes), and slowed to a halt. With trapped air in the line, it was not possible to have the liquid fill the system with pressure as intended.

These prototyping efforts have some important ramifications for the proposed design. It is important that designers take into consideration the effect of a closed kinked tube when purging and vacuuming the lines. Procedures might need to be put into place such that after every test, purge and vacuum are done while the panels are in a deployed state. The rest of the issues relate to hardware, and could likely be fixed by sourcing high quality (and expensive) aerospace components. Other aspects would need to include proper hardware regardless, such as replacing Schrader valves with fill/drain ports instead, and purchasing a legitimate accumulator, instead of using a paintball tank with custom fitting. Overall, more rigorous testing needs to be done to validate the general fluid-system design.

### 4.4.4    Packaged State

This prototype was also able to simulate the release mechanism effects on the design, by implementing the scroll sheet mechanism for this reduced panel mockup. Here, rope is used with a "figure eight" 3D printed endpiece, that holds the rope in tension with a screw. The sheet connects to the rope by printed strips with holes for the rope as well as springs.

This sheet was built using 0.13 mm metalized PET film, rolled by hand with two people to create sequential creases. An image below shows this process in action. By creating this permanent deformation along, the sheet's new equilibrium position is in a cylindrical curl with diameter 40 mm.



Figure 4.27: Rolling the PET film by hand

Images of deploying Jig in the packaged state are below.

Figure 4.28: Left: packaged deployment prototype front view. Center: Packaged deployment prototype with staggered sliding rails. Right: Packaged deployment prototype side view

Note that 3D printed corner pieces needed to be added in for this prototype such that panels could stack with the correct distance apart. The small locating pin features in the corners of the panels were not sufficient with the large tolerances of the strung panels of this prototype.

### 4.4.5    Deployment Videos

The most important feature of this prototype is best demonstrated on video. The deployment process is shown, where the panels successfully extend outwards.

The first video from the perspective of the rail system is below. Included in all of these are links to the videos themselves.
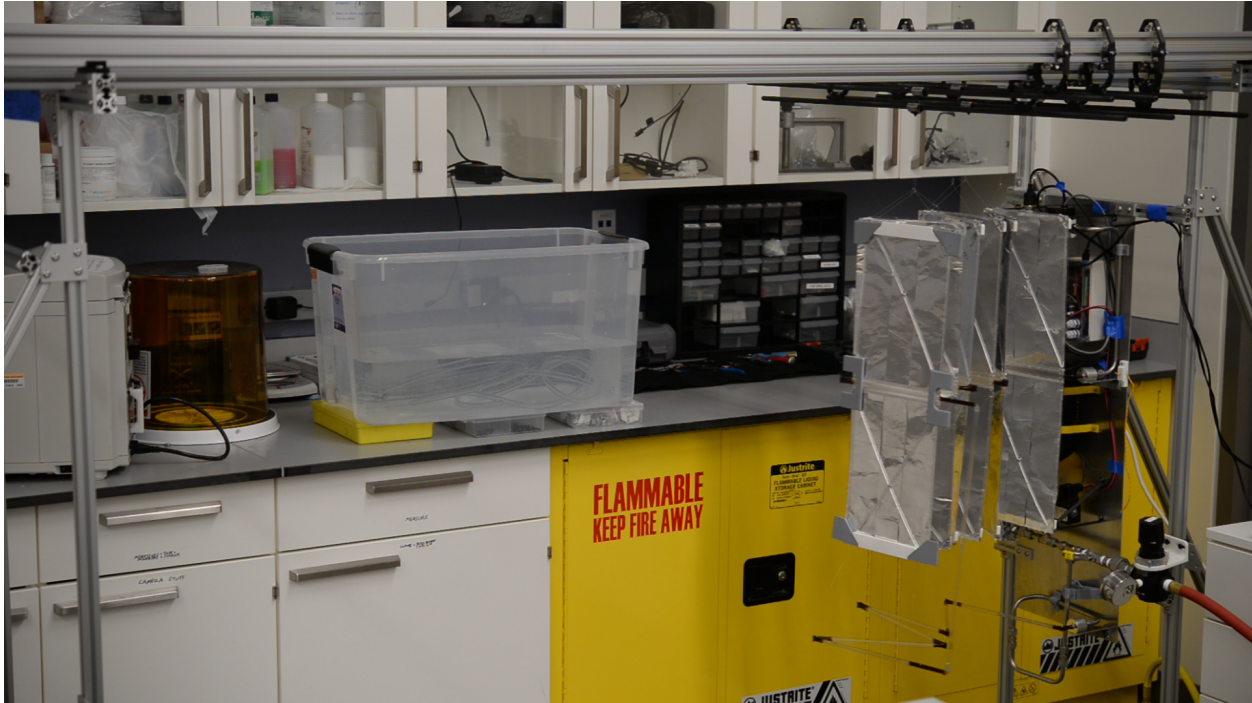
Figure 4.29: Video of the entire deployment process from scroll release to full extension with 2 bar of gauge pressure. Link
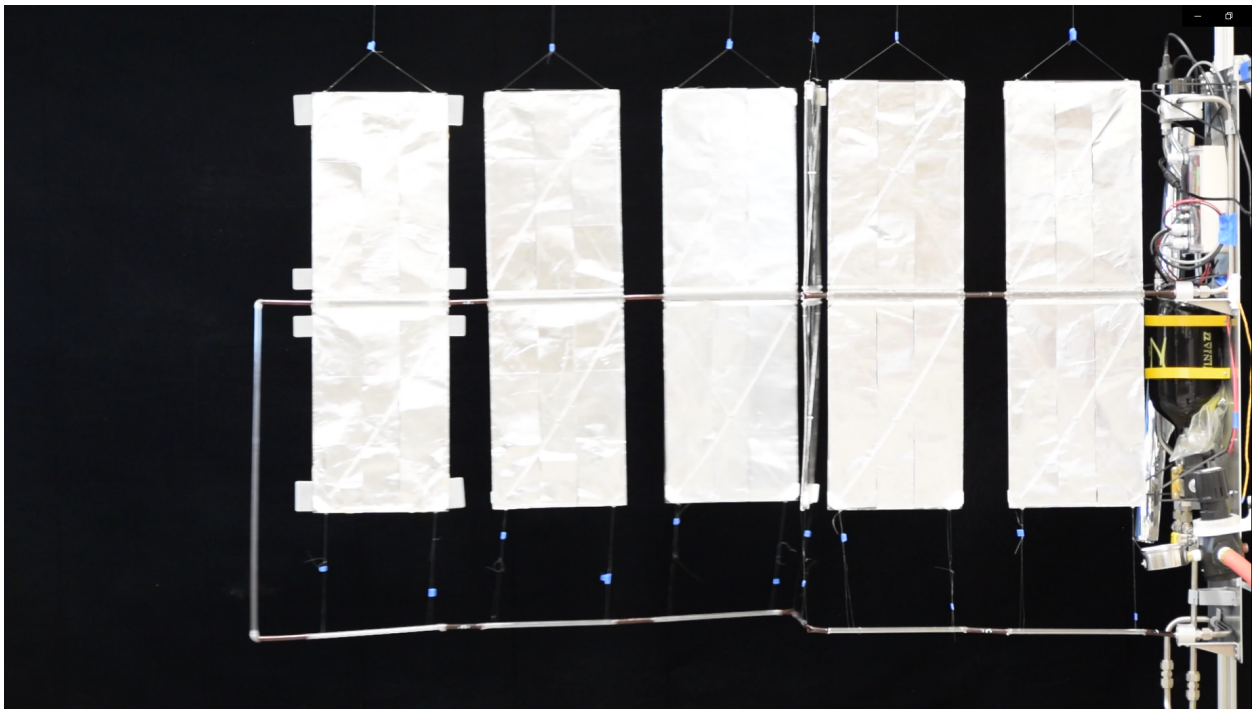


Figure 4.30: Video of the side profile shot of the deployment process, at 2 bar of gauge pressure. Link
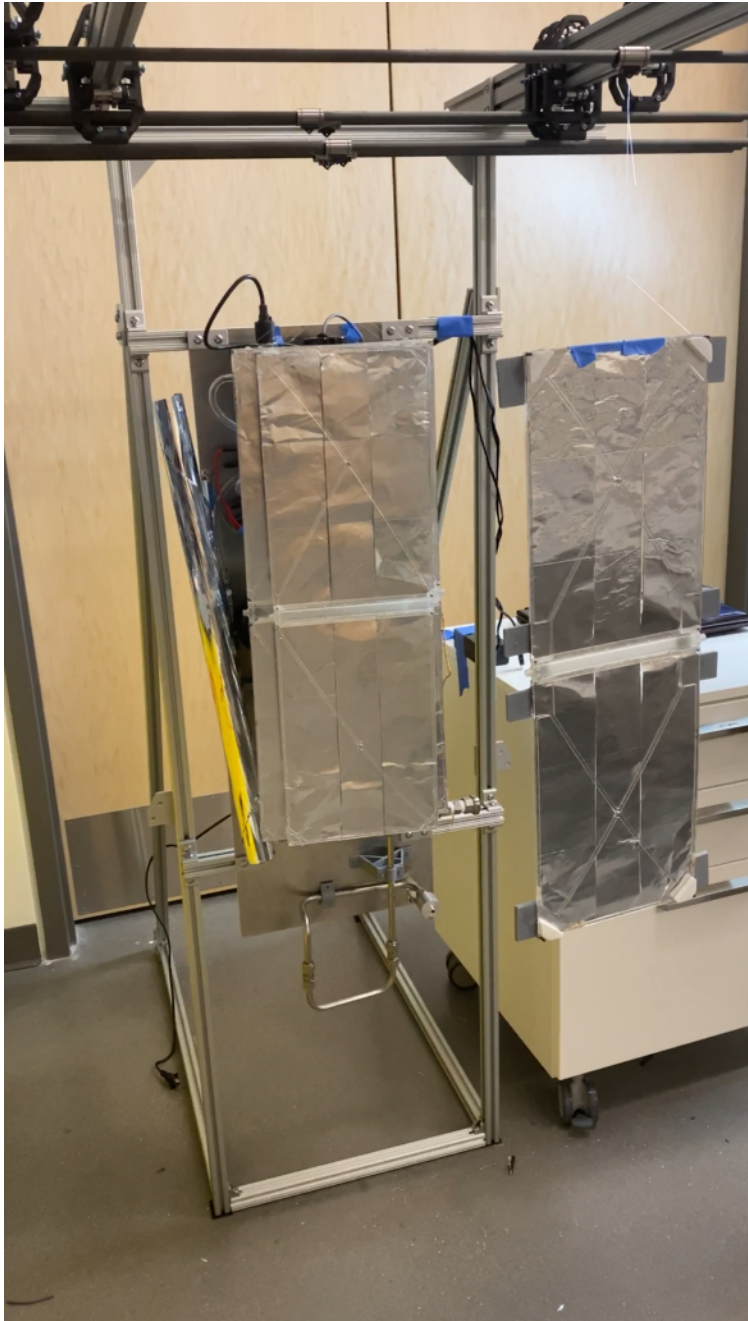
Figure 4.31: Scroll release video. Link
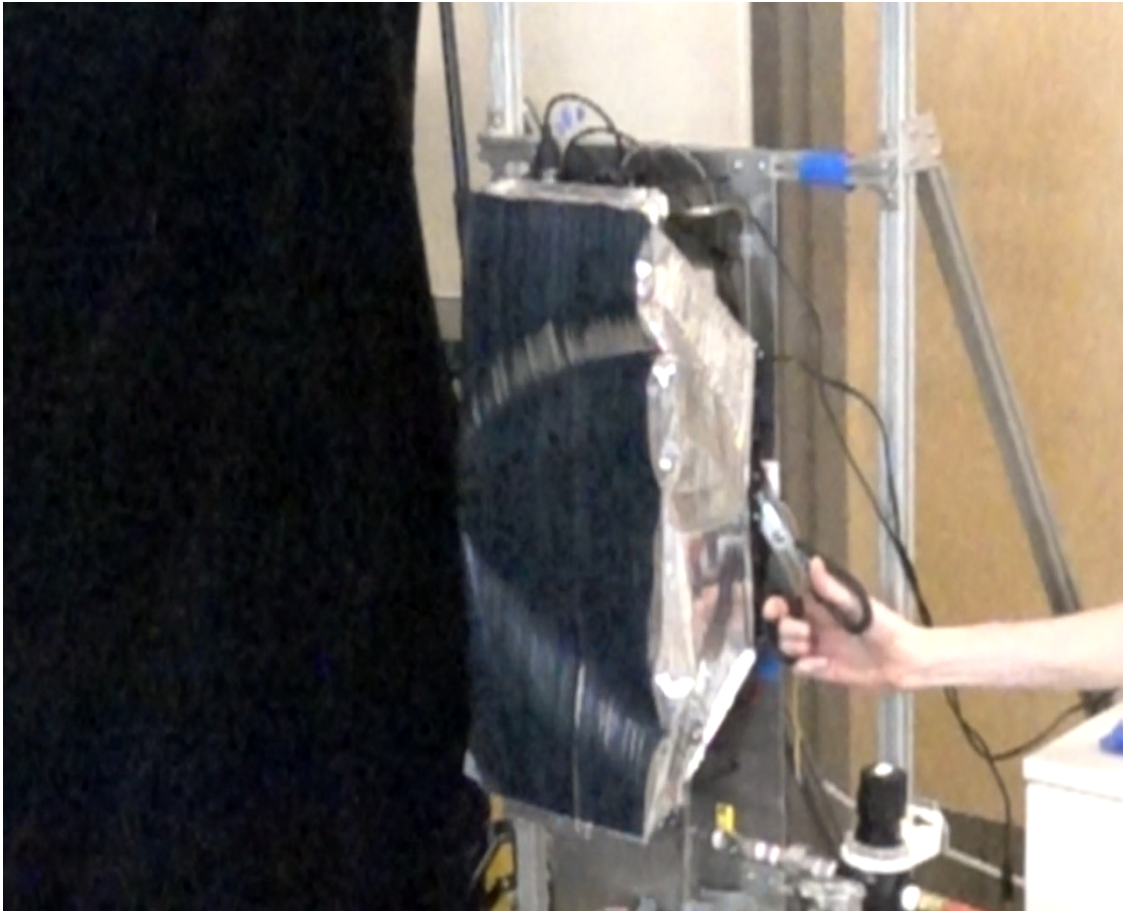
Figure 4.32: A 16x slow motion video of the scroll mechanism release. Link

### 4.4.6    Issues and Results from the Deployment Experiment

#### 4.4.6.1    Issues

After running the same experiment at 2 bar for many attempts, the polyimide tubes would often leak right at the kinked joints, and need to be epoxied again. This happened because the thickness of the polyimide tubes was larger than what was ordered from the manufacturer, and due to time constraints, these were still used in place of the other thinner tubes. From the experiments ran in section 4.1.2 above, we saw that at the proposed thickness of 0.069 mm, these tubes would be able to withstand many repeated bends, whereas the new thickness would start leaking only after a handful of bends.

Furthermore, it was often the case that the system would only open partway, likely caused by

a couple of different factors. First, sometimes the string hanging the lower tubes from the panels would wrap around others and tangle because of the knots in the line. Second, if the epoxy wasn't fully cured, sometimes the globs around the polyimide tubes would stick, and the joints would stay closed. Lastly, the linear bearings would sometimes get stuck (perhaps a piece of dust went into the bearing), and cause the system to get caught partway open. Furthermore, at 1 bar, it was not possible to get the expected full deployment, because of these issue outlined above. These concerns largely disappear for the proposed system thankfully, as no gravity compensation system will cause friction, and the lower tubes would be replaced with a more ordered stack of panels that can only deploy a certain way.

### 4.4.6.2    Results

This fluid deployment prototype has successfully demonstrated that the system deployment would likely succeed in the microgravity space environment. An accumulator system that can push fluid through the panels and then pressurize would be able to achieve the deployment without the need to turn on the pump.

We have found that the polyimide tubes at the current 7.7 mm diameter will need to be thinner than the prototype (0.086 mm), around the proposed 0.069 mm thickness or potentially thinner to deploy without cracking at lower temperatures, which this test was not designed to evaluate. Future designs should certainly incorporate rope that connects the two sets of panels such that they deploy together, as this was shown to be necessary for the lower tubes to pull the panels open.

The design of the two axis rail system performed admirably given the time, budget, and panel compression constraints, and a system such as this could certainly be replicated for future deploying experiments. Lastly, the scroll sheet mechanism was a success, and I have shown that it can roll and tuck away neatly beside the fluid system as hoped. While weighing only a couple hundred grams, this deployment mechanism can both restrain and deploy the many panels stacked underneath it.

# Chapter 5

# Conclusions and Future Work

## 5.1    Conclusions

A new type of pumped-fluid-loop deployable radiator system has been conceptualized and prototyped that can theoretically reject about three times the heat per unit mass compared to similar recent technology. The system relies on novel radiator panels utilizing pyrolytic graphite sheets in a tapered and layered configuration to efficiently reject heat from a central source. The panels are connected using thin polyimide tubes. The thermal-fluid system provides the deployment mechanism and structural integrity by connecting panels. Thin tubes transfer heat, act as a hinge, and structurally connect the panels to the spacecraft resulting in a significant reduction in weight and complexity. Experiments were completed that characterize the internal bending moment of these kinked tubes as a function of static pressure and angle, validating the design and potentially enabling future analysis to predict the panel deployment. For the release mechanism, the design combines previously demonstrated burn wire technology with a novel scroll sheet mechanism that releases to expose the stack of panels. Redundancy in the proposed single-phase mechanically pumped fluid loop was matched to be the same as Mars Science Laboratory and Parker Solar Probe spacecraft with two pumps set up in parallel. A fluid deployment prototype demonstrated the capabilities of the system to deploy under static pressure that would come from the accumulator, and successfully verified the scroll sheet mechanism. Significant mass savings in the fluid system are achieved by eliminating the need for a bypass valve, and by changing to a composite over-wrapped accumulator design. A detailed mass budget was created totalling 13.3 kg for the entire

system by developing the design and having prototypes underway. The thermal performance of the radiator system was computed by creating a thermal resistance network and solving using an iterative scheme. A 28-panel design reached 1400 W for a combined system while keeping the spacecraft temperature below 50 °C, outperforming existing deployable radiator technology on the basis of heat per unit mass.

The radiator panels themselves are lightweight and effective, weighing 126 g with the ability to theoretically reject 61 W with the layers' base temperature at 300 K. Tapered and layered fins composed of highly conductive pyrolytic graphite sheets allow for improvements over previous designs, with a carbon fiber frame structurally supporting them. Two mathematical models perfectly bounded the finite element analyses, validating that an isothermal assumption of these thin radiators is correct even with insulating adhesive layers. By exploring the parameter space through finite element analyses, the dimensions were settled, aided by the realistic structural limitations of sourcing and assembling such a design. Implementation and improvements on this design could lead to savings of several kilograms for a high-power application, and could be combined with loop heat pipe technology for a lightweight passive thermal solution. As a static non-deployable radiator, this style of panel could also be used as an extension to a spacecraft structure such as those found on the Mars Science Laboratory cruise module.

## 5.2    Future Work

The proposed radiator architecture has been shown to theoretically deliver incredible thermal performance with significant mass savings. However, the technology is not currently ready for flight. Here, we outline what needs to be done in order to bring this technology to a future mission.

First and foremost, a designer should ascribe an example mission where this novel radiator system can outperform similar technologies. By having a mission selected, this design can be tailored to meet those specific requirements.

Subsystem tests and modifications that will need to be made:

- Add lightweight hinges that can improve the fundamental frequency of the system.

- Verify fluid system performance with bench tests and make changes to the fluid loop as required.

- Specify ideal heat transfer fluid for the given mission design with freeze tolerance in mind.

- Perform detailed design for the electrical system.

- Test burn wire design with deploying scroll mechanism.

- Test adhesion of thermal paint to PGS.

- Test Kapton HN to see if the designed tube will not crack under low-temperature and the double-90 strain conditions.

- Perform a thermal-vacuum test for a single radiator panel to verify mathematical models

With these changes made, there are several standard tests that should be completed in order to raise the system's overall technology readiness level before a launch.

(1) Build and test the stowed radiator design under launch vibration conditions.

(2) Complete a higher-fidelity integrated structural and fluid test of the full system and operation using a gravity-offsetting two-axis rail system.

(3) Perform a deployed, multi-panel thermal-vacuum test on the radiator system to validate mathematical models

As with any mission, it is critical to analyze the failure risk, probability, and severity for the different failure mechanisms of the system. Above, testing has been recommended to alleviate some of the uncertainty in the design. After developing the system, it seems like the major issues that could arise are a possible failure in the kinked tubes due to cracks from testing, a power outage freezing the fluid, and motor/pump failure.

Of these, the most critical issue is that the selected glycol-water fluid would not be able to handle a significant long-duration power failure. A realistic example could be if attitude control is lost, solar panels are not facing the sun and a fraction of nominal power can be generated. Below the mentioned threshold of 792 W, over enough time, the fluid system will reach equilibrium and freeze up. If the fluid freezes to a solid, it will expand into an ice-glycol slush [83], which could structurally damage pipes if there is not adequate volume to expand. Furthermore, blockage of flow would occur, and the spacecraft would no longer be effective at rejecting heat when it receives power again. If this freezing happens, the heat path would be reduced to conduction instead of the previous material flow, and this could cause overheating and damage a spacecraft. Regardless, this freezing might not be a concern might depending on the mission. For missions that would unlikely ever experience a complete power outage, failure could be mitigated by including wire heaters along the fluid loop. However, not all missions have the likelihood or ability to survive a power failure. Deep space missions with an MMRTG are always producing heat and converting that to electricity, and if that were to fail, the entire mission would be a complete loss even without a radiator issue. Further, other systems such as manned space stations can be repaired. It might be feasible to sacrifice one or more radiator assemblies to preserve the temperature in the rest. This could result in only a partial failure with a lower power state to wait in while the station gets repaired. Perhaps the alternative of simple single redundancy by including an extra insulated accumulator filled with fluid would be feasible to mitigate the situation. Finally and most reasonably, this issue could be eliminated by changing to either a two-phase ammonia-based fluid system, or a different lower temperature single-phase heat transfer fluid (HTF). Examples of heat transfer fluids seen in aerospace literature [24, 27] include Galden ZT85, Paratherm CR, and Novec 7000, all of which can be operated below -80 °C. However, the most promising HTF is Novec 7200, which has a freezing temperature of -138 °C while not being toxic or flammable [84]. This fluid could prevent the thermal blockage and expansion issues described above because it would allow extremely low temperatures to exist within the fluid loop without freezing. Since the fluid would still flow, this means the spacecraft would still have control over the heat rejection capabilities. The only disadvantage with

this material seems to be a significant reduction in specific heat compared to water-glycol. NASA Technology Roadmap 2015 even said that long term, it is looking to switch from dual loop (water and ammonia) technology to single loop (but not necessarily single-phase) technology (14.2.2.1 Heat Transport Fluid) [85], so these HTFs might be worth considering. Regardless of which fluid is selected, the analysis should consider how this change will affect the design's mass budget as well as thermal, and dynamic performance - weighing the decision against other alternatives.

Another significant improvement that could be made is optimizing the geometry of the radiator panels, now knowing the expected mass of the fluid loop system. Since the weight of the radiator panels themselves are a small fraction of the mass budget as seen in section 3.2.3, it might make sense to lengthen the optimal geometry, make the design thicker with more PGS layers, increase the temperature of the surface of the radiator, and reject more heat for the same spacecraft temperature. Primarily, the techniques taken here were an optimization of the panel geometry alone without the rest of the system included in the parasitic mass. If the desire is to improve heat rejection per unit mass, the entire system needs to be taken into account. Further, if pyrolytic graphite sheets can be sourced at larger dimensions, wider panels could be an easy method to reduce the number of hinges and improve the stiffness of the structure.

Further work would be required to tailor this system to a high-temperature, nuclear powered radiator solution. The use of indium foil as a thermal interface would not work above its melting point around 157 °C, so other material choices should be considered. As well, the kinked tube design might not function since temperatures above 400 °C are at the limits of Kapton HN, and material degradation could occur. For the rest of the design, the choice of epoxies to hold the structure together would also need to be reconsidered. Brazing the clamping tube bracket is an option, such as that seen from Denham in 1994 [86].

The technology readiness level of our proposed radiator architecture could likely be categorized around TRL 4-5. Aspects of this technology have been demonstrated in a relevant environment with a deployment prototype demonstrating the ability to release and extend into the radiating configuration. Other aspects, such as the fluid loop system, have already been flown, such as with

MSL and Parker Solar Probe missions. However, with changes proposed, testing still needs to verify the system's ability to perform as expected. While a realistic tapered and layered panel prototype was built, raising the TRL from 0 to TRL 4, it has not yet been operated in a thermal-vacuum experiment but it has also progressed past analytical demonstrations. Its performance has been predicted for further evaluations.

Overall, the goal of this project was to create a lightweight radiator system that is highly scalable for missions requiring high heat rejection requirements. Hopefully, this work has demonstrated that the proposed design could meet these objectives. Following through and making the suggested improvements and testing could result in 3x the performance, enabling humanity's next generation of spacecraft to explore the universe.

# Bibliography

[1] "Thermal Management for High Power SmallSats," Air Force SBIR Program, AF191-070, 2019. Accessed on: Aug. 2, 2021. [Online]. Available https://www.sbir.gov/node/1531891

[2] "Spacecraft Thermal Management," NASA SBIR Program, SBIR_20_P1 Z2.01, 2020. Accessed on: Aug. 2, 2021. [Online]. Available https://www.sbir.gov/node/1657687

[3] Marquis, K. B., Ployhar, K., and López Jiménez, F., "Development of a High-Power Deployable-Tube Radiator System," *50th International Conference on Environmental Systems*, 2021.

[4] Marquis, K. B., Ployhar, K., and López Jiménez, F., "Thermal Analysis of a Novel Lightweight Layered and Tapered Radiator Panel with Pumped-Fluid-Loop System," *50th International Conference on Environmental Systems*, 2021.

[5] Lécossais, A., Jacquemart, F., and Lefort, G., "Deployable Panel Radiator," *47th International Conference on Environmental Systems*, Charleston, SC, 2017.

[6] Ambrose, J., "Flex Heat Pipe East-West Deployable Radiator," *Microgravity Science and Technology*, Vol. 31, 2019, pp. 311-316.

[7] Murphey, T. W., et al. "High Strain Composites," *2nd AIAA Spacecraft Structures Conference*, Kissimmee, FL, 2015.

[8] Oren, J.A., and Harold R.H., "Space Station Heat Rejection Subsystem Radiator Assembly Design and Development," *SAE Transactions*, Vol. 104, 1995, pp. 1086–1095.

[9] Ding, T., Liu, C., Li, M., Miao, J., Guo, Y., and Bu, X., "Design and Experimental Study of Deployable Radiator Based on Loop Heat Pipes," *8th International Conference on Mechanical and Aerospace Engineering*, Prague, Czech Republic, 2017, pp. 286-291.

[10] PGS Graphite Sheets, Panasonic Thermal Solutions Catalog, 2020.

[11] PG1513 Technical Data Sheet, ProGraphite, Untergriesbach Germany, accessed March 7, 2021.

[12] Maas, A., "Development of Pyrolytic Graphite Applications in Spacecraft Thermal Control Systems," *47th International Conference on Environmental Systems*, Charleston, SC, 2017.

[13] van Lierop, C. A. B., "Deployable radiator wing for high performance CubeSats," Masters Thesis, Aerospace Engineering Dept., Delft Univ. of Technology, Delft, NL, 2021.

[14] Bergman, T. L., Lavine, A. S., Incropera ,F. P., "Fundamentals of Heat and Mass Transfer", 7th ed., Wiley, 2011.

[15] Haller, H. C., Wesling, G. C., and Lieblein, S., "Heat-Rejection and Weight Characteristics of Fin-Tube Space Radiators with Tapered Fins," NASA TN D-2168, Cleveland, OH, 1964.

[16] Ku, J., "Introduction to Heat Pipes," *Thermal & Fluids Analysis Workshop (TFAWS)*, NASA Goddard Space Flight Center, 2015.

[17] Evans, A., "Design and Testing of the CubeSat Form Factor Thermal Control Louvers," *33rd Annual AIAA/Utah State University Small Satellite Conference*, Logan, UT, 2019.

[18] Bertagne et al., "Coupled behavior of shape memory alloy-based morphing spacecraft radiators: experimental assessment and analysis," Smart Materials and Structures, 2018.

[19] Dudon J.P. et al., "Development of Variable Emissivity Coatings for Thermal Radiator," *50th International Conference on Environmental Systems*, 2021.

[20] Bugby, D.C., Rivera, J.G., Mauro, S.L., and Farmer, J.T., "Extended Stroke and Miniaturized Reverse-Operation DTE Thermal Switches," *50th International Conference on Environmental Systems*, 2021.

[21] Ercol, C., Abel, E., Holtzman, G., & Wallis, E., "Thermal Design Verification Testing of the Solar Array Cooling System for Parker Solar Probe," *48th International Conference on Environmental Systems*, Albuquerque, NM, 2018.

[22] Birur, C. G., "Thermal Control of MSL Rover 'Curiosity' using an Active Fluid Loop," *29th International Symposium on Space Technology and Science*, Nagoya, JP, 2013.

[23] "Active Thermal Control System (ATCS) Overview, " Boeing. accessed July 17, 2021.

[24] Benthem et al., "Development of a Mechanically Pumped Fluid Loop for 3-6 kW Payload Cooling," National Aerospace Laboratory (NLR), 2009.

[25] "State of the Art of Small Spacecraft Technology", Thermal Control, Chap. 7. Accessed on: Aug. 2, 2021. [Online]. Available https://www.nasa.gov/smallsat-institute/sst-soa-2020/thermal-control

[26] Maidanik, Y. F.,, "Loop heat pipes," Applied Thermal Engineering, 2004.

[27] Anderson, A. J., "The Active CryoCubeSat Project: Design and Status," *31st Annual AIAA/Utah State University Small Satellite Conference*, Logan, UT, 2017.

[28] Balandin, A. A. et al, "Superior Thermal Conductivity of Single-Layer Graphene," Nano Letters, Vol. 8, pp. 902-907, 2008.

[29] Norley, J., "125 Years of Carbon and Graphite Science – From Arc Carbons to Smart Phones," *GrafTech International*, 2012.

[30] Kraus, A. D., Aziz, A., and Welty, J., *Extended Surface Heat Transfer*, Wiley, 2001, Chap. 13, pp 572-633.

[31] Benthem, B., Airbus Defense and Space Netherlands B.V., Leiden NL, U.S. Patent Application for a "Radiator, as well as space vehicle structure comprising such radiator," US Patent 10,101,099, filed March 12, 2015.

[32] Clark, S., *NASA plans to launch first two Gateway elements on same rocket*, Spaceflight Now, May 6, 2020. Accessed on: Aug 2, 2021. [Online]. Available: https://spaceflightnow.com/2020/05/06/nasa-plans-to-launch-first-two-gateway-elements-on-same-rocket/

[33] Penn, J., et al., "GPM Solar Array Gravity Negated Deployment Testing," *42nd Aerospace Mechanisms Symposium*, Baltimore, MD, 2014.

[34] Freeland, R. H., "Deployable Antenna Structures Technologies", *Large Space Apertures Workshop*, Caltech, Pasedena, CA, 2008.

[35] Block, J., Straubel, M., and Wiedemann, M., "Ultralight Deployable Booms for Solar Sails and Other Large Gossamer Structures in Space," Acta Astronautica, 2010.

[36] Cox, R. L. and Leach, J. W., "Flexible Deployable-Retractable Space Radiators," *AIAA 1977-764. 12th Thermophysics Conference*, Albuquerque, NM, 1977.

[37] Yendler, B., "Thermal Management for High Power Cubesats," *34th Annual AIAA/Utah State University Small Satellite Conference*, 2020.

[38] Mauroschat A, and Blythe, P., "The @BUS Programme," ESTEC, 2006.

[39] Verdonck, J., et al., "Development and qualification of a Deployable Radiator in the frame of the European Horizon 2020 Pegasus program," *48th International Conference on Environmental Systems*, Albuquerque, NM, 2018.

[40] Goncharov, K., Orlov, A., Golovin, O., Perotto, V, and Tavera, S., "1500 W Deployable Radiator with Loop Heat Pipe," *IV Minsk International Seminar: Heat Pipes, Heat Pumps, Refrigerators*, Minsk, Belarus, 2000.

[41] Franck, R. A. et al., "High Performance Cryogenic Radiators for James Webb Space Telescope," *46th International Conference on Environmental Systems*, Vienna, Austria, 2016.

[42] Longhurst, G. R., Schnitzler, B. G., and Parks, B. T., "Multi-Megawatt Power System Trade Study", Idaho National Engineering and Environmental Laboratory, United States, 2001.

[43] "Prometheus Project Final Report." Jet Propulsion Laboratory, NASA Report 982-R120461, 2005.

[44] Siamidis, J., "Heat Rejection Concepts for Lunar Fission Surface Power Applications," AIAA–2006–4196, NASA/CR—2006-2143888, 2006.

[45] Ellis, D. L. and Mason, L. S., "Summary of the Manufacture, Testing and Model Validation of a Full-Scale Radiator for Fission Surface Power Applications," Proceedings of Nuclear and Emerging Technologies for Space, Albuquerque, NM, 2011.

[46] Mason, L. S. and Poston, D., "Fission Surface Power System Initial Concept Definition," NASA/TM—2010-216772, 2010.

[47] Tomboulian, B. N., "Lightweight, High-Temperature Radiator for In-Space Nuclear-Electric Power and Propulsion," Doctoral Dissertation, Mechanical and Industrial Engineering Dept., Univ. of Massachusetts Amherst, Amherst, MA, 2014.

[48] Thurn, A. et al., "A Nichrome Burn Wire Release Mechanism for CubeSats," *Proceedings of the 41st Aerospace Mechanisms Symposium*, Jet Propulsion Laboratory, 2012.

[49] Burn Wire in Use in Deployable Boom - Fulton 2017 Loadpath Roccor

Fulton, J., Jeon, S., and Murphey, T. W., "Flight Qualification Testing of a Meter-class CubeSat Deployable Boom," AIAA SciTech Forum, *4th AIAA Spacecraft Structures Conference*, Grapevine, TX, 2017.

[50] Dandino, C., "Loads and Dynamics TDT Micro Burn Wire Release Mechanism," Jet Propulsion Laboratory, Pasadena, CA, 2017.

[51] Oh, H. U, Jeon, S. H., and Kwon, S. C., "Structural Design and Analysis of 1U Standardized STEP Cube Lab for On-Orbit Verification of Fundamental Space Technologies," International Journal of Materials, Mechanics and Manufacturing, Vol. 2, No. 3, 2014.

[52] Birur, G., Bhandari, P., Prina, M., Bame, D., Yavrouian, A., and Plett, G., "Mechanically Pumped Fluid Loop Technologies for Thermal Control of Future Mars Rovers," *SAE Transactions*, Vol. 115, 2006.

[53] Yedamale, P., "Brushless DC (BLDC) Motor Fundamentals," Microchip Technology application note AN885, 2003.

[54] Yao, X, Zhao, J., Wang, J., Huang, S., Jiang, Y., "Commutation Torque Ripple Reduction for Brushless DC Motor Based on an Auxiliary Step-Up Circuit," IEEE Access, Vol. 7. pp. 138721-138731, 2019.

[55] Balcerzak, M. J. and Raynor, S., "Steady state temperature distribution and heat flow in prismatic bars with isothermal boundary conditions," International Journal of Heat and Mass Transfer, vol. 3, (2), pp. 113-125, 1961.

[56] Mass Properties Control for Space Systems, AIAA Standard S-120A-2015, 2015.

[57] Vacco Low Pressure Latch Valve Technical Datasheet. Accessed on: Aug. 2, 2021. [Online]. Available https://www.vacco.com/images/uploads/pdfs/latch_valves_low_pressure.pdf

[58] GP50 Compact Flight Heritage Transducer Model 7202 Datasheet. Accessed on: Aug. 2, 2021. [Online]. Available https://www.gp50.com/wp-content/uploads/2018/06/A5SL-074_7202_7200-8494cc_RwB.pdf

[59] TE Precision Pressure & Temperature Transmitter AST20PT Datasheet. Accessed on: Aug. 2, 2021. [Online]. Available here

[60] Hyers, R. W., Tomboulian, B. N., Crave, P. D., and Rogers, J. R., "Lightweight High-Temp Radiator for Space Propulsion," Advanced Space Propulsion Workshop, Huntsville, AL, 2012.

[61] Lashley, C., Krein, S., and Barcomb, P., "Deployable Radiators - A Multi-Discipline Approach," *28th International Conference on Environmental Systems*, Danvers, MA, 1998.

[62] Howell, H. R. and Williams, J. L., "Qualification of the Space Shuttle Orbiter Radiator System", *Society of Automotive Engineers*, Dallas, TX, 1983.

[63] Ercol, C. J. and Holtzman, G. A., "Early Mission Thermal Performance of Parker Solar Probe through Orbit Four" *47th International Conference on Environmental Systems*, 2020.

[64] Fixsen, D. J., "The Temperature of the Cosmic Microwave Background," *The Astrophysical Journal*, vol. 707, pp. 916-920, 2009.

[65] Schmidt, P. B., "An Investigation of Space Suit Mobility with Applications," Doctoral Dissertation, Dept. of Aeronautics and Astronautics, Massachusetts Institute of Technology, Cambridge, MA, 2014.

[66] Guo, J., Wang, C., Zhang, J., and Tao, Q., "Kinking Characteristics of an Inflated Beam under Bending," Journal of Spacecraft and Rockets, Vol. 57, No. 3, May 2020.

[67] Sharma, A. H., Rose, TJ, Seamone, A., Murphey, T. W., and López Jiménez, F., "Analysis of the Column Bending Test for Large Curvature Bending of High Strain Composites," *AIAA Scitech Forum*, San Diego, CA, 2019.

[68] Main, J. A., Peterson, S. W., and Strauss, A. M., "Load-Deflection Behavior of Space-Based Inflatable Fabric Beams," Journal of Aerospace Engineering, vol. 7, (2), pp. 225-238, 1994.

[69] Harris C. M. and Piersol, A. G., *Harris' Shock and Vibration Handbook*, 5th ed., McGraw-Hill, 2002, Chap. 7, pp 7.11-7.15.

[70] NASA Space Flight System Design and Environmental Test, NASA AMES Technical Standard, std8070.1, 2018.

[71] "Spaceflight Mission Planning Guide", Spaceflight Inc., Feb. 2019. Accessed on: Aug. 2, 2021. [Online]. Available: https://spaceflight.com/wp-content/uploads/2019/02/Spaceflight-Mission-Planning-Guide-Rev-G.pdf

[72] Chamberlain, M. K., Kiefer, S. H., and Banik, J. A., "On-Orbit Structural Dynamics of the Roll-Out Solar Array", *2018 AIAA Spacecraft Structures Conference*, Kissimmee, FL, 2018.

[73] Winslow, C., Bilger, K., and Baraona, C., "Space Station Freedom solar array design development," *Proceedings of the 24th Intersociety Energy Conversion Engineering Conference*, Washington DC, 1989.

[74] Hedgepeth, J. M., "Efficient Structures for Geosynchronous-Spacecraft Solar Arrays," NASA Lewis Research Center, *Space Photovoltaic Research and Technology*, pages 363–377, Carpinteria, CA, 1980.

[75] Prepublished material from Yasara Dharmadasa, July 2021, used with permission.

[76] Jeong, J. W. et al., "A novel tape spring hinge mechanism for quasi-static deployment of a satellite deployable using shape memory alloy," Review of Scientific Instruments, vol. 85, (2), pp. 025001-025001, 2014.

[77] Public Domain Source: "S135E011027 - STS-135 - Flyaround View of the P1 HRS Radiators and MRM1", U.S. National Archives & DVIDS. Accessed on: Aug. 2, 2021. [Online]. Available https://nara.getarchive.net/media/s135e011027-sts-135-flyaround-view-of-the-p1-hrs-radiators-and-mrm1-25c610

[78] Jeong, J. W., Yooa, Y. I., Leea, J. J., Limb, J. H., and Kim, K. W., "Development of a Tape Spring Hinge with a SMA Latch for a Satellite Solar Array Deployment Using the Independence Axiom," IERI Procedia, vol. 1, pp. 225-231, 2012.

[79] Dharmadasa B. Y. et al, "Formation of Plastic Creases in Thin Polyimide Films," Journal of Applied Mechanics, vol. 87, (5), 2020.

[80] Sharma, A. H., Hill, S., Perez, R., Rose, TJ, and López Jiménez, F., "Tensile Fiber Failure on High Strain Composites," *AIAA SciTech Forum*, Orlando, FL, 2020.

[81] Corona, E., Lee, L. H., and Kyriakides, S., "Yield anisotropy effects on buckling of circular tubes under bending," International Journal of Solids and Structures, vol. 43, (22), pp. 7099-7118, 2006.

[82] "409-xxx Rev NC 0.24 Flat Carbon Composite Plate Testing Results", Center for Advanced Mineral and Materials Processing, prepared for Rockwest Composites, 2016. Accessed on: Aug. 2, 2021. [Online]. Available https://www.rockwestcomposites.com/media/downloads/409-xxx-Rev-NC-Final-Report.pdf

[83] "GLYCOL 101 - Difference between burst protection and freeze protection", NOCO Innovative Industrial Solutions, May 26, 2020. Accessed on: Aug. 2, 2021. [Online]. Available https://www.glycolblender.com/resources/glycol-101-difference-between-burst-protection-and-freeze-protection

[84] 3M Novec 7200 Engineered Fluid Datasheet. Accessed on: Aug. 2, 2021. [Online]. Available https://multimedia.3m.com/mws/media/199819O/3m-novec-7200-engineered-fluid-en.pdf

[85] NASA Technology Roadmaps TA 14: Thermal Management Systems, July 2015. Accessed on: Aug. 2, 2021. [Online]. Available https://www.nasa.gov/sites/default/files/atoms/files/2015_nasa_technology_roadmaps_ta_14_thermal_management_final.pdf

[86] Denham, H.B., Koester, J.K., Clarke, W., and A.J. Juhasz, "NASA Advanced Radiator C-C Fin Development," *American Institute of Physics Conference Proceedings*, 301, pp. 1119-1127, 1994.

## Appendix  A

## 3D-PDF Radiator Model and System Model

Two 3D-PDF models are included in the space below: one for the novel radiator architecture and another for the panel design. To open the model and allow zooming in, panning, and rotation, open the PDF using Adobe Reader or Acrobat, enable 3D and multimedia content, and click in the multimedia region.
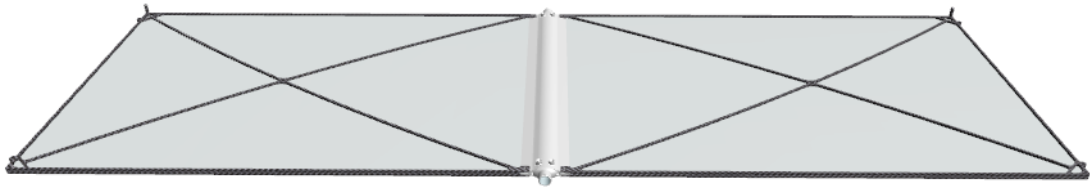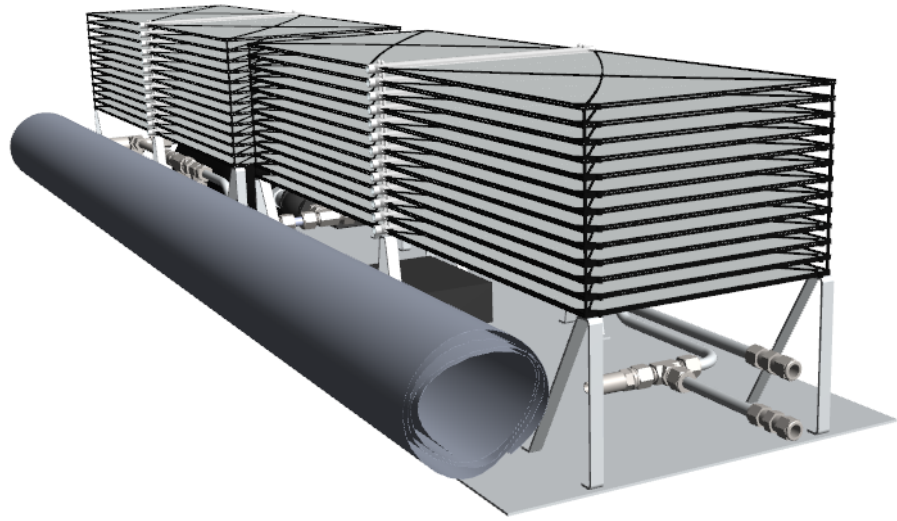
# Appendix B

# Data Archive

The code and data used for the triangular anisotropic radiator comparison is archived for open source use here. DOI 10.5281/zenodo.4686468

The code (including parameters) used for the pumped-fluid-loop analysis is archived for open source use here. DOI 10.5281/zenodo.5155424

The code and data for finding bending moment from different tube geometries is archived for open source use here. DOI 10.5281/zenodo.5155072

The code for the lumped element rigid panel dynamics model is archived for open source use here. DOI 10.5281/zenodo.5154930

The 3D models shown in this work are included and are archived for open source use here. DOI 10.5281/zenodo.5155046

Videos of the deployment model are saved and can be viewed if links break in the future, through open source use here. DOI 10.5281/zenodo.5155087

# Appendix C

# Initial Sketches of the Deployment Concepts

These sketches were created by Kayla Ployhar during the design process of developing a release mechanism.



Figure C.1: Sketch of original arm mechanism

Figure C.2: Sketch of diagonal latch mechanism



Figure C.3: Sketch of vertical latch mechanism
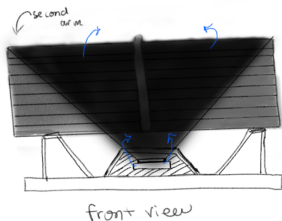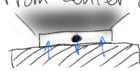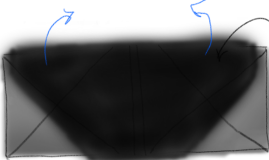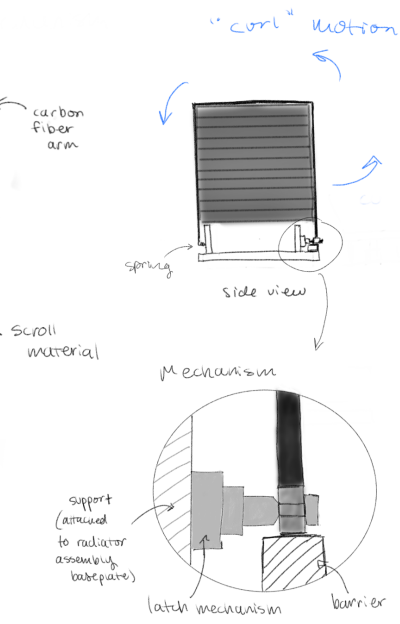
Figure C.4: Sketch of scroll release mechanism

# Appendix D

# Stacked Panel Calculations

A preliminary calculation was done to determine the potential forces on the stacked panel design under launch vibration conditions. This analysis assumed all the panels would be rigid in a single stack and provide reaction forces at the ends where locating pins keep panels together when compressed. As well, quasi-static loads are assumed to act on the system, which isn't realistic but is done anyways for this initial analysis. A free body diagram of this is shown below for the worst-case situation where gravity and accelerations exert a moment, reducing the required compression on the panels on one end.
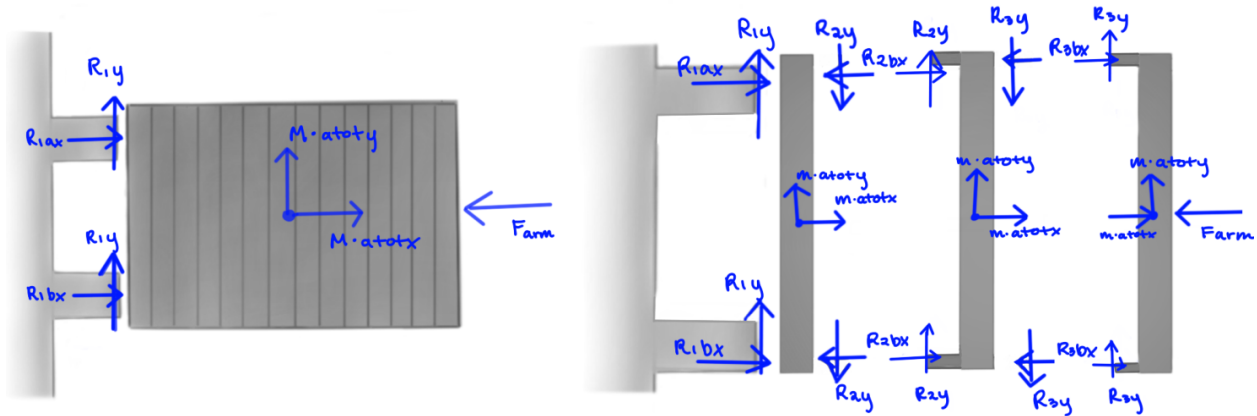


Figure D.1: Free body diagram on a simplified rigid 3-panel system

The lateral and axial g forces experienced on a falcon 9 were used for this work[1] , seen in Figure D.2, and the expected accelerations were found. The calculations below show the forces on

---

[1] Falcon Users Guide, SpaceX, April 2020. Accessed on: Aug. 2, 2021. [Online]. Available https://www.spacex.com/media/falcon_users_guide_042020.pdf

each of the panels, as well as the parameters used.
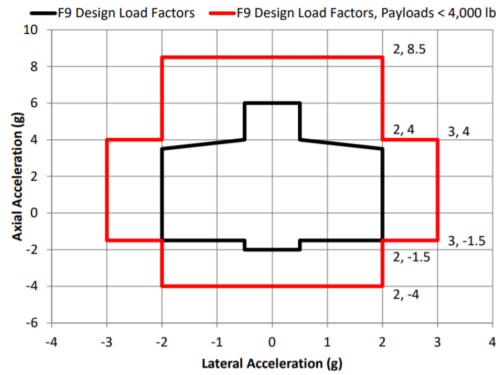


Figure D.2: Falcon 9 Acceleration Load Factors

Taking the sum of forces and moments on the panels led to the equations and results below in Figures D.3 and D.4.

| Knowns | | | Unknowns | | | |
|---|---|---|---|---|---|---|
| Variable | Value | units | Variable | Value | units | Equation |
| Farm_tot/2 | 126 | N | R1y | 163.7 | N | M*(1/2)*(-atoty) |
| m | 0.126 | kg | R1ax | 0.3 | N | R1bx - 2R1y*(L/h) |
| M | 3.51 | kg | R1bx | 182.8 | N | R1y*(L/h) + Farm - (M/2)*atotx |
| a_rx (multiplier) | 2 | | R2y | 157.9 | N | R1y + (m/2)*atoty |
| a_ry (multiplier) | 8.5 | | R2ax | 7.9 | N | R1ax + R1bx - R2bx + m*totx |
| # Panels | 28 | | R2bx | 177.6 | N | R1bx - 2*R2y*(w/h) + (1/2)*m*atotx + (w/2h)*m*atoty |
| g | 9.81 | m/s^2 | R3y | 152.0 | N | R2y + (m/2)*atoty |
| h | 0.201 | m | R3ax | 15.3 | N | R2ax + R2bx - R3bx + m*atotx |
| l | 0.112 | m | R3bx | 172.7 | N | -2R3y(w/h) + m*atoty(w/(2h)) + m*atotx(1/2) + R2bx |
| w | 0.004 | m | R(n+1)y= R(n)y+(m/2)*atoty | | | |
| a_total_x | 19.6 | m/s^2 | R(n+1)ax = R(n)ax+ R(n)bx - R(n+1)bx +m*atotx | | | |
| a_total_y | -93.2 | m/s^2 | R(n+1)bx = R(n)bx-2*R(n+1)y(w/h)+m*atotx(1/2)+m*atoty(w/(2h)) | | | |
| deg_arx | 0 | deg | | | | |
| deg_grav | 270 | deg | **Based on 28 Panels (Final)** | | | |
| deg_ary | 270 | deg | Test Case: | | Minimum Farm needed | |
| Farm_tot | 252 | N | a_rx = **2**, a_ry = **8.5** | | 252 N | |

Figure D.3: Knowns, unknowns, and calculations for reaction forces

| Panel # | Rny | Rnax | Rnbx |
|---|---|---|---|
| 1 | 163.7 | 0.3 | 182.8 |
| 2 | 157.9 | 7.9 | 177.6 |
| 3 | 152.0 | 15.3 | 172.7 |
| 4 | 146.2 | 22.5 | 168.0 |
| 5 | 140.4 | 29.4 | 163.5 |
| 6 | 134.5 | 36.1 | 159.2 |
| 7 | 128.7 | 42.6 | 155.2 |
| 8 | 122.8 | 48.8 | 151.5 |
| 9 | 117.0 | 54.8 | 147.9 |
| 10 | 111.1 | 60.6 | 144.6 |
| 11 | 105.3 | 66.1 | 141.5 |
| 12 | 99.4 | 71.4 | 138.7 |
| 13 | 93.6 | 76.5 | 136.1 |
| 14 | 87.7 | 81.3 | 133.7 |
| 15 | 81.9 | 86.0 | 131.6 |
| 16 | 76.0 | 90.3 | 129.7 |
| 17 | 70.2 | 94.5 | 128.0 |
| 18 | 64.3 | 98.4 | 126.5 |
| 19 | 58.5 | 102.1 | 125.3 |
| 20 | 52.6 | 105.5 | 124.3 |
| 21 | 46.8 | 108.7 | 123.6 |
| 22 | 40.9 | 111.7 | 123.1 |
| 23 | 35.1 | 114.4 | 122.8 |
| 24 | 29.2 | 116.9 | 122.8 |
| 25 | 23.4 | 119.2 | 122.9 |
| 26 | 17.5 | 121.3 | 123.4 |
| 27 | 11.7 | 123.1 | 124.0 |
| 28 | 5.8 | 124.7 | 124.9 |

Check Farm that is large enough that Rnax is still positive

Figure D.4: Free body diagram on a simplified rigid 3-panel system

The force required to hold down the set of 28 panels without panels separating was found to be 252 N, which is within reasonable limits, roughly 26 kgf. In the current design, panels would be in two stacks instead of one and this should reduce the effect of bending moment pulling the panels apart. Consequently, a Mylar scroll sheet cover would be easily able to constrain these panels and prevent motion. Assuming a 0.5 m long section of 5 mil thick Mylar, and assuming all the force gets transmitted to this area and is distributed evenly, the stress on the sheet comes out at 2 MPa,

well below Mylar's tensile strength, around 200 MPa.

$$\sigma = \frac{F}{A} = \frac{252N}{(2 * 0.5m \cdot (0.000127m)} = 1.98 MPa$$

## Appendix  E

## Fluid Volume Calculations

Fluid volume calculations were performed to find the amount of fluid necessary to fill the radiators. Gas pressure was calculated to be 20 bar such that after releasing fluid into the panels, the system's static pressure would be at 2 bar. This was done assuming free expansion of the pressurized gas into the evacuated space left in the tank after the latch valve allows fluid to flow through the radiators.

Checks to make sure the tank can hold enough fluid were validated, which can be seen in Figure E.1 below.

**Fluid Volume Calculations**

**Inputs**

| | | |
|---|---|---|
| Num Radiators | 28 | |
| Tube Length between Radiators | 0.06 | m |
| Volume fluid margin (leftover) | 0.00014748 | m^3 (10 % tank) |
| Initial Air pressure P1 | 2000000.00 | Pa = N/m^2 (20.0 bar) |

**Static Variables**

| | | |
|---|---|---|
| Length of radiator | 0.204 | m |
| Pressure max Tank | 31026000 | pa |
| Vtank - 90 CI Tank | 0.001475 | m^3 |
| V tank-to-valve | 0.000014 | m^3 |
| gamma (ratio of specific heats for gas) | 1.00 | (Free Expansion) |

$$P_0 V_0^\gamma = PV^\gamma = \text{constant.}$$

| | | |
|---|---|---|
| V fluid initial = V vacuum + margin + V tank-valve | 0.00133 | m^3 |
| V fluid in tank = V fluid initial - V tank-to-valve | 0.00132 | m^3 |
| V inital air = Vtank - V fluid in tank | 0.00016 | m^3 |
| V2 = Vinitial air + V vacuum | 0.00133 | m^3 |
| V1 = Vtank - Vinitial Fluid | 0.00014 | m^3 |
| P2 = P1*(V1/V2)^gamma | 216282 | Pa = N/m^2 (216 kPa) |

**Volume of Vacuum Section**

| Name | Cross Section Area (m^2) | Length (m) | Total |
|---|---|---|---|
| Heat Input Section | 0.0000713 | 3.20 | 0.000228 |
| To and from center of spacecraft | 0.0000713 | 2 | 0.000143 |
| Radiators | | 5.712 | 0.000317 |
| Between radiators | 0.0000212 | 1.68 | 0.000036 |
| Post Radiator Length | 0.0000713 | 0.28 | 0.000020 |
| 1st check valve to pump | 0.0000713 | 0.19 | 0.000014 |
| 1st check valve to pump (redundant) | 0.0000713 | 0.23 | 0.000017 |
| pump | 0.0002835 | 0.04 | 0.000010 |
| pump (redundant) | 0.0002835 | 0.04 | 0.000010 |
| pump to final check valve | 0.0000727 | 0.32 | 0.000024 |
| Return from Radiators | | 7.39 | 0.00035243 |
| **Total volume of Vacuum Region:** | | | **0.001170** |
| | | | m^3 |

**Checks**

| | |
|---|---|
| Is volume inital fluid smaller than tank | TRUE |
| Is volume of fluid enough to fill the entire system | TRUE |
| (V_to Fill Tubes < V_Fluid Initial < V_tank) | TRUE |
| Pressure < Max Pressure in Tank | TRUE |

Figure E.1: Fluid Volume Calculations

# Appendix F

# Detailed Parameters of the Pumped-fluid-loop Analysis

Below is a non-exhaustive list of the parameters used in the thermal analysis for the pumped-fluid-loop design mentioned above. These items drive the derived parameters such as thermal resistances used in the iterative solver.

Table F.1:  Detailed Parameters of the Pumped-fluid-loop Analysis

| System Parameters | Value | Units |
|---|---|---|
| Flow Rate | 1.25E-05 | m$^3$/s |
| Heat Input | 1400.4 | W |
| Number of Radiator Panels (brackets) | 28 | |
| **Radiator Layers - double sided (4 symmetric quadrants)** | | |
| Number of radiator layers | 6 | |
| Radiator stepped-layer distance | 50.0 | mm |
| Thickness of PGS | 25 | $\mu$m |
| Thermal conductivity of PGS in-plane | 1500 | W/(m· K) |
| Length of contact region | 6.09 | mm |
| Thickness of adhesive layers | 10 | $\mu$m |
| Thermal conductivity of adhesive layers (out-of-plane conductivity) | 0.200 | W/(m· K) |
| Panel emissivity | 0.89 | |
| **Spacecraft/Cold Plate/Tubes** | | |
| Spacecraft plate thickness | 5.00 | mm |
| Spacecraft plate thermal conductivity | 236 | W/(m· K) |
| Spacecraft plate area | 0.0400 | m$^2$ |
| Length of cold plate tubes (half switchback) | 200 | mm |
| Number of cold plate lines (half-switchback) | 16 | |
| Outer diameter for inlet/outlet tubes | 4.76 | mm |
| Thickness of tube | 0.50 | mm |
| Thermal conductivity of tube | 14.4 | W/(m· K) |
| Length of tube beginning section | 0.400 | m |
| Length of tube end section | 1.000 | m |
| **Fluid Parameters - Hot Case - water-glycol 52 % by volume glycol, 20 °C average temp.** | | |
| Specific Heat | 3260 | J/(kg· K) |
| Density | 1082 | kg/m$^3$ |
| Dynamic Viscosity | 0.00487 | N· s/m$^2$ |
| Thermal Conductivity | 0.402 | W/(m· K) |
| **Bracket Section** | | |
| Length of bracket for convection/radiation | 200 | mm |
| Thermal conductivity of bracket | 200 | W/(m· K) |
| Thickness of bracket end section | 1.20 | mm |
| Length of bracket arm section | 4.60 | mm |
| Perimeter of bracket fluid cross section | 29.1 | mm |
| Area of bracket fluid cross section | 5.65E-05 | m$^2$ |
| Length of fluid tube after each bracket | 60.0 | mm |
| **Derived Non-Dimensional Parameters** | | |
| Prandtl's number | 39.49 | |
| Reynold's number within tube | 4.15 | |
| Graetz number within tube | 6.98 | |
| Nusselt number within tube | 15.02 | |
| Reynold's number within bracket | 3.82 | |
| Graetz number within bracket | 5.87 | |
| Nusselt number within bracket | 14.03 | |

# Appendix  G

# Post-Buckling Literature Review

A review of the literature was completed for independent study course credit.

Note that the pagination and references here are seperate from the main document.

# Tube Kinking and the Research into Post-Buckling - a Literature Review

Kyle Marquis
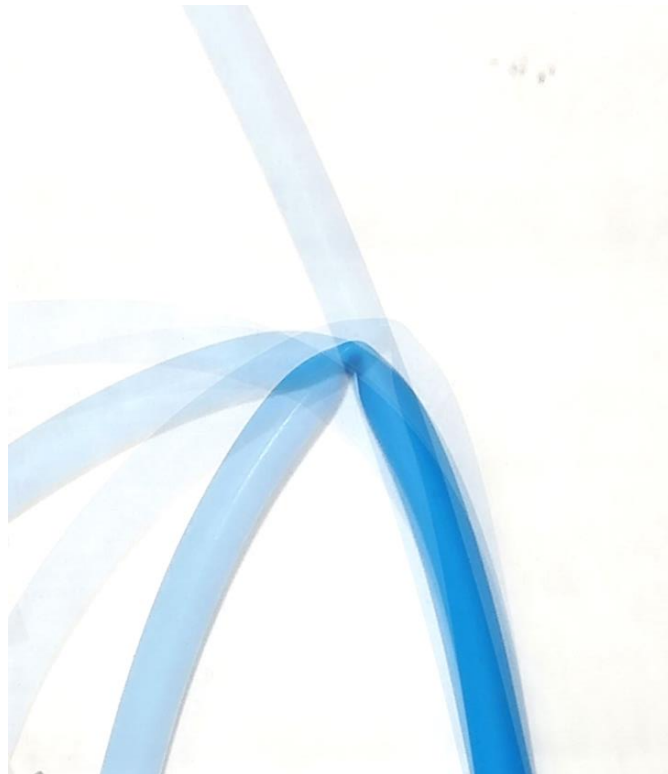
Cover Image by Kyle Marquis

# Table of Contents

# Introduction

Tube buckling is a mechanical phenomenon that happens when a cylindrical structure undergoes a shape change due to high loads, either compression forces, or in this case, bending moments. Aspects of this area have been well documented and researched, and there are many papers characterizing the onset of buckling

In my research, however, the onset of buckling itself is not my direct interest, and much of this review will focus on the stresses, strains, and geometry while kinking a tube. Here, I will also refer to this phenomenon, and the associated regime of bending, as post-buckling as used in the academic community.

The purpose of this study is to find out what's been done so far to characterize the effects of large deformations on a kinked tube. By knowing if and when a tube will break, or become overly plastified, weakening the structure, this can help researchers to understand how to design tubes that can fold and unfold. By folding thin tubes, they can be stored compactly which could enable a lightweight and small-footprint system that could be used in spacecraft.

# Methods

A search of the literature was conducted with the help of Dr. Francisco Lopez-Jimenez. The search terms were not exhaustive but included different permutations of

- Shells
- Tubes
- Thin shells
- Thin tubes
- Plasticity
- Bending
- Buckling
- Post buckling
- Large deformation
- Large strain
- Collapse

Furthermore, the references given from the results of these searches helped locate other authors and work in the field.

# Onset of Buckling

Within the broader scope of what we shall call buckling, much of the interest, and consequently research, lies within the domain of the onset of buckling. In many engineering applications, parts are designed to survive under expected loadings and fail under more extreme loads. Failure is often considered the stress that initial buckling occurs. For example, a person riding a bicycle might consider a collapsed frame a "failure" if their frame was to deform and bend out of position. Take another example as the offshore pipeline industry (where some of the authors included in this review have contributed research to and even textbooks on). Buckling, in this case, could cause rupture and leakages, so designers care about the point of initial deformity from expected values. This gives a conservative value of design stress for which engineers take care to avoid.



**Fig 1: Buckled bicycle frame. Source:**
https://construct.typepad.com/25seven/2009/01/engineering-buckling-limit-of-frame-tubing.html#more

Some of the phenomena associated with buckling, touched on by the authors within this review, include
- Ovalization of the tube cross-section
- Various modes of collapse
- Wrinkling features at the surface

As with any academic field, the current day research relies heavily on the work from previous decades, and even centuries. Buckling studies originate from Leonhard Euler in 1757 (no original source could be located), but work on thin wall sections started to appear later in the 1900s.

One of the earlier works frequently cited pertains to research by Brazier from 1927 where a relationship to bending and tube cross-section ovalization was developed [1].

A common mode of collapse, forming a diamond-patterned surface, was researched from Tyvergaard 1983 [2].

Analysis by Axelrad in 1985 looked at how the stress state and shape of the deformed shell directly affect buckling stability [3].

Weingarten, publishing with NASA, gave experimental relations in 1965 for thin-walled cylinders, which led to a knockdown factor for bending and axial loads [4].

Further research from Kyriakides and Ju at the University of Texas at Austin proceeded to characterize the formation of wrinkles, localization, and failure in 1991 using the test setup below [5].
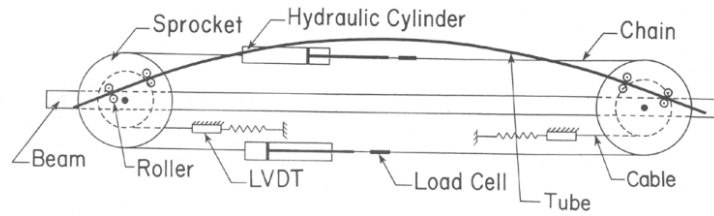


**Fig 2: Tube bending test setup reprinted from the work of Kyriakides and Ju [5].**

Work from  Houliara in 2006 evaluated "the stability of initially-ovalized thin elastic tubes subjected to combined pressure and bending" [6]. Notably, they provide some of the only equations for longitudinal stress as well as deformed hoop curvature as a function of overall curvature and pressure.

$$\frac{\sigma_x(\theta)}{\sigma_e} = -\zeta_0 \frac{\kappa - 2f\kappa - f\kappa_{in}}{4(1-f)}(3\sin\theta - \sin 3\theta)$$
$$+\kappa\left[\left(1 - \frac{3(\kappa+\kappa_{in})^2}{4(1-f)}\right)\sin\theta + \frac{(\kappa+\kappa_{in})^2}{4(1-f)}\sin 3\theta\right],$$
$$(43)$$

$$\frac{1}{r_\theta(\theta)} = \frac{1}{r} + \frac{3\zeta_0(1-2f)}{r(1-f)}\cos 2\theta + \frac{3\kappa(\kappa+\kappa_{in})}{r(1-f)}\cos 2\theta. \quad (44)$$

**Fig 3: Equations of longitudinal stress and hoop curvature as a function of overall curvature and pressure reprinted from the work of Houliara and Karamanos [6].**

Imperfections and their effects on steel thin-walled cylinders are investigated by Yadav, in 2018. One of their plots is found below in figure 4.
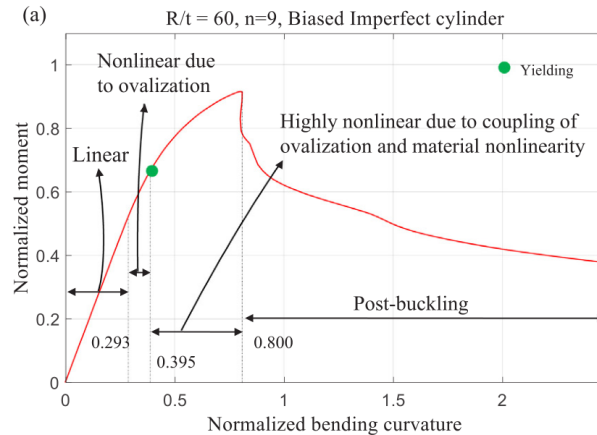
**Fig 4: Normalized plot of moment vs bending curvature for an imperfect steel cylinder reprinted from the work of Yadav and Gerasimidis [7].**

Many other works go into detail on the collapse of these thin tube structures, including but not limited to the authors below:

- Bai in 1993 [8]
- Elchalakani in 2002 [9]
- Mathon in 2006 [10]
- Coman in 2017 [11]

# Kinking of Thin Tubes

Very little research has been done to characterize the state of the material after buckling has already occurred, but this is my primary focus. In this section, the few papers that review parts of the post-buckling regime are investigated. Ideally, there would be simple equations describing the stress, strain, relating them to displacement, pressure, and moment for a kinked hose in a configuration such as in Figure 2. However, this topic is highly complex and often relies on simulations and experiments to find results.



**Fig 5: Kinked Hose - an example of a tube in the post-buckling state. Source: Kyle Marquis**

**Bending and symmetric pinching of pressurized tubes - Fay and Steele, 2000**

The work of Fay and Steele looked at force and angle of displacement curves while bending thin tubes [12]. In this article, they develop a relationship between forces and moments from their testing machine, translating the forces into an effective moment at the kink. Their sample setup is shown in figure 6, and their plot for non-dimensionalized moment vs bend angle is shown in figure 7. They also looked at the force required to indent the tube, but this will not be covered in this review.
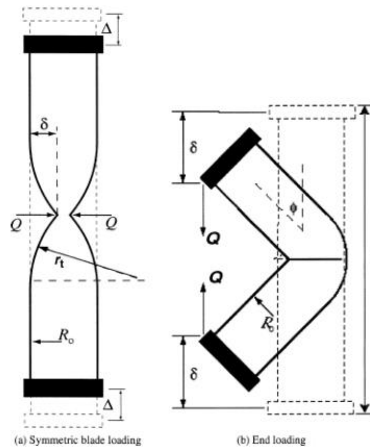
**Fig 6: Tube Experiment Diagram. Left is under blade loading, Right is under bending loading. Reprinted from the work of Fay and Steele [12]**
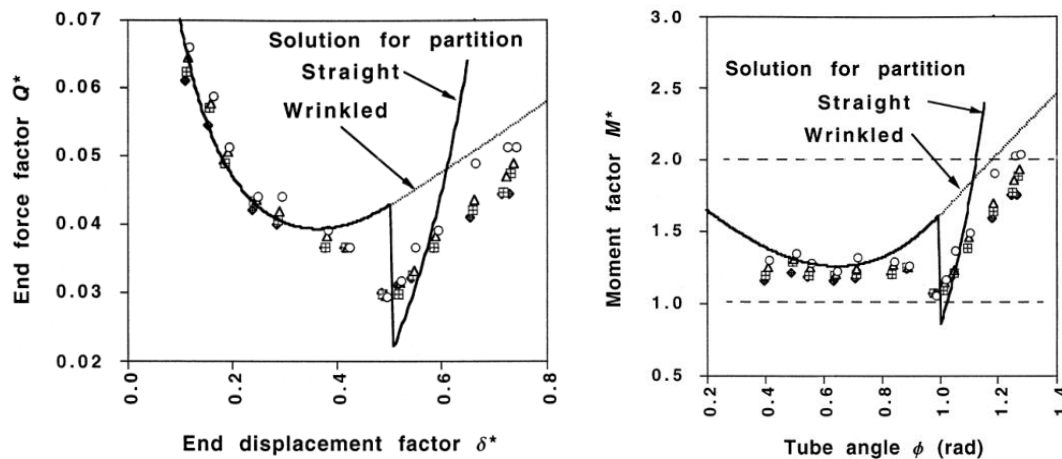


**Fig 7: Normalized force-displacement and moment-angle plots. Reprinted from the work of Fay and Steele [12]**

Their work extends to account even for different pressures, as their setup had pressures within the tubes during testing. This plot seen in figure 7 includes shows the effects of varying the pressure from 4905 Pa to 11,000 Pa. [905 (circles), 6900 (triangles), 8800 (squares), and11000 (rotated squares)]. Consequently the relative effect of pressure is observed by the authors to not make a significant difference on the result.

The rest of their work goes on to describe the mathematics of their analytical solutions, using an approach of total potential energy with modified terms. In this, they are assuming the material to be inextensional due to the thin nature of the shell.

Main Takeaways:
- This work ignores any effect of plasticity, or even elasticity, by considering a very thin shell of a high elastic modulus material. In their own words: "The main assumption is that all the work done by the applied loads goes into changing the volume and not into stretching and bending the wall of the tube. Generally, this is valid for a high modulus material with a sufficiently high internal pressure, but not for a rubber balloon."
- The relative change in pressures investigated showed very little effect on the moment required to displace the tube. However, it follows rationally that very small pressures would only have a small effect on the moment required to deform the tube. This work does not elaborate on how a larger pressure difference, such as say 10 bar (1,000,000 Pa) might affect the results.
- The authors were effective in comparing theory to experiment and show how the results of their work don't match experiment at larger angles, such as past $\phi = 1$ radian.

**Mechanics of highly deformed elastic shells - Vaziri, 2009**

Vaziri used numerical simulations in ABAQUS to model the bending of thin tubes [13], mentored by and following some of the work of Hutchinson [14]. In their work, they also plotted moment vs angle and included different ovalized cross-sections. In Figure 8 below, the effect of changing the eccentricity of the oval is seen in the moment required to change the angle. As the author describes, a more circular section loses a larger fraction of the load-carrying ability, as opposed to an already ovalized section which drops only a small percent when critical curvature happens.
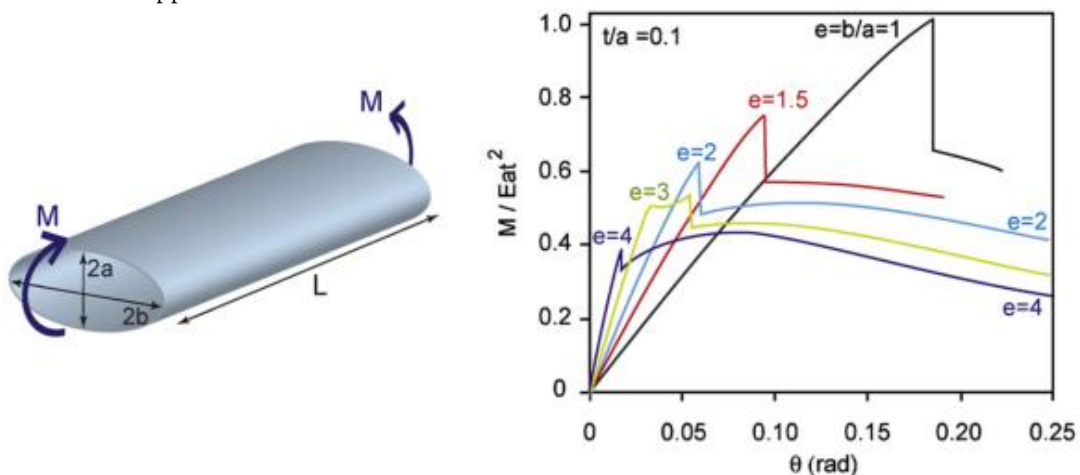


**Fig 8: Left: diagram of their tube geometry. Right: Normalized plot of moment vs angle. Reprinted from the work of Vaziri [13].**

The author uses these simulation tools to look at the post-buckling moment of different eccentricity cases, but the angle only goes up to 14 degrees of rotation. Interestingly, their simulations highlight the regions of maximum curvature of a kink, on the left side of figure 9 below.
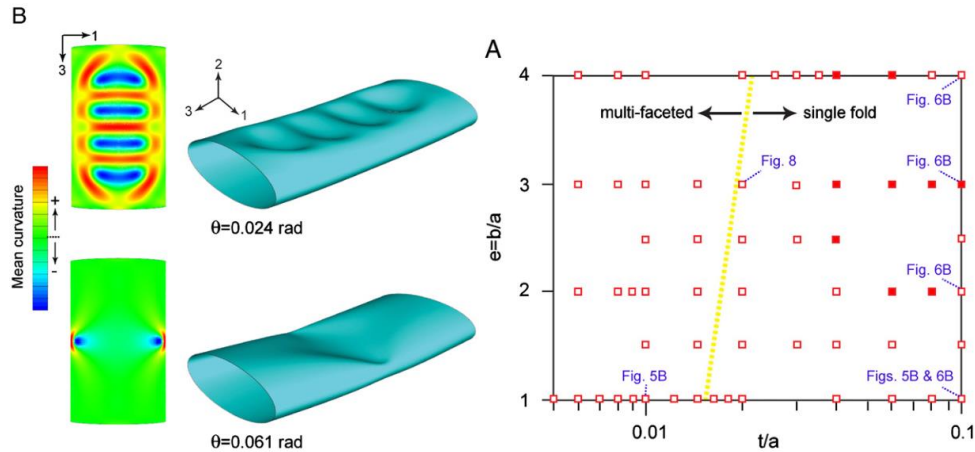


**Fig 9: Left: plot of relative curvature from simulation. Right: plot of eccentricity and ratio of thickness to length of minor axis for experiments completed, and method of collapse. Reprinted from the work of Vaziri [13].**

Their work also shows some of the various methods of collapse, as it relates to the relationship of thickness to radius for cylinders as in figure 10. For ellipses, they plot the space for modes of collapse in the right image of figure 9.
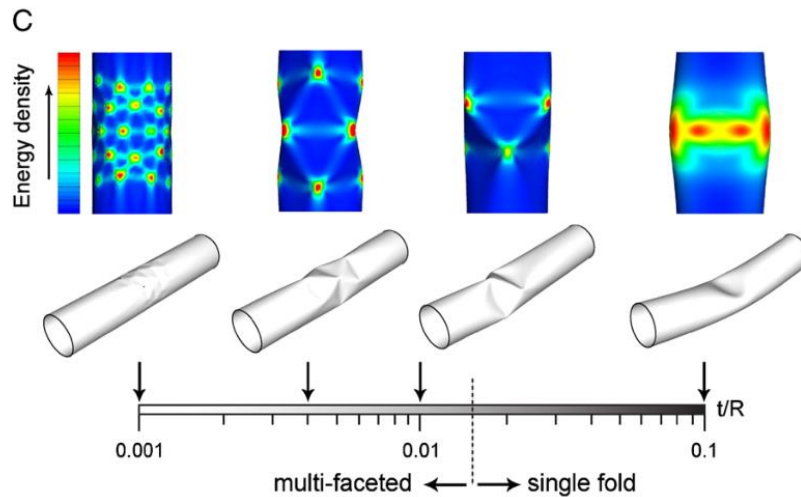


**Fig 10: Various modes of collapse based on thickness to radius ratio. Reprinted from the work of Vaziri [13].**

Main Takeaways:

- Numerical Simulations can be used to model the bending of these thin tubes. However, no information is given as to how these simulations were created, other than specifying in the abstract that the software ABAQUS is used.
- This analysis did not compare FEA to experiments, and no mention as to how accurate these results are, casting some doubt as to the results.
- Ovalization and then bifurcation causes a significant drop in the moment, particularly in proportion to the initial circularity of the tube.
- The work gives a good indication as to when to expect different modes of collapse and what their visualizations look like.
- Plasticity was not discussed in this paper, and it appears the simulations did not take this nonlinearity into account.

**Yield Anisotropy Effects – Corona, Lee, and Kyriakides, 2006**

Corona investigated the effects of anisotropy in the plasticity model for bending thin circular tubes [15], building upon the work from Ju and Kyriakides[5], explaining how a discrepancy in the earlier data might be explained from anisotropic effects in the aluminum tubes that were being tested.

From the earlier work by Kyriakides, they found that axial wrinkling happens when the ratio of diameter to thickness is high, agreeing with the simulations of Vaziri above. After further bending, the wrinkles then localize into a single kink, which can be seen from the newer results of Corona in figure 10 below.
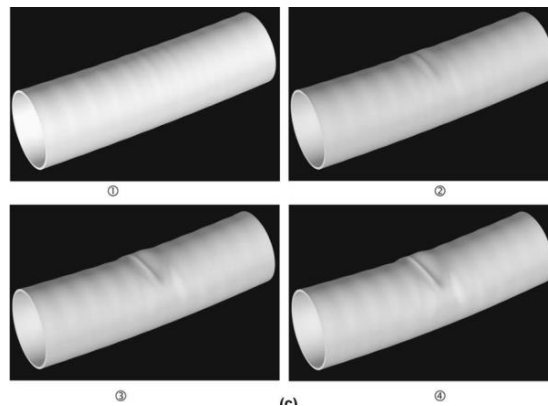


**Fig 11: Stages of localization of a wrinkle into a single fold. Reprinted from the work of Corona [15].**

Corona's work included a post-buckling response also using ABAQUS finite element software and, they detail in great lengths how they set it up, including an axisymmetric imperfection using a specific "half-wavelength" obtained from their analysis.

Unlike many of the other analyses, an elasto-plastic model was considered by using flow theory. On top of this isotropic model, terms were added by including the anisotropic material parameters which were found for the specific aluminum samples they were testing.

Like the earlier analysis, the model for moment vs curvature features a drop after a maximum moment from the critical curvature, seen below in figure 12. Their work showed that "this failure curvature is influenced by anisotropy directly as well as indirectly through the adopted wrinkle wavelength".
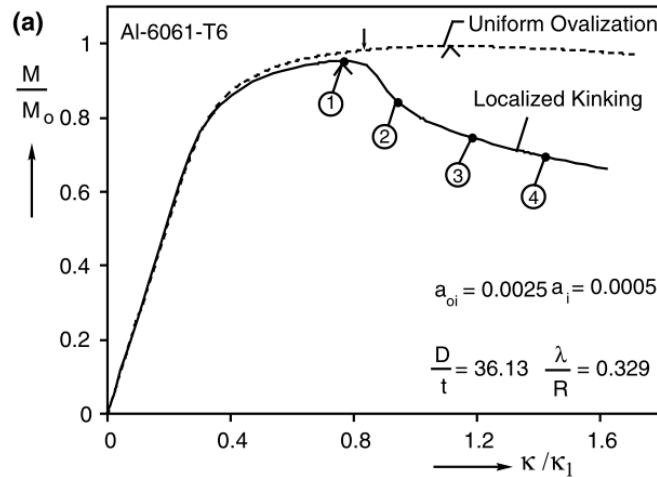


**Fig 12: Stages of localization of a wrinkle into a single fold. Reprinted from the work of Corona [15].**

While "the curvature corresponding to the limit moment was found to be in good agreement with the experimental values", the real-life experiment did not go into the post-buckling regime, and comparison to the simulation was made only at the critical curvature, not after that.

Concerning extending this simulation out further into the post-buckling regime, the author suggests using local refinement of the mesh which they did not pursue.

Towards the end of their paper, Corona mentions that the anisotropy affects failure curvature, but also the response of post-buckling calculations and leaves the judgment as to exactly how this affects the results to the reader. Looking at some of the results, it appears as though the post-buckling response is mostly just shifted and scaled from the change in critical curvature from the anisotropic effects, which can be seen in figure 13 below. The slopes appear to approach one another as curvature increases.
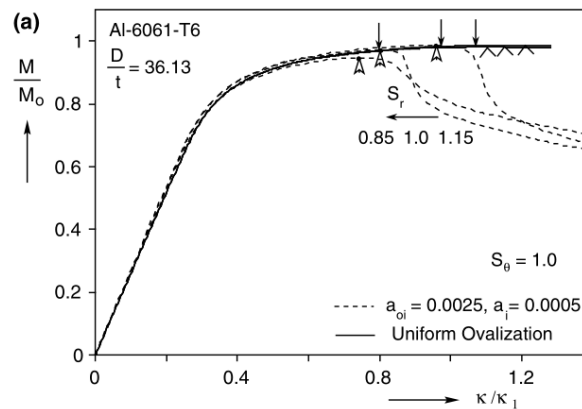
**Fig 13: Stages of localization of a wrinkle into a single fold. Reprinted from the work of Corona [15].**

Main Takeaways:
- Similar to the plots from Vaziri and Yadav, the post-buckling response appears to linearize as curvature increases.
- This work follows from experimental results, and they have explained why previous simulations results matched up poorly to experiment, and it was due to anisotropic effects.
- Anisotropy affects the post-buckling response, and researchers should be aware of this phenomena
- Finite element simulations with ABAQUS can be used to model these thin tubes, and care needs to be taken to initialize with proper amplitude wrinkles, otherwise, the response will not be accurate.

# Conclusions

In this literature review, the current research on kinking phenomena was summarized and shows a lack of theory in the area of the post-buckling regime, with only a handful of papers dealing in this area.

Many works describe the onset of buckling, and some of these have helped build the research into the post-buckling analysis too.

**From what has been summarized from the work, these are the areas that have begun being studied:**
- Stability of thin elastic tubes under pressure and bending loading
- Force-displacement as well as moment-angle, relationships for inextensional surfaces
- Moment-angle relationships from experiments and simulations of elastic-plastic
- ABAQUS finite element models for elasto-plastic models
- Anisotropy - how it plays a role in critical curvature and post-buckling
- Different modes of wrinkling for radius vs thickness ratios

**And these are the remaining areas that need to be considered for further work:**

- Stresses and strains within these collapsing tubes as a function of bending angle - this has been ignored for almost everything related to post-buckling research
- Anisotropy effects on the post-buckling response - equations describing this would be useful.
- The region where inextensional approximations can be used - when does this approximation fail for materials that are thicker, and more elastic?
- The highly elastic regime for rubbery polymeric materials - this has not been studied in any detail.
- Post-post-buckling regime - every study's results are for very small angles or curvatures, with nothing close to a "kinked in half" scenario

# Acknowledgements

# References

[1] L. G. Brazier, "On the Flexure of Thin Cylindrical Shells and Other "Thin" Sections," *Proceedings of the Royal Society of London. Series A, Containing Papers of a Mathematical and Physical Character*, vol. 116, (773), pp. 104-114, 1927.

[2] V. Tvergaard, "On the transition from a diamond mode to an axisymmetric mode of collapse in cylindrical shells," *International Journal of Solids and Structures*, vol. 19, (10), pp. 845-856, 1983.

[3] E. L. Axelrad, "On local buckling of thin shells," *International Journal of Non-Linear Mechanics*, vol. 20, (4), pp. 249-259, 1985.

[4] V.I. Weingarten, P. Seide, J. Peterson, Buckling of thin-walled circular cylinders, *NASA* SP-8007 (1968).

[5] S. Kyriakides and J. G.T, "Bifurcation and localization instabilities in cylindrical shells under bending—I. Experiments," *International Journal of Solids and Structures*, vol. 29, (9), pp. 1117-1142, 1992.

[6] S. Houliara and S. A. Karamanos, "Buckling and post-buckling of long pressurized elastic thin-walled tubes under in-plane bending," *International Journal of Non-Linear Mechanics*, vol. 41, (4), pp. 491-511, 2006.

[7] K. Kumar Yadav and S. Gerasimidis, "Instability of thin steel cylindrical shells under bending," *Thin-Walled Structures*, vol. 137, pp. 151-166, 2019.

[8] Y. Bai, R. Igland and T. Moan, "Collapse of thick tubes under combined tension and bending," *Journal of Constructional Steel Research,* vol. 32, (3), pp. 233-257, 1995.

[9] M. Elchalakani, R. Grzebieta and X. Zhao, "Plastic Collapse Analysis of Slender Circular Tubes Subjected to Large Deformation Pure Bending," *Advances in Structural Engineering*, vol. 5, (4), pp. 241-257, 2002.

[10] C. Mathon and A. Limam, "Experimental collapse of thin cylindrical shells submitted to internal pressure and pure bending," *Thin-Walled Structures*, vol. 44, (1), pp. 39-50, 2006.

[11] C. D. Coman, "Asymptotic approximations for pure bending of thin cylindrical shells," *Zeitschrift Für Angewandte Mathematik Und Physik*, vol. 68, (4), pp. 1-20, 2017.

[12] J.P. Fay, C.R. Steele, "Bending and symmetric pinching of pressurized tubes," *International Journal of Solids and Structures,* vol. 37,(46-47), pp. 6917-6931, 2000

[13] A. Vaziri, "Mechanics of highly deformed elastic shells," *Thin-Walled Structures*, vol. 47, (6), pp. 692-700, 2009.

[14] J. W. Hutchinson, "Buckling and Initial Postbuckling Behavior of Oval Cylindrical Shells Under Axial Compression," *Journal of Applied Mechanics*, vol. 35, (1), pp. 66-72, 1968.

[15] E. Corona, L. -. Lee and S. Kyriakides, "Yield anisotropy effects on buckling of circular tubes under bending," *International Journal of Solids and Structures*, vol. 43, (22), pp. 7099-7118, 2006.

# Appendix  H

# Static Pressure Tube Bending Experiment Test Procedure

# Test Procedure Static Pressure Tube Bending Experiment

Kyle Marquis, Started Oct 23, 2020

# Pre-Procedure Checklist

1. Have 3 different Tube Samples already measured and cut for a given material and geometry. Tube Samples must be fresh, and never kinked. There should be a small mark in the center of the sample
2. Have correct closest Tube Holder size within 0.4 mm of the inner diameter of the tube
3. Have enough PTFE Tape to wrap around the tube for sealing, both thin and thick varieties
4. Have correct O Ring size close but above Tube Sample inner diameter
5. Have Air Hose
6. Have Regulator with 0-2 Bar Pressure Gauge installed onto table
7. Have Small Air Tube
8. Put on Safety Glasses when pressurizing equipment
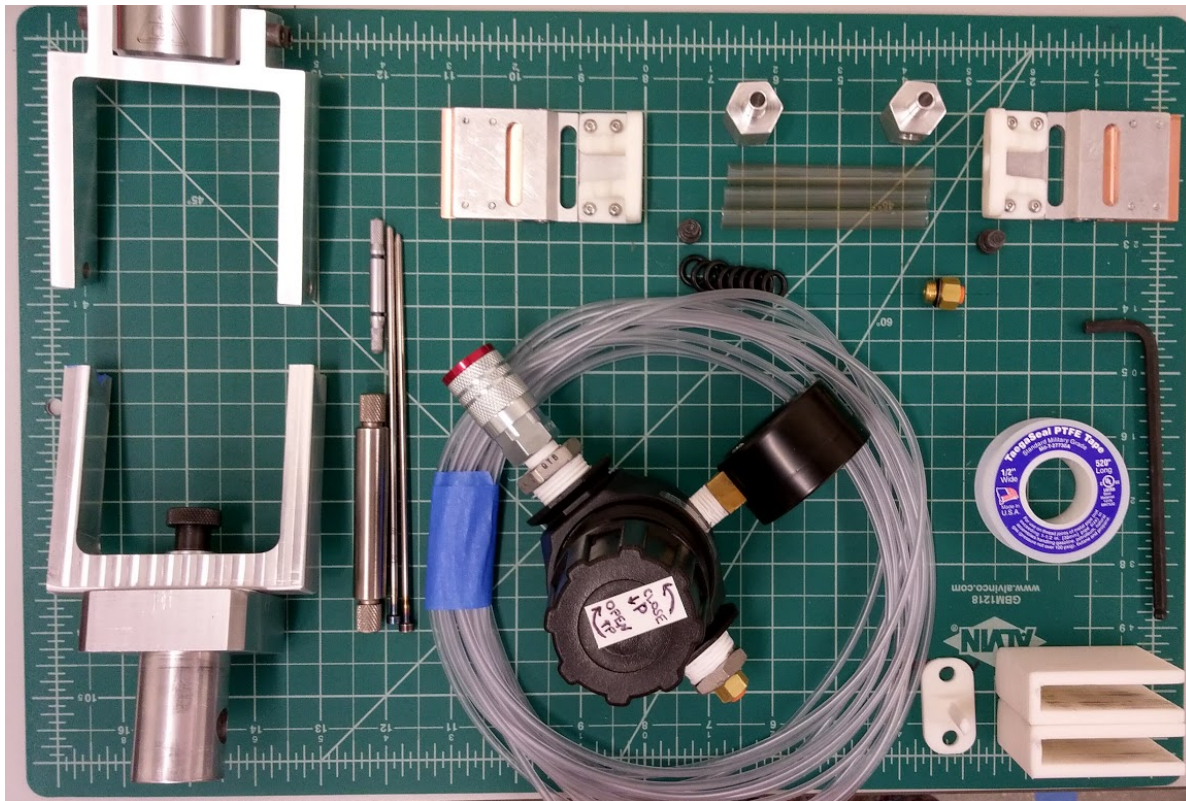
# Test Procedure Static Pressure Tube Bending Experiment

## Instron Setup 1

9. Start system and software
10. Open Instron Machine method called SPBendTest_Method
11. Ensure **100 N** load cell attached
12. Add Clevis System, set distance to be full extension length (distance hole to hole for the later defined Bending Grip Assembly)
13. Put masking tape on clevis ends to prevent reflections
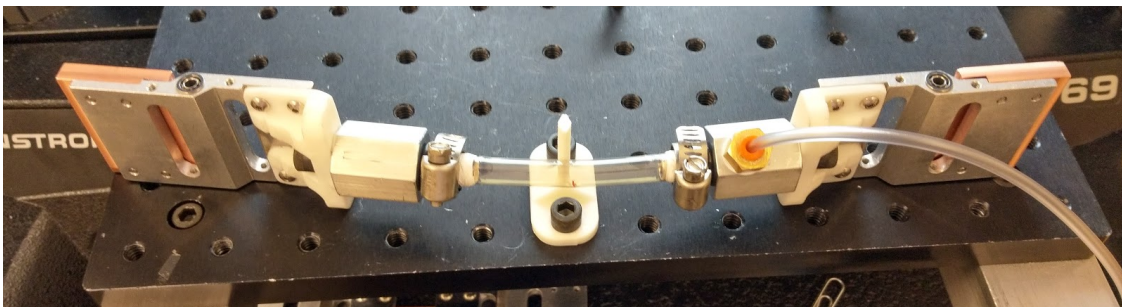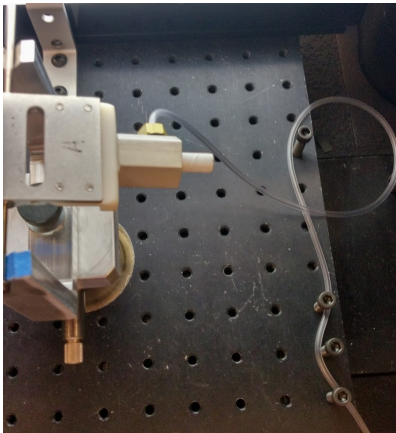
<p align="center"><u>Test Procedure Static Pressure Tube Bending Experiment</u></p>

# Test + Pressure Setup

14. Ensure one of the Tube Holders contains the Push-To-Connect Fitting, complete with plenty of PTFE Tape, and torqued down
15. Insert Air Hose into Wall Port and confirm Wall Port Valve is closed with no air coming out
16. Set up Pressure Regulator on Table, tightening down to Table or onto Aluminum Breadboard
17. Ensure Regulator Knob is rotated all the way counterclockwise, closed
18. Attach Air Hose to Regulator, turn on building air by turning valve, and ensure no air coming out from regulator
19. Take Small Air Tube from Regulator and attach to Tube Holder's Push-To-Connect Fitting
20. Test Pressure by rotating Regulator Knob clockwise slowly until air hisses out of the Tube Holder cylinder. Put finger on the end, and increase the pressure until 2 bar, ensuring no leaks at that pressure. If there are any leaks, wrap with more PTFE Tape and tighten the joints
21. Remove Small Air Tube from Push-To-Connect Fitting for now, while the Tube Holder Assembly is set up
22. Now wrap PTFE Tape around the first Tube Holder cylinder
23. Slide Tube Sample onto tube holder covered now in PTFE tape. Should barely slide on with axial load by hand, leave about a mm until the endfor overwrap of next PTFE
24. Apply a significant amount of PTFE Tape, wrapping at least 5 times until O rings fit snugly
25. Add O Rings, ensuring snug fit around PTFE Tape
26. Slide first Hose Clamp over O Rings, removing any that won't fit with the clamp
27. Using ¼" Socket Wrench for Hose Clamps, tighten with reasonable force, but not full strength
28. Ensure no O Rings are interfering with the Tube Sample, so not poking out past the cylinder
29. Now place that number of O rings around the tube that is now attached to one of the Tube Holders, as well as the second Hose Clamp
30. Using same number of PTFE Tape wraps as before, wrap the bare second Tube Holder with PTFE Tape
31. Slide the second Tube Holder, again snugly fitting, onto the Tube Sample leaving a 1 mm gap to the end. Ensure the Push-to-Connect Fitting is facing towards you and up, and ensure the hexagonal pieces are flat on a surface.
32. Again, apply a significant amount of PTFE Tape, wrapping at least 5 times until O rings fit snugly
33. Again, slide O Rings on, ensuring snug fit around PTFE Tape
34. Now attach second hose clamp around O Rings

# Test Procedure Static Pressure Tube Bending Experiment

35. Use ¼" Socket Wrench again to tighten last Hose Clamp with reasonable force, but not full strength

36. Again, ensure no O Rings are interfering with the Tube Sample, so not poking out past the cylinder

37. You should now have the Tube Sample sealed and tightened around the Tube Holders, set it aside as the Clevis System is set up. The Tube Sample should have barely any kinks in it, if it has major ones near the center, make and use a new sample.

38. Ensure Copper Counterweights are thoroughly attached and flush with Bending Grips

39. Ensure Tube Holder Brackets are thoroughly attached and flush with Bending Grips

40. Attach Tube Holder Assembly onto the first Tube Holder Bracket using ¼-20 Socket Head Cap Screw which should be 12.5 mm long. Use fingers to hand tighten the screw, then use the allen key to tighten, while making sure the Push-to-Connect Fitting is on the right, and facing away and up.

41. Attach Tube Holder Assembly onto the second Tube Holder Bracket using ¼-20 Socket Head Cap Screw which should be 12.5 mm long. Use the allen key to tighten, while making sure the Push-to-Connect Fitting is on the right, and facing away and up.

42. Ensure that neither of the threaded connections are loose and that the Bending Grip Assembly is as shown.   Bending should be able to occur to the right when viewing the Instron Machine from the front.

# Test Procedure Static Pressure Tube Bending Experiment
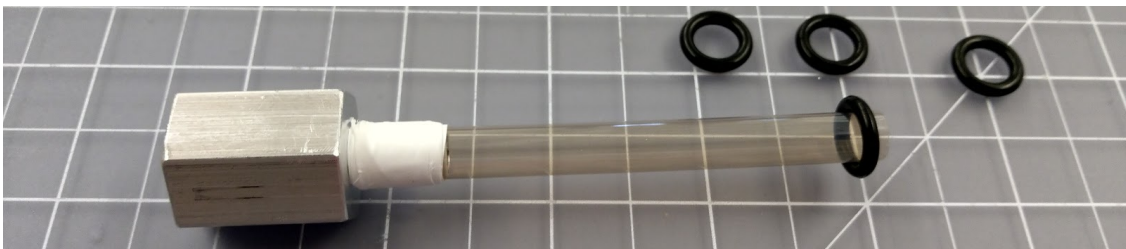
# Test Procedure Static Pressure Tube Bending Experiment
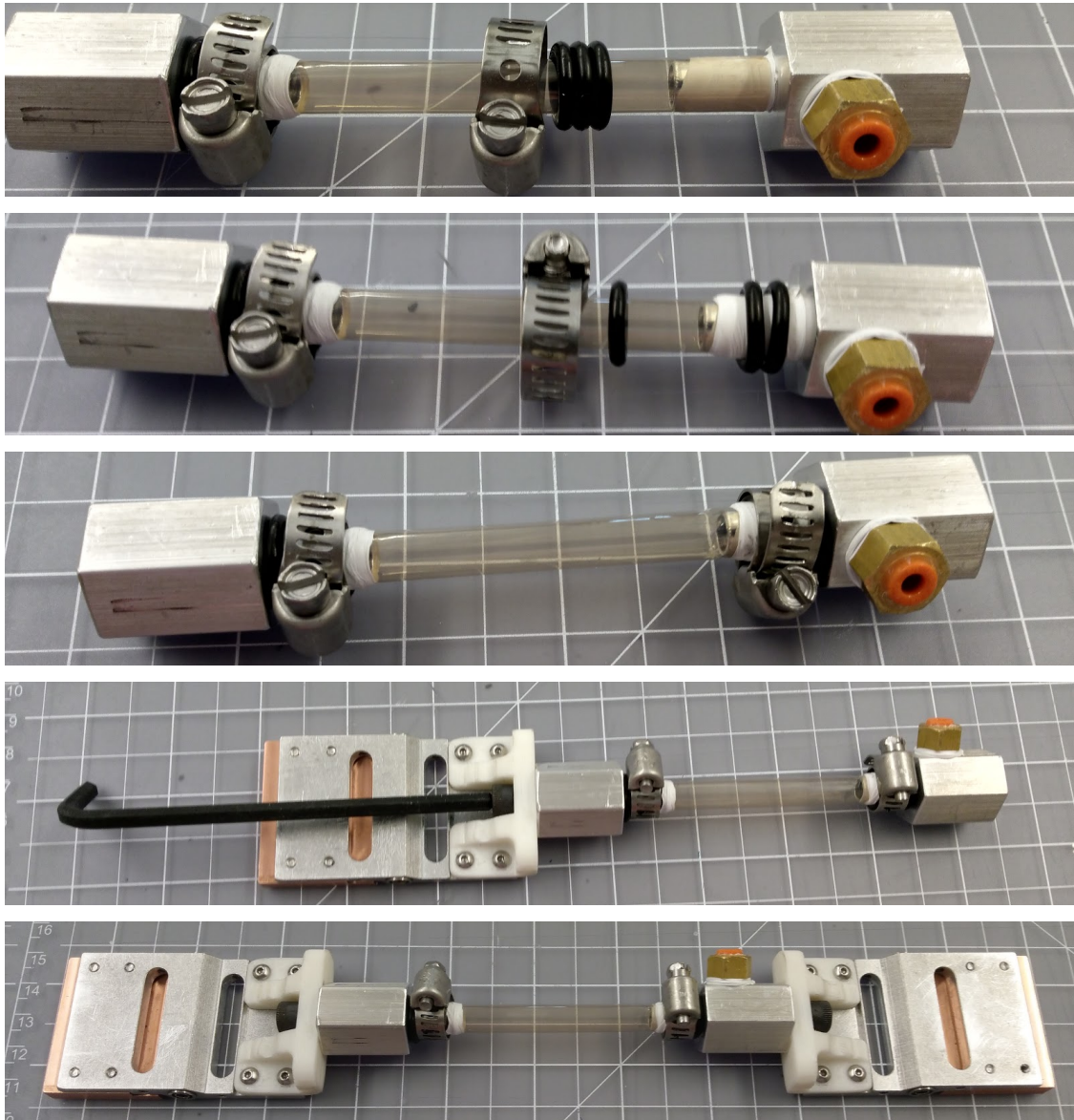
Test Procedure Static Pressure Tube Bending Experiment

# Camera Setup

43. Get NIKON? camera with telephoto lens
44. Move stand into pre-taped floor position
45. Place NIKON? Camera onto Stand, with portrait position
46. Go into video mode by flicking the switch to the right of the main screen and leaving the top left knob in auto. Top here means top when held in landscape position
47. Ensure camera and stand are centered using bubble levels
48. Adjust Stand height to center on the position slightly above bottom Clevis
49. Ensure no reflections of the clevis
50. Adjust telephoto zoom to capture top Clevis after full extension, with center closer to bottom Clevis
51. Adjust Focus to make sharp edges

# Instron Zeroing and Setup 2

52. Zero the Force on the Instron Interface with just the Clevis
53. Use Clevis Rods and hang Bending Grip Assembly in top Clevis, write down the weight **WITHOUT TUBE**
54. Remove Bending Grip Assembly and place Clevis Rods aside
55. Set distance between clevises to be a y height of 32 mm, measured using Calipers
56. Now, carefully bend the center of the Tube Sample by hand around the Small Peg attached to the Aluminum Breadboard.
57. Keeping the Bending Grip Assembly in the "bent partway" position, CAREFULLY insert into the Instron Machine, using the Clevis Rods to affix to the Clevises.
58. Zero displacement
59. Ensure travel distance set on method to 202 mm

## Test Procedure Static Pressure Tube Bending Experiment

# Test Operation

60. Ensure pressure level is set, connected, not leaking
61. Ensure camera is focused properly
62. Hit **record** on Camera, ensure flashing red dot on screen
63. Hit **Start Test**
64. When no more movement, and test is finished, hit **record** again on Camera, ensure flashing red dot is gone to end the video
65. Turn pressure gauge back to 0 for the manual process of re-bending the tube
66. Remove the Bending Grip Assembly from the Clevises, and while keeping the pressure tube attached, bend the center of the Tube Sample by hand around the Small Peg again.
67. Press **RETURN** on Instron to return to original displacement of 0
68. Place back onto Clevises now in closed (kinked) position
69. Increase pressure to next level according to the Tube Data Spreadsheet
70. Repeat steps 62-69 to get through all pressure levels for the sample. Each time, removing sample from clevises, returning to 0 displacement, re-bending around the Small Peg, and replacing back into the Instron
71. Hit **finish** to save as CSV file for all the pressures
72. Remove SD card from Camera, and load into new folder
73. Go into folder and rename to SPBendTest_VZ_pAAA_YYYYMMDD
    a. Where V refers to geometry letter code
    b. Where Z refers to the sample number, eg, 1,2, or 3
    c. Where AAA refers to the pressure in kPa, eg 040
    d. Where YYYYMMDD refers to the year month and date of the test, eg, 20201023
74. Remove Tube Sample from Bending Grip Assembly
75. Repeat steps 22-42 to replace the tube with a new sample for the given geometry & material. Then repeat steps 60-74 until all the samples are tested.
76. Repeat from beginning for new geometry and/or material specimens

# Images during Operation
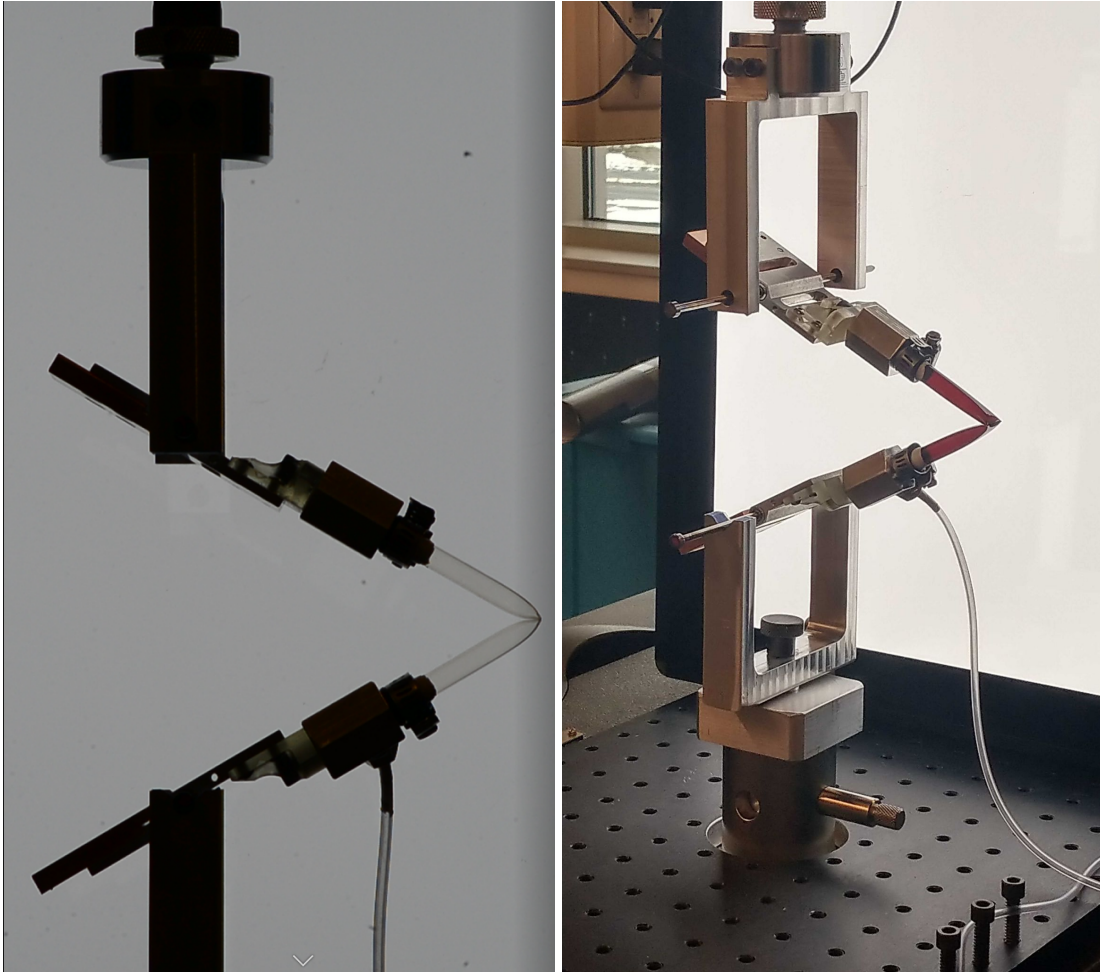
# Appendix  I

## Parameters for Thin Tube Geometries and Materials used in Bending Moment Static Pressure Tests

Parameters are shown for thin tube geometries and materials which were used in bending moment static pressure tests. Some geometries were acquired for comparison purposes, but not tested. Acquiring samples that held radius and thickness constant across trials was a challenge with the limited budget of this project, and compromises were made accordingly.

## Tube Data

Black = from Mfr or measured    Magenta = assumed (from other datasheets)

| Geo | Material | Tested | Inner Diameter [mm] | Wall Thickness [mm] | Modulus of Elasticity [MPa] | Ultimate Tensile Strength [MPa] | Yield Strength [MPa] |
|---|---|---|---|---|---|---|---|
| a | PTFE | ☑ | 7.70 | 0.127 | 390-600 | 21-35 | 9 |
| b | PTFE | ☑ | 6.60 | 0.051 | 390-600 | 21-35 | 9 |
| c | PTFE | ☑ | 5.84 | 0.051 | 390-600 | 21-35 | 9 |
| d | PTFE | ☑ | 3.05 | 0.019 | 390-600 | 21-35 | 9 |
| e | PTFE | ☑ | 2.03 | 0.019 | 390-600 | 21-35 | 9 |
| f | PTFE | ☑ | 4.22 | 0.254 | 390-600 | 21-35 | 9 |
| g | PTFE | ☑ | 1.93 | 0.203 | 390-600 | 21-35 | 9 |
| h | PTFE | ☑ | 5.28 | 0.254 | 390-600 | 21-35 | 9 |
| i | PTFE | ☑ | 7.34 | 0.381 | 390-600 | 21-35 | 9 |
| j | PTFE | ☑ | 5.28 | 0.381 | 390-600 | 21-35 | 9 |
| k | FEP | ☑ | 5.94 | 0.381 | 440-640 | 21-35 | 12 |
| l | FEP | ☑ | 5.77 | 0.254 | 440-640 | 21-35 | 12 |
| m | FEP | ☑ | 4.50 | 0.254 | 440-640 | 21-35 | 12 |
| n | Polyimide | ☑ | 5.74 | 0.070 | 2760 | 231 | 138 |
| o | Polyimide | ☑ | 5.88 | 0.133 | 2760 | 231 | 138 |
| p | Polyimide | ☑ | 7.70 | 0.069 | 2760 | 231 | 138 |
| q | Polyimide | ☑ | 7.11 | 0.152 | 2760 | 231 | 138 |
| r | BoPET | ☑ | 4.75 | 0.076 | 3100 | 138 | 97 |
| s | BoPET | ☐ | 6.35 | 0.076 | 3100 | 138 | 97 |
| t | BoPET | ☐ | 7.95 | 0.076 | 3100 | 138 | 97 |
| u | PEEK | ☑ | 8.26 | 0.127 | 3700-4000 | 98-100 | 110 |
| v | PEEK | ☐ | 3.18 | no data | 3700-4000 | 98-100 | 110 |
| w | PEEK | ☐ | 2.13 | 0.038 | 3700-4000 | 98-100 | 110 |
| x | Polyimide | ☑ | 7.70 | 0.086 | 2760 | 231 | 138 |

Figure I.1: Tube data of acquired samples for bending moment testing

# Appendix  J

# Lumped Element Rigid Panel Dynamics Model

A lumped element rigid panel dynamics model was created to find the natural frequencies of the deployed system. Below, Figure J.1 shows a system diagram for the oscillating system, the free body diagram of a panel in the system, and a diagram equating a beam in bending to rigid panels connected with a torsional spring.

First, the polyimide tube needs to be connected to the lumped model. From beam theory, bending moment on a small beam element can be defined as:

$$M = \kappa E I \tag{J.1}$$

Where

$$\Delta \theta = \kappa L \tag{J.2}$$

As well, torsional springs can be described as

$$M = k \Delta \theta \tag{J.3}$$

Accordingly, spring stiffness, $k$ can be written as

$$k = E I / L \tag{J.4}$$

Which provides the bridge between the thin tubes and the lumped element model. The equations of motion are derived below. Note that each panel individually only has a single rotational degree of freedom, but can move in the y-direction through the previous panels' rotation. The displacement,
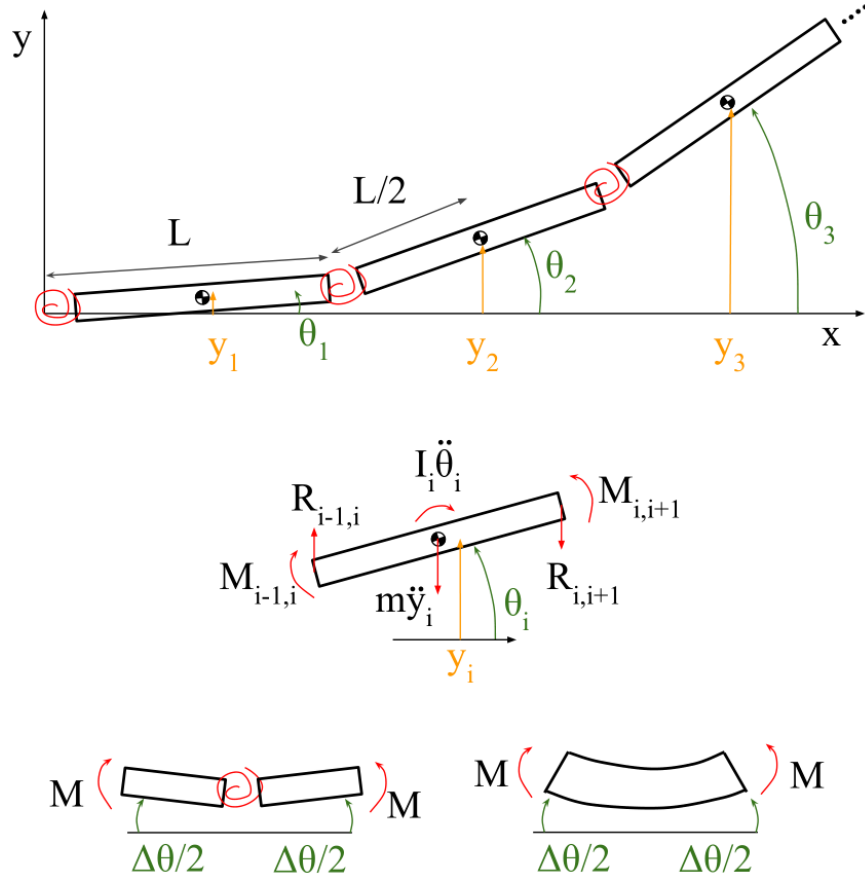
Figure J.1: Top: System diagram for lumped element model with rigid panels connected by torsional springs. Center: free body diagram of a panel within the system. Bottom: comparison between beam element and torsional spring with mass element

velocity, and linear acceleration can be replaced using rotational degrees of freedom.

$$y_i = y_{i-1} + \frac{L}{2}sin(\theta_i) \tag{J.5}$$

$$\dot{y}_i = \frac{dy_i}{dx} = \dot{y}_{i-1,i} + \frac{L}{2}cos(\theta_i) \cdot \dot{\theta}_i \tag{J.6}$$

Assuming small-angle approximation

$$\ddot{y}_i = \ddot{y}_{i-1,i} + \frac{L}{2}\ddot{\theta}_i \tag{J.7}$$

For boundary conditions, at the first hinge $\ddot{y}_{0,1} = 0$ so $\ddot{y}_1 = \frac{L_1}{2}$. As well, end loads are zero at the furthest most panel, lets call that N , so $R_{N,N+1} = 0$, and $M_{N,N+1} = 0$. Using equation J.7 and the left boundary condition, solutions can be found for each successive $y_i$ in terms of the angular

accelerations.

$$\ddot{y}_i = \sum_{n=1}^{i} \left( L_i \ddot{\theta}_i \right) - \frac{L_i}{2} \ddot{\theta}_i \tag{J.8}$$

Similarly, by taking sum of forces in the y-direction, we can find the reactions at every joint based on the boundary conditions.

$$R_{i,i+1} = f([m_1, m_2, ...m_N], [L_1, L_2, ...L_N], [\ddot{\theta}_1, \ddot{\theta}_2, ...\ddot{\theta}_N]) \tag{J.9}$$

Here, mass of each panel is $m_i$. Taking sum of moments gives

$$-I_i \ddot{\theta}_i - \frac{L_i}{2}(R_{i-1,i} + R_{i,i+1}) - M_{i-1,i} + M_{i,i+1} = 0 \tag{J.10}$$

Where the applied moments can be written as a function of the difference in angle between the panels.

$$M_{i,i+1} = k_{i,i+1}(\theta_{i+1} - \theta_i) \tag{J.11}$$

Applying the boundary condition where the initial angle is zero, $\theta_0 = 0$, and the final panel has no hinge at the end, the following matrix can be derived:

$$K = \begin{bmatrix} (k_{0,1} + k_{1,2}) & -k_{1,2} & 0 & 0 & & & & 0 \\ -k_{1,2} & (k_{1,2} + k_{2,3}) & -k_{2,3} & 0 & & & & \\ 0 & -k_{2,3} & (k_{0,1} + k_{0,1}) & -k_{3,4} & & & & \\ & & & & \ddots & & 0 & \\ & & & & -k_{n-1,n} & (k_{n-1,n} + k_{n,n+1}) & -k_{n,n+1} & \\ & & & & 0 & & \ddots & \\ 0 & & & & & & -k_{N-1,N} & k_{N-1,N} \end{bmatrix} \tag{J.12}$$

The inertial terms can be cast into matrix form, with rows m and columns n, with N number of

panels and becomes:

$$I = \begin{bmatrix} \ddots & & & \\ & I_n + \frac{L_n^2}{2}\left(\frac{m_n}{2} + 2\sum_{i=n+1}^{N} m_i\right) & \cdots & \frac{L_m L_n}{2}\left(m_n + 2\sum_{i=n+1}^{N} m_i\right) \\ & & \ddots & \\ & & & \\ Sym. & & & \ddots \end{bmatrix} \quad \text{(J.13)}$$

For the overall system, these can be combined for a linear symmetric equation of motion:

$$I \begin{bmatrix} \ddot{\theta}_1 \\ \ddot{\theta}_2 \\ \vdots \\ \ddot{\theta}_N \end{bmatrix} + K \begin{bmatrix} \dot{\theta}_1 \\ \dot{\theta}_2 \\ \vdots \\ \dot{\theta}_N \end{bmatrix} = \begin{bmatrix} 0 \\ 0 \\ \vdots \\ 0 \end{bmatrix} \quad \text{(J.14)}$$

This equation of motion can then be recast as a vibratory eigenvalue problem and solved for natural frequency just like any mass-stiffness linear undamped system such as that seen in Chapter 8 of Kelly, 2011[1] . It takes in panel mass, length, and inertia as well as hinge stiffness EI and hinge length. This work assumes small displacements by way of small-angle approximation, and that the hinges do not contribute any significant damping. Further, this model assumes 2D motion and is not meant to represent the other torsional modes for two sets of panels in 3D space. It is assumed that this mode is representative of the worst-case natural frequency with the two sets of panels bending up and down together.

---

[1] Mechanical Vibrations Theory and Applications by S. Graham Kelly, 2011